Cold Beams of Large Molecules for Structural Dynamics Studies

Dissertation

zur Erlangung des Doktorgrades
an der Fakultät für Mathematik, Informatik und
Naturwissenschaften,
Fachbereich Chemie
der Universität Hamburg

vorgelegt von

Nicole Teschmit

Hamburg

2018

Gutachter der Dissertation: Prof. Dr. Jochen Küpper
Prof. Dr. Horst Weller

Zusammensetzung der Prüfungskommission: Prof. Dr. Jochen Küpper
Prof. Dr. Dr. Christian Betzel
Prof. Dr. Gabriel Bester

Datum der Disputation: 31 August 2018

Eidesstattliche Versicherung

Hiermit versichere ich an Eides statt, dass ich die Inanspruchnahme fremder Hilfen aufgeführt habe, sowie, dass ich die wörtlich oder inhaltlich aus anderen Quellen entnommenen Stellen als solche kenntlich gemacht habe. Weiterhin versichere ich an Eides statt, dass ich die Dissertation selbst verfasst und keine anderen als die angegebenen Hilfsmittel benutzt habe.

Nicole Teschmit

Contents

Abstract . . . 1

Zusammenfassung . . . 3

1 Introduction 5

1.1 Motivation . . . 5

1.2 Laser Desorption . . . 9

1.3 Controlling Molecules . . . 11

1.4 Overview . . . 13

2 Fundamental Concepts 17

2.1 Rotational States of Molecules . . . 17

2.2 Supersonic Molecular Beams . . . 20

2.3 Electrostatic Deflection . . . 22

3 Experimental Setup 29

3.1 Laser Desorption Source Design — Considerations . . . 29

3.2 New Source Design - Technical Realisation . . . 32

3.3 Integration in the Molecular Beam Setup . . . 39

3.4 Sample Preparation . . . 41

4 Characterising and Optimising a Laser Desorption Source 45

4.1 Introduction . . . 45

4.2 Experimental Setup . . . 47

4.3 Results and Discussion . . . 51

4.4 Conclusion 61

5 Spatially Separated Conformers of a Dipeptide 63

5.1 Introduction 63

5.2 Results and Discussion 66

5.3 Conclusion 73

5.4 Methods 74

6 Spatially Separated Conformers of Glycine 75

6.1 Introduction 75

6.2 Stark Interaction 76

6.3 Glycin Time-of-Flight Mass Spectrum 78

6.4 Electrostatic Deflection of Glycine 79

6.5 Conclusion 82

7 Insulin in the Gas-Phase 85

8 Suggested Improvements of the Laser Desorption Source 89

9 Summary and Outlook 93

Bibliography 99

Curriculum Vitae 109

Publications 111

H- und P-Sätze 113

Abstract

Biomolecules and their reactions are of great interest because they are important for the functions in our body and thus for health. The structure of a molecule defines its function, and in this work we demonstrate the crucial steps that will allow direct recording of structural information from large biological molecules through gas-phase x-ray diffraction. This requires a source of intact biomolecules in the gas-phase, as well as the ability to ensure all molecules in the x-ray focus are structurally identical. In this thesis it is shown how this can be achieved using a laser desorption molecular beam source in combination with electrostatic deflection.

Following an introduction into the subject and a brief review of the theoretical background in the first two chapters, chapter 3 contains the details of our new laser desorption source for thermally labile biomolecules, that is fully compatible with use at central facilities. Afterwards, a characterisation of the laser-desorption molecular beam source is presented in chapter 4. Utilizing strong-field ionisation, we characterised the produced molecular beam and evaluated the influence of various experimental parameters. Strong-field ionisation acted as a universal probe and enabled us to analyse the purity of the produced molecular beam, including molecular fragments. The optimised source was then combined with an electrostatic deflector for species separation. In chapter 5 it is shown that a cold molecular beam of Ac-Phe-Cys-NH_2 is produced and the conformers are spatially separated. This is the first demonstration of conformer-selected and rotationally cold molecular beams of peptides, which is a crucial step towards the implementation of single-molecule diffractive imaging experiments of biological systems. Additionally, it was possible to produce a molecular beam of glycine with the laser desorption source. Combined with the electrostatic deflector one of the conformers of glycine could be separated from the other two, shown in chapter 6, enabling novel conformer-resolved ultrafast dynamics experiments. In chapter 7 the applicability of the source to even larger biomolecules, through first measurements of insulin, is demonstrated. In the last two chapters a summary and outlook is given and several improvements and follow-up experiments are suggested.

Zusammenfassung

Biomoleküle und ihre Reaktionen sind von großem Interesse, weil sie wichtig für die Funktionen in unserem Körper und damit auch für die Gesundheit sind. Die Struktur eines Moleküls definiert seine Funktion. In dieser Arbeit demonstrieren wir die erforderlichen experimentellen Grundlagen zur Durchführung von Strukturmessungen an isolierten biologischen Molekülen mittels Röntgenbeugung. Dafür wird eine Quelle benötigt die Biomoleküle unbeschädigt in die Gasphase überführt und zusätzlich ermöglicht, dass alle Moleküle im Röntgenfokus eine identische Struktur aufweisen. Unter Benutzung einer Laserdesorptionsquelle in Kombination mit einem elektrostatischen Deflektor wurde dieses erreicht.

Nach einer kurzen Einleitung und einer Übersicht über den theoretischen Hintergrund in den ersten beiden Kapiteln folgt in Kapitel 3 eine Beschreibung des Aufbaus und der Funktionen der neuen Quelle, die des Weiteren für den Einsatz an Freie-Elektronen Lasern ausgelegt wurde. Anschließend wird eine Charakterisierung der Laserdesorptionsquelle in Kapitel 4 gezeigt. Mit Hilfe der Starkfeldionisation wird der erhaltene Molekülstrahl charakterisiert und der Einfluss verschiedener Faktoren untersucht. Die Starkfeldionisation ionisiert alle Spezien in dem Molekülstrahl, dies beinhaltet auch die vorhandenden Fragmente und ermöglichte deswegen die Reinheit des Molekülstrahls zu analysieren. Die optimierte Quelle wird anschließend mit dem elektrostatischen Deflektor zur Trennung der vorhanden Spezien kombiniert. In Kapitel 5 wird gezeigt dass ein kalter Molekülstrahl des Dipeptides Ac-Phe-Cys-NH_2 erzeugt und die Konformere räumlich getrennt werden konnten. Das ist die erste Demonstration von konformerausgewählten und rotationskalten Molekülstrahlen von Peptiden und ein kritischer Schritt für die Durchführung von Röntgenbeugungsexperimenten an isolierten Molekülen in der Gasphase. Zusätzlich war es möglich einen kalten Molekülstrahl von Glycin zu erzeugen. Ein Konformer von Glycin konnte ebenfalls mit elektrostischer Ablenkung von den anderen beiden Konformeren räumlich getrennt werden, wie dargestellt in Kapitel 6. In Kapitel 7 wird am Beispiel von Insulin gezeigt, dass die Quelle auch mit größeren Proteinen verwendet werden kann. In

den letzten beiden Kapiteln ist eine Zusammfassung und Perspektive beschrieben, die mögliche Verbesserungsvorschläge und zukünftige Experimente enthält.

1 Introduction

1.1 Motivation

Chemical reactions are taking place all around us. The ubiquity of chemical reactions makes it so important and interesting to study and understand every step of them. To understand a chemical reaction, the structures of the involved reactants, products and, if possible, of transition states need to be known, because the structure defines the function of a molecule. This is confirmed by the large role structure determination and the development of novel structure determination methods plays in chemistry and biology. For example, the 2009 noble price for chemistry was awarded to V. Ramakrishnan, T. A. Steitz, and A. E. Yonath for their studies of the structure and function of a ribosome. In this example the structure of a bacteria ribosome was determined and thus the interaction of antibiotics with it could be understood, aiding the production of new antibiotics. This connection exemplifies the importance of structural determination in chemistry and biology. Typical methods to gain structural information are nuclear magnetic resonance (NMR)-spectroscopy, rotational spectroscopy, infrared (IR)-spectroscopy, cryogenic-electron microscopy, x-ray crystallography, or mass spectrometry.

Even more interesting than the static molecular structure are the dynamics of a molecule or a molecular reaction. Here, the ultimate goal is to measure a so called *molecular movie* with femtosecond temporal and picometer spatial resolution, i. e., to measure the position of all atoms within a molecule and how their positions change in real-time during a reaction. No currently available technique can achieve this resolution in both spatial and

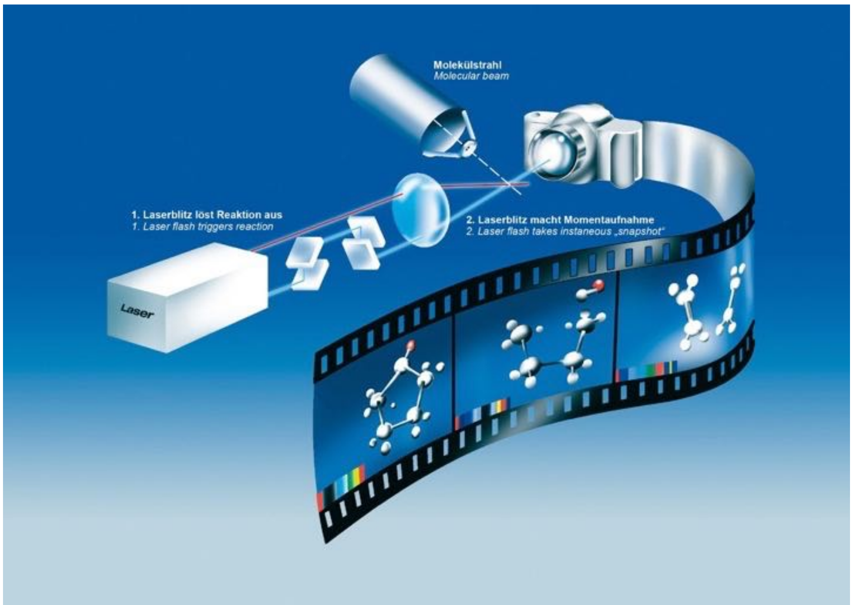
Molekülstrahl
Molecular beam
1. Laserblitz löst Reaktion aus
1. Laser flash triggers reaction
2. Laserblitz macht Momentaufnahme
2. Laser flash takes instaneous „snapshot"
Laser

Figure 1.1: A measurement of a molecular movie using a pump-probe experiment is shown. A molecular beam is crossed with a pump pulse which triggers the reaction. Afterwards a probe pulse makes a snapshot of the structure exactly at one certain time after the pump pulse, for example by a short x-ray pulse. Figure adapted from MPIbpc, DESY Photon Science.

temporal domains. A proposed way to record a *molecular movie* is through pump-probe measurements of isolated molecules in the gas-phase. For a pump-probe measurement a reaction is, for example, started with an ultrashort laser pulse (this acts as the pump). After certain time delays the molecule is probed, e. g., *via* x-ray diffraction. For each time delay the molecular structure can be reconstructed from the recorded diffraction pattern and thus the structure of the molecule can be measured as a function of time. Putting together many such snapshots creates a stop-motion movie of the molecular movement, as shown in Figure 1.1. For example, intra-molecular movements like torsions or inversions can be observed in this fashion [1]. Such data can, furthermore, give direct information about structures of molecules at their transition state and this knowledge could subsequently be used to control or steer a chemical reaction.

Free-electron lasers offer, due to their short wavelength, high intensity and short pulses, a tool to record diffraction patterns from single gas-phase molecules with sufficient temporal and spatial resolution [2]. From the measured diffraction pattern the structure of a gas-phase molecule can be determined. This has been demonstrated for ultrafast dynamics in nanocrystals, such as the *cis-trans* isomerisation of photoactive yellow protein [3], however the dynamics in crystals are limited and thus it is preferable to measure dynamics in a gas-phase sample. To realise x-ray diffractive imaging of isolated molecules several requirements need to be fulfilled.

Firstly, every molecule is destroyed by the high intensity of the few femtosecond x-ray pulse of the free-electron laser [4]. However, it has been proposed and demonstrated that because of the short pulse duration the x-ray beam is diffracted before the molecules are destroyed (diffraction before destruction) and hence a pattern of the intact molecule can be recorded [2, 4–6]. This furthermore requires the delivery of new molecules into the interaction region for each x-ray shot. This can be achieved using a molecular beam, so that the destruction of the molecules is not an issue any more as every shot probes a fresh sample of molecules. However, electronic damage induced by a free-electron laser pulse can be much faster than the pulse duration and needs to be considered in electronic structure studies [7, 8].

Secondly, it needs to be considered that a single molecule is not diffracting sufficiently to record a full diffraction pattern. Since the diffracted photons in a single pulse are not enough to determine which molecule diffracted them it is important to have identical molecules interacting with the x-ray beam. Especially if several molecules present in the interaction region are hit by the x-ray beam in a single shot, it is important that this molecular ensemble consists of identical molecules. Otherwise the structural information encoded in the diffraction pattern would not lead to a well defined molecular structure. This requires that even different structural conformers present in the molecular beam need to be separated before the interaction with the x-ray beam.

Lastly, the orientation of the molecules within the molecular ensemble being probed is important. If the molecules are isotropically (i. e., randomly) oriented in space, the diffracted signal from each individual molecule cannot be added together since the molecular orientation is not identical. This leads essentially to a blurring of the diffraction pattern

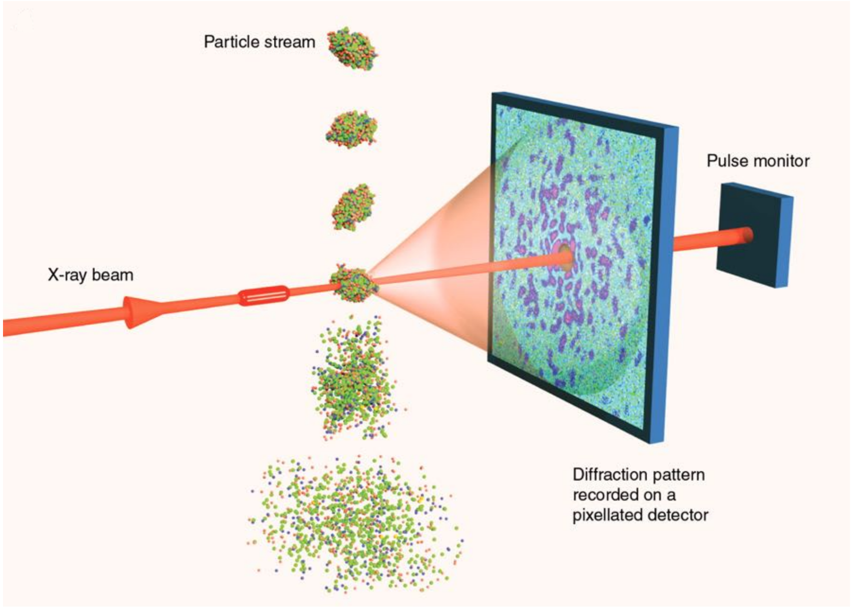

Figure 1.2: Sketch of a single-molecule diffraction experiment. A stream of identical particles is crossed by an x-ray beam. The diffraction of the x-ray beam is recorded by a large area pixel detector, which has a hole for the direct beam, whose intensity is recorded on a pulse monitor. Figure adapted from [9].

over all possible molecular orientations. This can be overcome by aligning or orienting the molecules in space during the interaction with the x-ray pulse [5, 10, 11]. This allows the diffraction signal to be averaged over many molecules and hence a better signal-to-noise ratio is achieved [5]. Furthermore, diffraction patterns need to be added for many successive x-ray laser pulses, all containing diffraction from identically aligned molecules. To align and orient molecules a very cold molecular ensemble is required.

In Figure 1.2 this principle, termed “single-molecule diffraction” is shown schematically. A particle stream delivers new sample for each x-ray shot. The particle is destroyed after the x-ray beam hit it, with a large area detector recording the diffraction pattern. A hole in the detector lets the un-diffracted x-ray beam pass, which is monitored behind the detector. The possibility to gain structural information by x-ray diffraction of gas-phase samples has recently been shown in a proof-of-principle experiment [6], using controlled molecular beams of small molecules [12, 13].

To unravel how life works and how human bodies function, biological molecules are of significant interest. But it is not trivial to solve the complete structure of a biological molecule, for example it is often difficult to produce crystals in sufficient size and purity for x-ray crystallography. So we want to investigate individual biological molecules in the gas-phase, resolve their structure and learn about their reactions. But, as described above, for these experiments a cold and conformer-selected molecular beam of biological molecules is required. At the moment there is no system which can achieve this and that delivers large, controlled, and isolated biological gas-phase molecules to the interaction point of a free-electron laser. In this thesis the above mentioned experiments will be enabled by developing, constructing and implementing a source, for cold, conformer separated molecular beams of biological molecules.

1.2 Laser Desorption

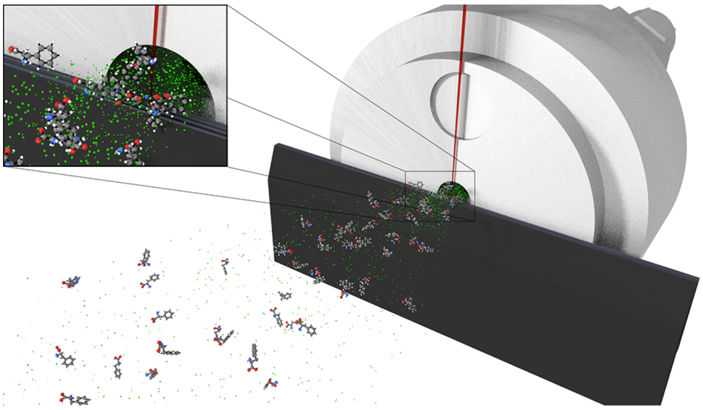

Figure 1.3: Sketch of a laser desorption source. A pulsed laser (red) shoots onto a sample bar (black). Desorbed molecules - here, phenylalanine - are entrained in a supersonic expansion of noble gas (green).

For many biomolecules it is not trivial to produce crystals [2] and they are often also thermally labile, therefore, transferring them into the gas-phase is challenging. Several different techniques have been developed to transfer thermally labile molecules into the gas-phase, for example, matrix assisted laser desorption ionisation (MALDI) [14, 15], laser-induced acoustic desorption (LIAD) [16], and laser desorption (LD) [17, 18]. The latter is closely related to laser ablation [19, 20]. In laser desorption the sample (e. g., a biological molecule such as a peptide) is mixed with a graphite matrix, placed on a substrate and hit by the desorption laser. This is absorbed by the matrix and induces a fast and instant heating on the order of $10^{10} - 10^{12}$ K/s, such that the sample preferentially vaporises instead of fragmenting [21].

Already in 1968 aromatic hydrocarbons and the amino acid Leucin were laser-desorbed and analysed *via* mass spectrometry [17]. Later on laser desorption was combined with pulsed molecular beam sources to directly cool the intact desorbed molecules [22–25]. Furthermore larger molecules, like a nonapeptide [26] or a pentapeptide [27], have been investigated using laser desorption. A detailed characterisation of a laser desorption source was conducted in 1990 by Meijer et al.. They used anthracene, diphenylamine, and perylene entrained in a supersonic expansion after desorption and determined a rotational temperature of 5-10 K and a vibrational temperature of < 15 K [23]. The rotational temperature was determined by the rotational contour of a resonance-enhanced multi-photon ionisation (REMPI) process for anthracene. The vibrational temperature was derived from the relative intensity of a measured hot band in the REMPI spectrum of diphenylamine. For our planed experiments a rotationally colder molecular beam is required and several technical considerations need to be fulfilled, see chapter 3.

The existing laser desorption sources have a huge variety in terms of experimental parameters, such as molecular beam valves, laser parameters and sample preparation. For example the sample can be pressed [17], mixed with graphite [27], or desorbed from metal [23]. Similarly, different lasers have been used to desorb molecules, including wavelengths from the ultraviolet to the infrared [22, 23, 27]. Laser desorption is routinely used in combination with different spectroscopic techniques, for example, resonance-enhanced multi-photon ionisation [24] and infrared-ultraviolet double resonance techniques [28]. These are species-specific spectroscopic techniques and thus are only sensitive to the molecule of interest in the molecular beam. What has to date not been investigated, however, is that in a laser desorbed molecular beam many different species can be present. For example, fragments of the sample produced during the desorption process or material from the matrix in which the molecule of interest was embedded. For the matrix material mentioned above this would be carbon or metal atoms or clusters. The species composition of a laser desorbed molecular beam has never been studied because the impurities in the beam were essentially invisible with the used spectroscopic techniques. We are here for the first time combining laser desorption with strong-field ionisation, which is a non-species-specific universal ionisation technique and allows us to assess the contribution of carbon and sample fragments in the molecular beam. Furthermore, even at the low temperatures achieved using supersonic molecular beams, different structural conformers of biomolecules are present, as they are essentially frozen in their local potential minimum. If laser desorption is to be combined with a non-species-specific technique, for example x-ray diffraction, a separation of these different species in the beam is necessary. This allows the investigation of the structure-function-relationship, for example, of different conformers of a biomolecule. This can be achieved using controlled molecules techniques as outlined in the next section. However, the approaches require rotationally extremely cold molecular beams. Using a special conically-shaped supersonic expansion nozzle we demonstrate the production of molecular beams with rotational temperatures of ~ 2.3 K from laser desorption. This is the coldest temperature to date reported from a laser desorption source and ideally suited for molecular control approaches.

1.3 Controlling Molecules

X-ray diffraction or strong-field ionisation are inherently non-species-selective techniques. In order to gain conformer-specific information requires the different conformers to be separated in space, such that they can be investigated separately. For polar molecules, such as nearly all biological molecules, this can be achieved with strong inhomogeneous electric fields [13, 29–31]. The interaction of the effective dipole moment of a molecule with the electric field leads to a force acting on the molecule, given by $\vec{F} = -\mu_{\text{eff}}(\epsilon) \cdot \vec{\nabla}\epsilon$ [29]. The force $\vec{F}$ depends on the effective dipole moment μ_{eff} and the electric field gradient $\vec{\nabla}\epsilon$. Species with a different effective dipole moment-to-mass-ratio $\mu_{\text{eff}}/\text{m}$ will experience different forces in the field and can thus be spatially separated.

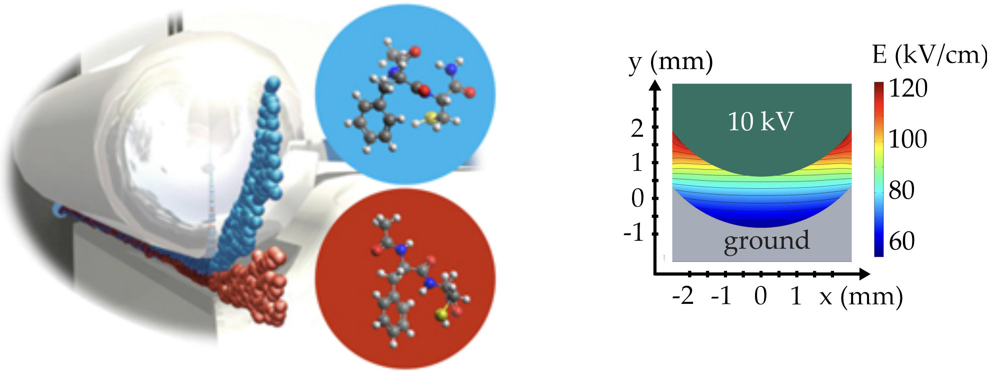

Figure 1.4: Spatial separation of two conformers by the electrostatic deflector and the inhomogeneous electric field throughout the deflector. The molecule shown is the dipeptide Ac-Phe-Cys-NH_2, which has two conformers, indicated in red and blue, with different dipole moments. Figure adapted from [13]

This spatial separation can be achieved with an electrostatic deflector producing an inhomogeneous electric field, as shown in Figure 1.4. Additionally, two conformers are depicted with blue and red spheres, and how their trajectory through the deflector is influenced by the electric field. The molecules in the spheres correspond to the dipeptide Ac-Phe-Cys-NH_2, which was spatially separated as part of this work. This is the first demonstration of electrostatic deflection and conformer separation of a biologically relevant and thermally labile molecule. Previous conformer separation experiments were all conducted using thermally evaporated molecules, with the largest example prior to this work the separation of the conformers of 3-fluorophenol [32] or hydroquinone [33]. So Ac-Phe-Cys-NH_2 is the most complex molecule to be separated with a deflector to date and the first time electrostatic deflection has been combined with laser desorption of a biomolecule. It further represents the first production of a conformer-selected molecular beam of neutral peptides.

In addition to conformer selection molecules can be aligned or oriented in space. Alignment is induced by the interaction of the anisotropic polarisability of a molecule with an AC electric field and alignment, therefore, refers to the fixing of an axis in space, i. e., with no preferred direction. The electric field utilised for alignment is typically provided by a non-resonant laser pulse, which is linearly polarised for 1D alignment or elliptically polarised for 3D alignment [11]. Molecular orientation, furthermore, refers to the definition of a preferred direction of the dipole moment vector, i. e., breaking the up/down symmetry induced by the AC alignment field. Orientation can be achieved with a strong static electric field, this is termed brute force orientation [34, 35], a combination of a dynamic and a static electric field [36, 37], or with multiple AC fields [38, 39]. The degree of alignment or orientation of a molecular ensemble can be determined, for instance, through Coulomb explosion imaging [36, 40]. Alignment and orientation are illustrated in Figure 1.5 for the molecule 2,6-difluoroiodobenzene, showing how isotropic, 1D aligned, and 1D oriented molecules are arranged in space.

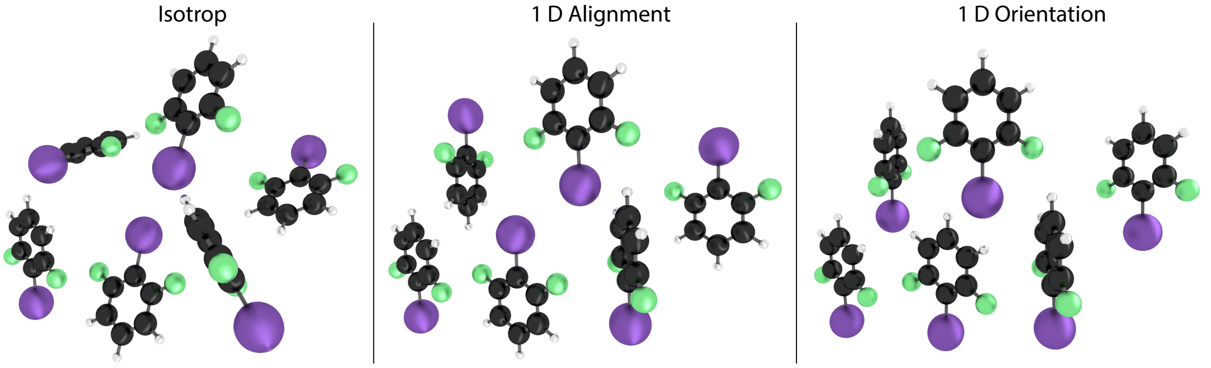

Figure 1.5: Molecular ensembles of 2,6-difluoroiodobenzene molecules for the cases of isotropically distributed molecules, 1D alignment and 1D orientation.

The key advantage of aligned or oriented molecules is that they allow the measurement of molecular-frame data. It enables, for example, diffractive imaging of molecular ensembles [6, 41] or the collection of molecular-frame photoelectron angular distributions [42, 43]. Alignment and orientation also requires rotationally extremely cold molecular samples [36, 44].

1.4 Overview

The first challenge for this thesis was to build a laser desorption source which produces a molecular beam of intact biological systems with a rotational temperature well below

5 K. Such a rotationally cold molecular beam is essential for the implementation of the control techniques described above. The rotational temperature measured previously from a laser desorbed molecular beam was 5-10 K [23]. The second challenge was to apply the electrostatic deflection approach to the produced cold molecular beam of a prototypical biomolecule, and to fully spatially separate the different conformers. Additionally, with this technique all non-polar species in the molecular beam were filtered out and a pure conformer-selected molecular beam of biological molecules was produced. The final challenge was to use a real protein with the novel design of the laser desorption source and to produce a molecular beam of an intact protein.

The theory underlying molecular beams and electrostatic deflection will be briefly introduced in chapter 2. Followed by chapter 3, where the laser desorption source is described in detail with all its functionality and also the considerations that led to the final design are given. Afterwards the laser desorption source is characterised in chapter 4. For the characterisation of the produced molecular beam we used, for the first time, strong-field ionisation, which allowed us to monitor the fragmentation and the entrainment of the desorbed molecules in the molecular beam. This was the first such characterisation of a laser desorption source and these results have been published in the *Journal of Chemical Physics*, details are given in the publication list.

Following from this, the laser desorption source was combined with electrostatic deflection, as described in chapter 5, to spatially separate the two conformers of a dipeptide from each other and from other molecules and carrier gas in the molecular beam. The advantage of this separation is that now the conformers can be investigated individually with non-species-specific techniques and this represents a milestone towards diffractive imaging of individual biomolecules. To our knowledge this was the first time that conformers of neutral peptides have been separated from each other and a conformer-pure molecular beam was produced. Through detailed modelling and simulation of our results we furthermore extracted the rotational temperature from our laser desorption source as ~ 2.3 K, significantly colder than previously reported. These results are submitted to *Angewandte Chemie International Edition*, details are given in the publication list. Furthermore, we have been granted beam time at the FLASH free-electron laser to investigate the conformer specific fragmentation of peptides.

In chapter 6 experiments on glycine are presented. Glycine is the smallest amino acid and an important model system for, e. g., ultrafast electron and charge migration dynamics. Such experiments have long been proposed and have been studied theoretically already in detail [45]. For the proposed experiments, a conformer-pure beam of glycine is needed. This has been achieved for the first time and one conformer of glycine could be spatially separated from the other conformers in the molecular beam. The separation enables novel experiments to investigate the charge migration on glycine, or other conformer-specific interactions, and a manuscript of these results is in preparation.

In chapter 7 the laser desorption source is used to desorb bovine insulin, an intact functional protein. A time-of-flight mass spectrum of the molecular beam is recorded and clear indications for the presence of desorbed insulin were measured.

In the final chapters some improvements for the experimental setup, based on the experience gained, are suggested, a summary of experiments performed is given, as well as an outlook with suggestions for new experiments enabled by the novel combination of laser desorption with electrostatic deflection.

2 Fundamental Concepts

In this short theory section a brief overview of the fundamental concepts needed to understand the work in this thesis is given. In particular, the rotational states of molecules, supersonic molecular beams and the behaviour of molecules in electric fields are described. Further details can be found in textbooks [46–50] and recent reviews [29, 51].

2.1 Rotational States of Molecules

For the measurements performed in this thesis the rotational state population of a molecule plays an important role. Given here is a basic treatment of molecular rotations, always assuming the approximation of the rigid rotor model. This assumes that the nuclei are connected by a weightless and rigid rod and thus the distance between the nuclei is not changing during the rotation. The rotation is performed around the molecular centre of mass and can be described with the moments of inertia, I, and reduced mass μ. For the simple case of a diatomic molecule, these are given by:

$$I = \mu r^2, \qquad \mu = \frac{m_1 m_2}{m_1 + m_2}$$

In general, molecules can possess three distinct moments of inertia around their three principal axis. These are characterised by their corresponding rotational constants A, B and C of a molecule,

$$A = \frac{h}{8\pi^2 I_a}, \qquad B = \frac{h}{8\pi^2 I_b}, \qquad C = \frac{h}{8\pi^2 I_c}.$$

Here a, b and c denote the principal axes of the molecule.

Molecules can be classified as one of four kinds of molecular rotors depending on their symmetry and thus also on the moment of inertia for the three principal axis. The four kinds of rotors are the linear rotor, the spherical rotor, the symmetric rotor and the asymmetric rotor, as shown in Figure 2.1. The linear rotor, e. g., a diatomic, is the simplest one and the moments of inertia in this case are $I_c = I_b, I_a = 0$. For a linear rotor there is only one distinct rotation; we use the total rotational angular momentum quantum number J, to label the states.

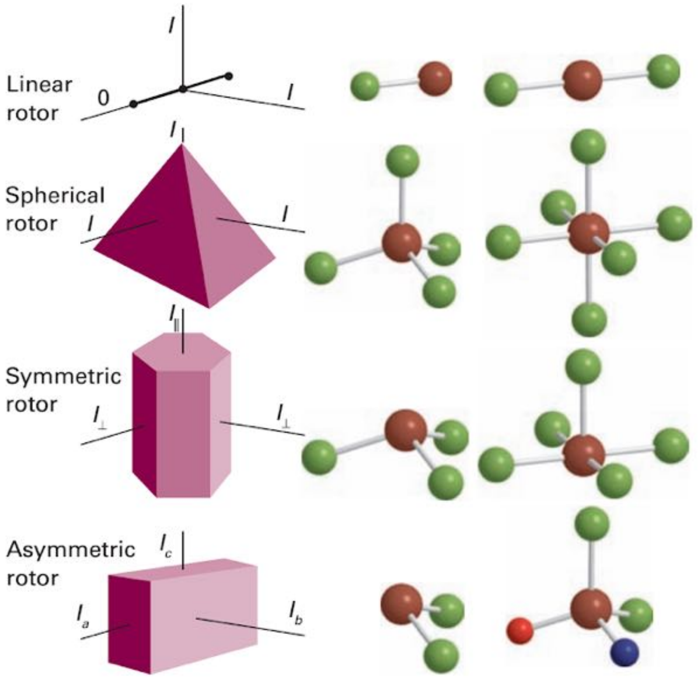

Figure 2.1: The four different kinds of molecular rotors, with their principal axes and corresponding moments of inertia indicated. Figure adapted from [52]

The molecules investigated in this thesis are asymmetric rotor molecules, as are most molecules. This means that the three principal moments of inertia have different values, and by convention $I_c > I_b > I_a$. Water, for example, is an asymmetric rotor molecule and is shown in Figure 2.2 with its three principal axes and the corresponding moments of inertia highlighted. [48–50]

Describing the rotations of an asymmetric rotor is a complex problem and no general

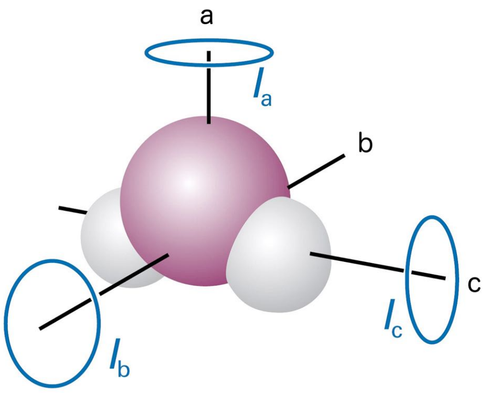

Figure 2.2: A water molecule, an asymmetric rotor, with its principal axis (a, b, c) and the principal moments of inertia around them (I_a, I_b, I_c). Figure adapted from [50]

analytic solution exists. To describe the rotational states of a asymmetric top molecule we typically use the quantum number J for the total rotational angular momentum and two pseudo quantum numbers K_a and K_c. The latter are projections of the total rotational angular momentum onto the principal molecular a and c axes. Note that, although not discussed here in detail, these projections correspond to the approximation of an asymmetric rotor to the limiting cases of an oblate or prolate symmetric rotor. The density of rotational states for each rotational angular momentum J is much higher for the asymmetric rotor than for the linear rotor, namely $2J+1$ distinct states exist. [54, 55]

Additionally to the higher number of rotational states for each J in an asymmetric rotor, the rotational states for larger molecules are also closer together due to the larger inertia and hence smaller rotational constants. This means that significantly more rotational states are populated at the same rotational temperature for larger molecules than for small molecules. For example, Figure 2.3 shows the relative population of the different J states for one conformer of the dipeptide Ac-Phe-Cys-NH_2 investigated in chapter 5 for four different temperatures. These were calculated assuming a Maxwell-Boltzmann distribution of rotational energy and using the rotational constants for Ac-Phe-Cys-NH_2 of $A = 340.18$ Mhz, $B = 203.44$ Mhz and $C = 159.88$ Mhz, for more details see chapter 5. It is clear that even with a slight increase of the temperature the relative population gets significant broader and more states are populated. Taking into account that there are

$2J+1$ distinct states for each J, there is a total of 2601 rotational states in the range of $J = 0 - 50$ (in the absence of external fields). This can be compared with, e. g., OCS, which is a linear rotor with $B = 6081.49$ Mhz [53]. In this case at 2.5 K 95% of the population is in the $J = 0 - 5$ states. [29, 54]

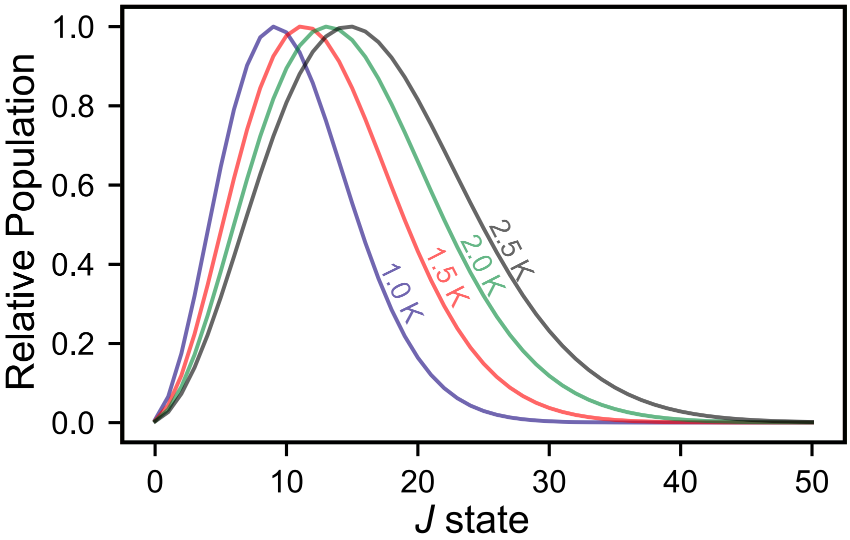

Figure 2.3: The relative population of J states for four different rotational temperatures of the dipeptide Ac-Phe-Cys-NH_2.

Furthermore, in the presence of an external field the degeneracy of the quantum number M, the projection of the rotational angular momentum on the field axis, is lifted and each rotational state splits into $2J+1$ states with $M = -J, ..., J$. For the case of an electrostatic field, as used in this thesis, states with $-M$ and $+M$ are still degenerate, i. e., states are split with $|M|$. This splitting means that for the case of the dipeptide considered above 89726 distinct states exist in the range $J = 0 - 50$ in the presence of an electric field. [48, 49, 54, 55]

2.2 Supersonic Molecular Beams

Due to the large number of rotational states that become populated with increasing temperature, the efficient cooling of molecules in the gas-phase is highly desirable to simplify molecular spectra and to enable conformer separation utilising the Stark effect.

One way to achieve this is using supersonic molecular beams. A molecular beam is produced with a gas reservoir held at a certain pressure, usually several bar, which has an orifice larger than the mean free path of the molecules in the gas reservoir. On the outside of the reservoir is high vacuum, typically below 10^{-5} mbar. The molecules now expand from the reservoir into the high vacuum region. As they fly through the orifice, and in a short distance behind the orifice, they collide with each other, transferring the internal energy of the molecules to kinetic energy, as shown in Figure 2.4. [49, 56–58]

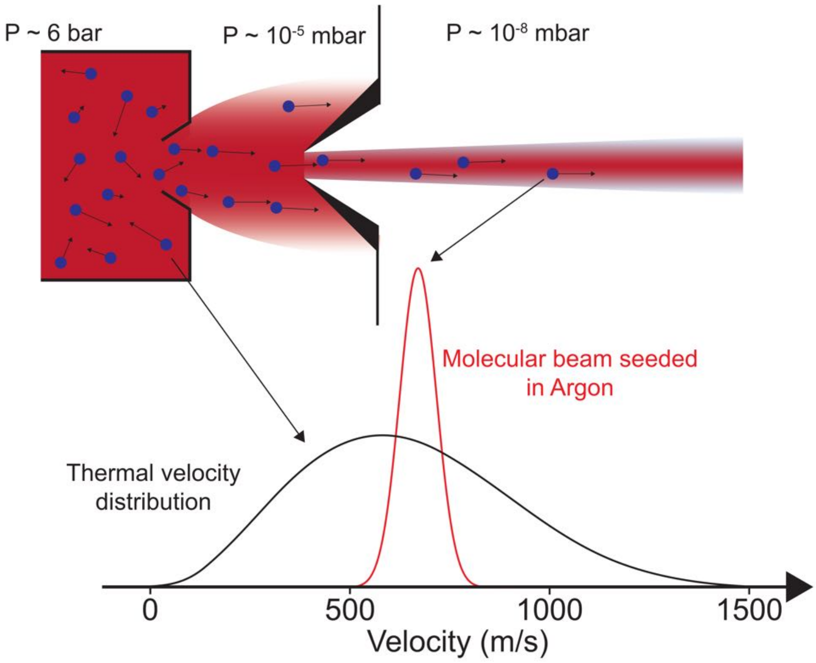

Figure 2.4: Sketch of a supersonic expansion molecular beam source. Molecules, typically mixed with a noble seed gas, expand from a high-pressure reservoir into vacuum. In the vicinity around the orifice the molecules internal energy is converted into directed forward motion, forming a fast molecular beam with a high velocity but narrow velocity spread. Additionally the thermal velocity distribution inside the reservoir before the expansion and of a molecular beam seeded in argon is shown.

The random thermal motion in the reservoir is thus converted to directed forward motion in the molecular beam. The translational temperature is defined by the width of the velocity distribution of the molecular beam and not by its total velocity. Due to the collisions in the molecular beam the velocity distribution of the molecules in the molecular beam is narrow, i. e., all molecules are travelling with the same velocity, and typically corresponds to translational temperatures of <1 K [56]. Due to the inelastic collisions during the expansion the internal degrees of freedom are also cooled, i. e., the vibrational and rotational temperature decreases. The achievable rotational temperature of the beam is close to the translational temperature, but the vibrations of the molecules are cooled less efficient and thus the achievable vibrational temperature is typically < 15 K [23] in laser desorption. A colder temperature for the vibrations and rotations means that fewer states are populated, which leads to simpler spectroscopic spectra, reduces the Doppler broadening of the spectral lines and in our case the colder rotational temperature leads to better conformer separation in space. How cold a molecular beam can be is limited by the cluster formation of the cooled molecule [59]. To shift this limitation towards colder molecular beams the molecules can be mixed with a noble gas, which reduces the cluster formation. [49, 56–58]. In this work pulsed molecular beams with a repetition rate of 20 Hz are used, with helium or argon as seed gas.

2.3 Electrostatic Deflection

Controlling neutral molecules in the gas-phase, such as the separation of different conformations in space, requires a 'handle' on these molecules. One possibility is the use of the distinct molecular dipole moments which can interact with external fields [13]. In this work the separation of molecular conformers is performed using the Stark effect, which is the interaction of a molecular dipole moment with an external electric field.

First the classical behaviour of a molecular dipole in an inhomogeneous electric field is considered and shown in Figure 2.5. A force acts on the molecule with the permanent dipole and it will orient in the field. But the forces pulling the molecule towards the electrodes cancel out and thus the molecule is moving to neither of the electrodes. However, due to the curvature of the electric field lines in an inhomogeneous field the forces acting on the molecule do not cancel out fully and there is a net force which is dragging the molecule towards the stronger fields. The classical dipole is a so called 'strong-field-seeker' and will always move towards higher field strengths.

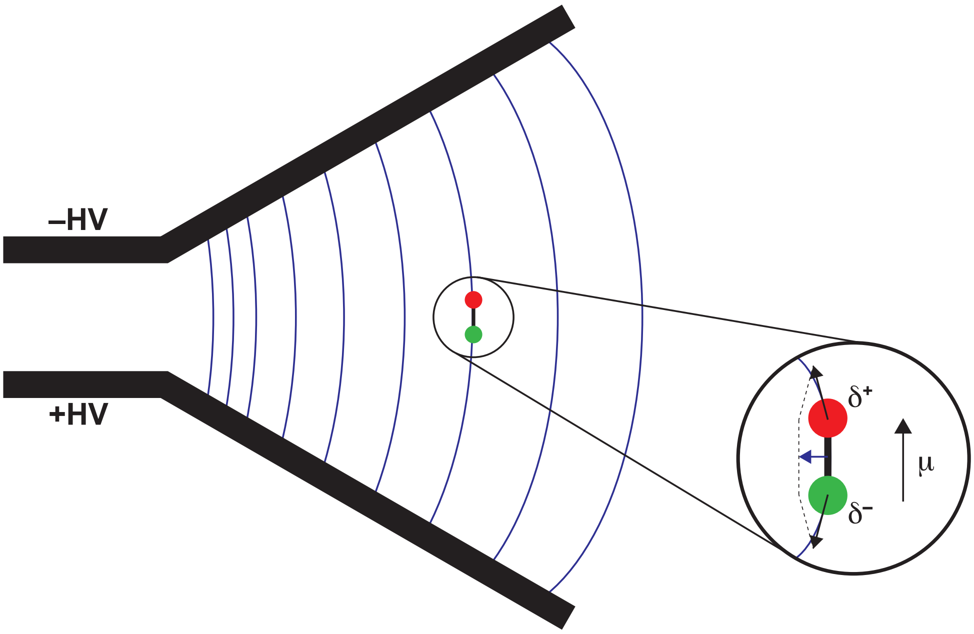

Figure 2.5: A classical picture of the forces acting on a molecular dipole in an inhomogeneous electric field.

This is a simple classical picture and in reality molecules exhibit a quantum-state specific behaviour, for example there are also states which are weak field seekers for which there is no classical equivalent. However, large molecules in strong fields approach the classical limit and are strong-field-seekers, much like the classical picture.

In quantum mechanics the Stark interaction for rigid-rotor molecules can be described by only considering the rotational degrees of freedom of a molecule. We describe the overall rotational Hamiltonian as the sum of the rigid-rotor Hamiltonian, $\mathbf{H}_{\text{rot}}$, and the Stark Hamiltonian, $\mathbf{H}_{\text{Stark}}$, leading to: [54]:

$$\mathbf{H} = \mathbf{H}_{\text{rot}} + \mathbf{H}_{\text{rot}}$$

Where $\mathbf{H}_{\text{rot}}$ can be described, using the total rotational angular momentum operator $\mathbf{J}$ around the principal axes a, b and c, as [54]:

$$\mathbf{H}_{\text{rot}} = h(A\mathbf{J}_a^2 + B\mathbf{J}_b^2 + C\mathbf{J}_c^2)$$

For an asymmetric rotor molecule this equation cannot generally be solved analytically. To solve these issue a numerical calculation is performed using symmetric top wave functions to obtain asymmetric top eigenfunctions.

The Stark interaction $\mathbf{H}_{\text{Stark}}$ is predominantly determined by the interaction of the electric field $\vec{\epsilon}$ with the dipole moment $\vec{\mu}$ and given by [54]:

$$\mathbf{H}_{\text{Stark}} = -\epsilon \sum_{g=x,y,z} \mu_g \phi_{Z_g}$$

where x, y, z represent a molecule-fixed coordinate system, μ_g represents the dipole moment components along the molecule-fixed axes x, y, z and ϕ_{Z_g} are the direction cosines of the molecular axes with reference to the space-fixed X, Y, Z-axes, with Z being oriented along the electric field direction. The influence of higher order effects is very minor and is thus neglected.

To solve the Hamiltonian $\mathbf{H}$ for the rotation including the Stark interaction, it is transformed to a symmetrised matrix using the Wang transformation, diagonalised for different field strength to obtain the eigenstates and afterwards interpolated between the calculated energies. [54]

The Stark effect for molecules can be calculated as outlined above using the freely available `CMIstark` package [54], developed and maintained by our group. Two examples of Stark calculations are shown in Figure 2.6 for the linear rotor OCS (a) and the asymmetric rotor indole (b).

The left side of Figure 2.6 shows the dependence of the Stark energy W_{Stark} given as

$$W_{\text{Stark}} = -\vec{\mu} \cdot \vec{\epsilon} = -\mu\epsilon\langle\cos\theta\rangle = -\mu_{\text{eff}}\epsilon$$

on the applied electric field, ϵ. here $\vec{\mu}$ is the permanent dipole moment, $\vec{\epsilon}$ is the applied electric field, and θ the angle between the two vectors. Quantum mechanically, $\langle\cos\theta\rangle$ acts as a mixing operator and couples rotational states with equal M but $J \pm 1$, resulting in the

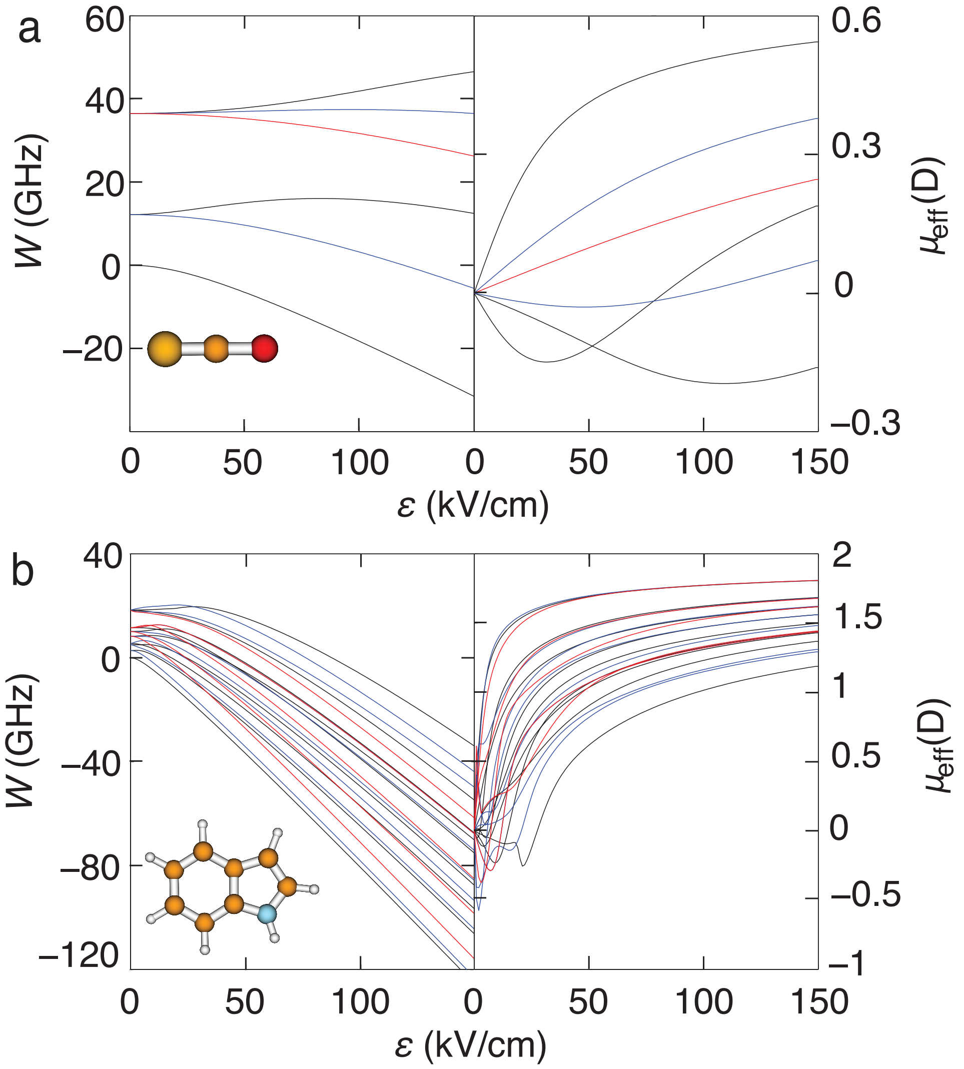

Figure 2.6: The energy shift W and the effective dipole moment μ_{eff} in dependence of the electric field ϵ for the linear rotor OCS (a) and the asymmetric rotor indole (b). The $J = 0 - 2$ states are plotted with the corresponding $M = 0$ (black), 1 (blue) and 2 (red) states. Figure adapted from [29]

formation of so-called pendular states. Since the expectation value $\langle \cos\theta \rangle$ is quantum-state dependent, so is the effective dipole moment, μ_{eff}, the dipole moment projected on the field axis.

On the right side of Figure 2.6 the dependence of the effective dipole moment, μ_{eff} on the applied electric field is shown. The effective dipole moment is defined as the first derivative of the Stark shift with respect to the field and is given as [29]

$$\mu_{\text{eff}}(\epsilon) = -\frac{\partial W}{\partial \epsilon}$$

In the absence of external fields, all M states of a molecule, i. e., the projection of the angular momentum onto the field axis, are degenerate. This leads to a spherical angular probability density and hence $\langle \cos\theta \rangle = 0$. Therefore there is no effective dipole moment in field-free space.

The presence of an electric field removes this degeneracy of M states. For relatively weak fields, for example as commonly used in Stark spectroscopy, the Stark interaction can be treated perturbatively and approximate analytical expressions derived [48]. This is not the case for the strong fields used in this thesis, where the Stark effect mixes, or hybridizes, different wave functions leading to $\langle \cos\theta \rangle \neq 0$. Therefore, in dependence of the strengths of the inhomogeneous electric field molecules will feel a force and move. The force acting on the molecule is given by [29]

$$F = -\vec{\nabla} W = -\mu_{\text{eff}} \cdot \vec{\nabla} \epsilon$$

Therefore, using appropriate inhomogeneous electric fields allows us to manipulate molecules in space, such as spatially separating different conformers. [29]

In Figure 2.6 the $J = 0 - 2$ rotational states are shown. On the left side of the plot the field-free states, i. e., $\epsilon = 0$ are shown. For the linear rotor OCS this means a single energy level for each given J. Increasing the electric field splits up the J states according to the projection quantum number M. The different M states are indicated with different colours, were $M = 0$ is black, $M = \pm 1$ is blue and $M = \pm 2$ is red. It is clearly visible that the energies for the rotational states shift considerably in the electric field, which cannot be considered a small perturbation any more. In the case of OCS there are some states which, over the range of field strengths, lower their energy at higher field strength, which means they are so-called strong-field-seekers. Therefore, these molecules will move towards

stronger field strength in an inhomogeneous electric field. Conversely, some states have higher energies in the stronger electric fields making them weak-field-seekers. [29]
For the case of the asymmetric rotor indole the Stark curves become much more complicated, due to the much higher density of states, as shown in Figure 2.6 b. Here again the states with $J = 0 - 2$ and $M = 0 - 2$ are shown. Due to the much higher density of states in larger asymmetric rotor molecules, the separation of single quantum states is not feasible any more. However, different conformer structures, possessing differing permanent dipole moments, can still be separated. [29, 54]

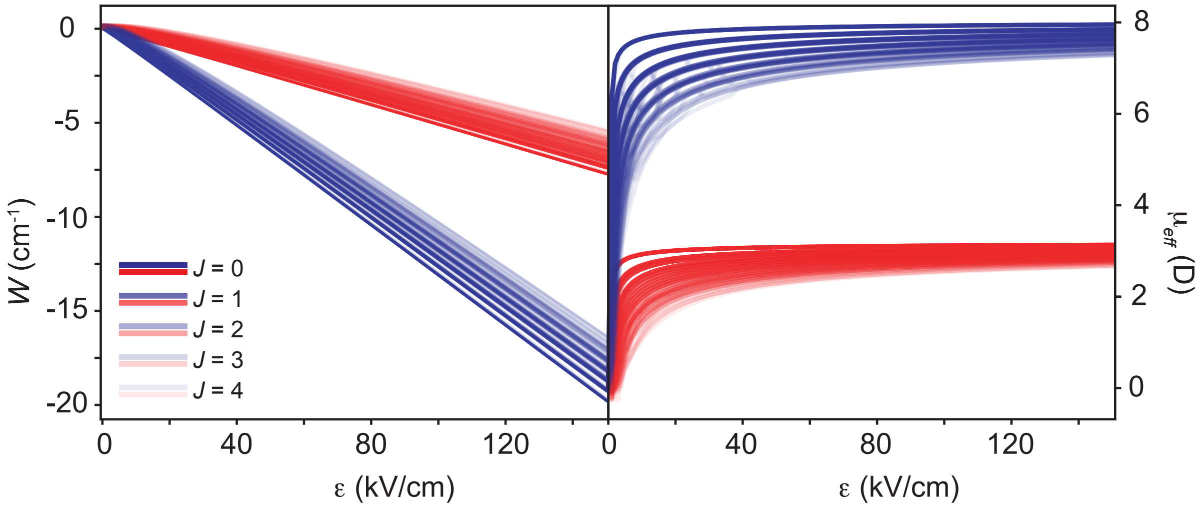

Figure 2.7: Stark calculations for the two conformers of the dipeptide Ac-Phe-Cys-NH_2 for the $J = 0 - 4$ states. The different conformers are shown in red and blue, while different opacities indicate the corresponding J state.

In the following Stark plots in this thesis the different conformers are therefore coloured differently. The different J states are indicated by a different opacity and the different M states are shown in the same colour and opacity as the J state they originated from, as depicted in Figure 2.7, for the two conformers of Ac-Phe-Cys-NH_2 (see chapter 4 and chapter 5 for more details). Even though it is not possible to distinguish every quantum state, a clearly different behaviour for the two conformers depicted in red and blue is visible and they can thus be separated. Additionally it is evident that the lower lying rotational states, shown with higher opacity, experience a larger influence of the electric field than the higher rotational states.

3 Experimental Setup

In this work a new laser desorption source was designed, set up and characterised. Several important requirements had to be fulfilled with the new design. These requirements are given in the first part of this chapter. Additionally, the experimental setup and the sample bar preparation is described in detail.

3.1 Laser Desorption Source Design — Considerations

Our laser desorption source needed to fulfil different requirements than previous designs, because we want to perform diffraction experiments. As this is a non-species-specific technique it is sensitive to all contaminants in the beam. Therefore, a cold molecular beam of identical molecules intersecting the x-ray beam is needed. In this section the design, functions, and characteristics of our new source are described in detail. Furthermore, some background information for the considerations taken into account for the design of the source are given.

3.1.1 Source Mobility

For diffraction experiments at free-electron lasers, the molecular beam needs to be fully translatable in the *xyz*-direction, because the x-ray beam cannot be moved easily, hence the molecular beam needs to be adjusted to the x-ray beam. Additionally if conformers are spatially separated they are at different positions in the molecular beam and need to be adjusted to the x-ray beam, accordingly. To ensure this adjustment the complete laser desorption source was fixed on a rod connected to a 3D-manipulator and is, therefore, moveable in xyz from outside vacuum. Furthermore, the desorption laser was coupled into a fibre, which was fed into vacuum and connected to a collimator fixed at the source. Thus the desorption laser and the source move together and no more adjustment of the laser is needed for new source positions.

3.1.2 Sample Bar Height

The sample bar was adjusted approximately 200 µm in front of the molecular beam valve and is partially blocking the exit of the valve. The molecules desorbed from the sample bar are picked up by the expansion of a noble gas from the valve and transported through the chamber, forming a molecular beam. So the height of the sample bar with respect to the valve is a crucial parameter to achieve stable signal. Hence a straight sample bar and not a rod or pellet is used. The sample bar was ground after each use, see section 3.4, to ensure it had the same height everywhere. Since the height is so crucial and needs to be optimised on signal during the measurement, the movement of the sample bar in the x-direction is motorised.

3.1.3 Sample Bar Replenishment

As molecules on the sample bar are vaporised after interaction with the desorption laser, the molecules need to be replenished continuously to continue the measurement. A long sample bar was build, which was continuously moved to ensure fresh molecules were desorbed for each laser spot. For a slow and steady movement of the sample bar the y-direction is also motorised.

3.1.4 Sample Bar Exchange

Since the sample bar is moved during the whole measurement in the y-direction, it eventually needs to be exchanged with a fresh one. To minimise the number of exchanges the sample bar should be as long as possible considering the travelling distance and size of the vacuum chamber. This led to a 80 mm long sample bar. Furthermore, sample bar exchange should be as fast as possible, as no data can be recorded during this time. Therefore, a load-lock system was build, which allows a faster sample bar exchange into and out of vacuum. The load-lock is a small chamber connected to the source chamber. Thus only the small load-lock chamber needs to be vented, ensuring the required vacuum conditions in the molecular beam machine shortly after exchange.

3.1.5 Cold Beam

To separate different conformers in a molecular beam requires a low rotational temperature, typically of a few Kelvin [29]. Additionally, for diffraction experiments a molecular beam with high density is desirable to enable a measurement in a realistic time. For measurements at the Linac Coherent Light Source (LCLS) it has been demonstrated that a density of approximately 10^8 cm^{-3} is sufficient [6, 60]. To achieve a cold and dense molecular beam of a biomolecule a pulsed valve was mounted behind the sample bar. The supersonic expansion of a noble gas from this molecular beam valve entrains the laser desorbed biomolecules and cools them down. We use a piezo electric valve with a conical shaped front plate, which has been shown to provide colder and denser beams [61].

3.1.6 Desorption Laser

Since the desorption laser should be mainly absorbed by the graphite and not by the biomolecule of interest, the wavelength should be chosen accordingly. The combination of a Nd:YAG laser at the fundamental wavelength of 1064 nm with a sample-graphite mixture has proven to be functional before [62]. Additionally, the shot-to-shot fluctuations should be as low as possible to ensure signal stability, which makes a diode-pumped laser more suitable. The repetition rate is strongly coupled to the sample bar length and thus the measurement time for one sample bar, we have used 20 Hz as a good compromise and because this fits to existing laser systems.

3.2 New Source Design - Technical Realisation

An overview of the entire new source assembly is shown in Figure 3.1. For better visibility and understanding, the laser desorption source is split up in five sub-assemblies: the sample bar assembly, the supersonic expansion valve, the laser fibre coupling, the mechanical hinge, and the load-lock and sample bar exchange mechanism, which are described in the following sections.

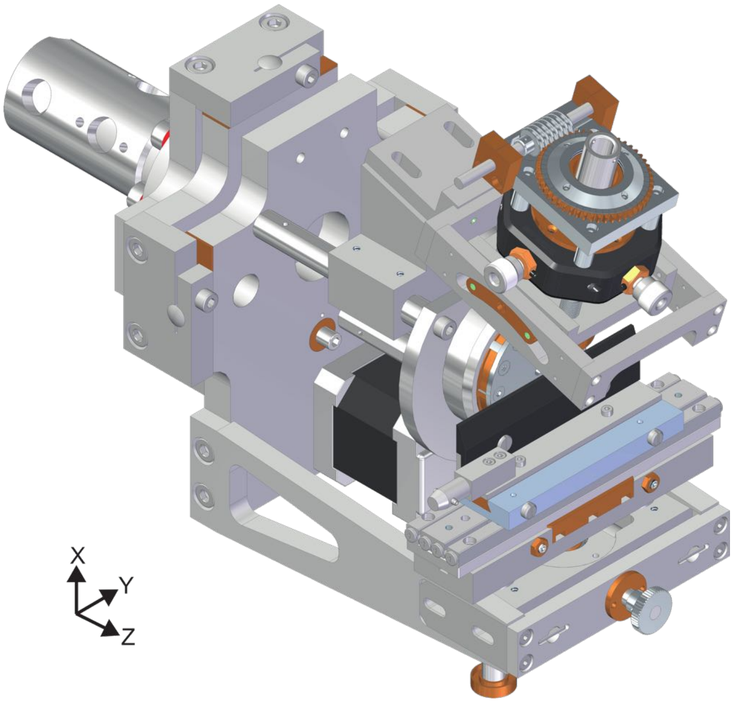

Figure 3.1: Complete design of the new laser desorption source. At the following explosion images the functions are described in detail. This setup is always shown at the top right corner, with the exploded detail highlighted in red.

3.2.1 Sample Bar Assembly

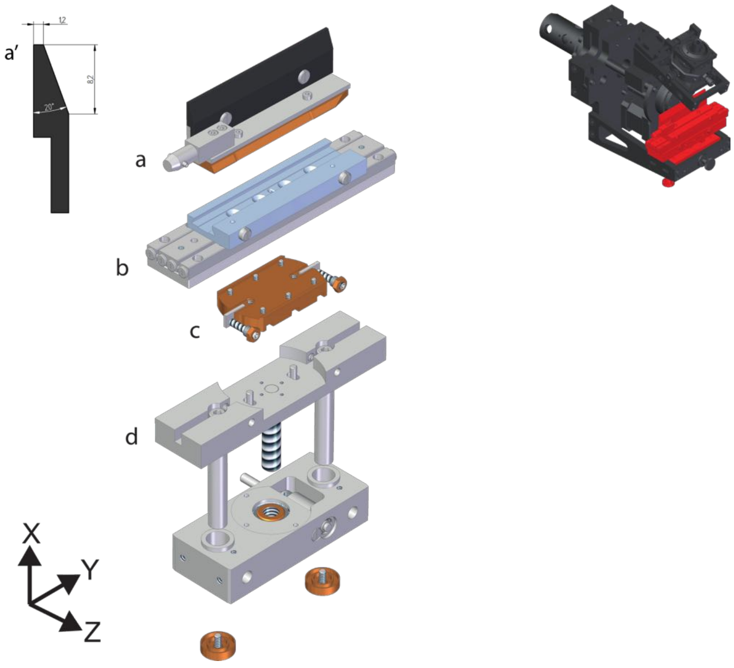

Figure 3.2: The sample bar assembly consisting of the sample bar unit (a), a SmarAct translation stage (b), the bronze angle movement piece (c) and the platform with gear and spiral (d). Additionally a cross section of the graphite for the sample bar (a') is shown.

The sample bar assembly consists of four parts, shown in Figure 3.2, and was mounted in front of the valve. The sample bar unit itself (a) also consists of four parts. A graphite sample bar made from POCO EDM1 graphite, a really fine and hard type of graphite, that was previously used for laser desorption [63]. The cross sectional area of the sample bar is shown in Figure 3.2 a'. On the left side the valve is placed, with the sample bar blocking the orifice at approximately the centre. The sample is deposited on top on a 1.2 mm wide channel. From the top downwards the sample bar broadens with an angle of 20 °, as indicated in Figure 3.2 a'. This chamfered shape of the sample bar is designed to minimise disturbance of the supersonic expansion from the valve [63]. On the lower left side the sample bar was fixed to an aluminium angle, such that the two are flush at the left side. This allows adjustment of the sample bar unit very close to the valve, to approximately two hundred micrometer, which ensures more efficient cooling of the desorbed molecular plume. The aluminium angle itself was fixed on a bronce rail. For fast and easy exchange a bayonet catch was mounted on the aluminium angle.

The second part of the sample bar assembly is a SmarAct translation stage (SLC-24120-S-HV), Figure 3.2 b, which provides motorised movement in the y-direction. On the SmarAct stage a rail was mounted, fitting to the rail on the sample bar unit, allowing removal of the sample bar in the y-direction.

The SmarAct stage itself was mounted on a bronze piece, which permits an angle movement in the YZ-plane, Figure 3.2 c. This movement allows one to adjust the sample bar parallel to the valve front plate, to ensure constant distance between the valve and sample bar during y-translation.

The last part of the sample bar assembly is a platform, Figure 3.2 d, which all parts were mounted onto. It furthermore contains a gear connected to an Owis stepper motor (SM.255.V6), Figure 3.7 d, which allows motion of the entire platform in the x-direction, thereby adjusting the height of the desorbed molecular plume relative to the expanding noble gas and influencing the cooling and entrainment in the molecular beam. One turn of the motor equates to 0.2 mm linear movement of the platform.

3.2.2 Supersonic Expansion Valve

The valve used is an Amsterdam Cantilever Piezo valve [64], Figure 3.3 c, with a 300 µm orifice followed by a conical shaped front plate with a conical opening of 4 mm diameter and 40° opening angle. The valve was fixed with a bronze clamping ring, Figure 3.3 b, to a holder, which was mounted with three rods, Figure 3.3 a, to the front plate of the mechanical hinge, Figure 3.7 c. On the two upper rods the laser fibre coupling unit was fixed. Additionally, the holder has been designed such that the valve can be quickly exchanged for an Even-Lavie valve, as shown in Figure 3.3 d, which produces colder supersonic expansion beams [65].

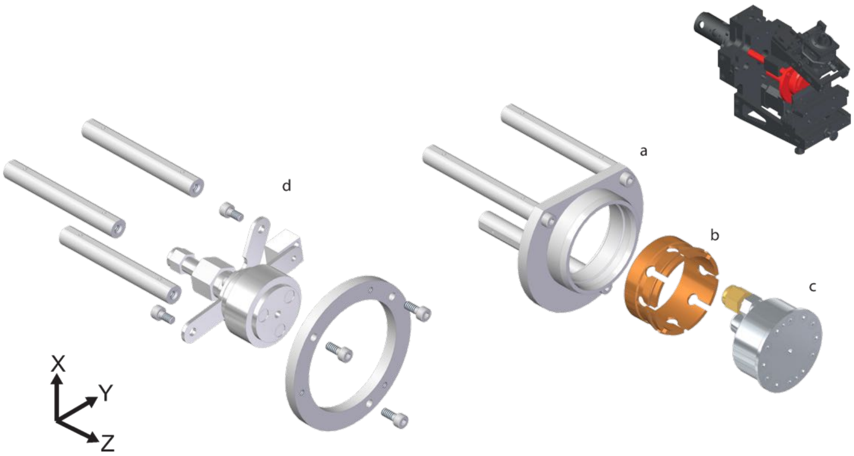

Figure 3.3: Supersonic expansion valve assembly. A piezo valve (c) is held by a bronze clamping ring (b) in a holder with three rods (a). Alternatively, an Even-Lavie valve (d) can be mounted onto the same three rods.

3.2.3 Laser Fibre Coupling

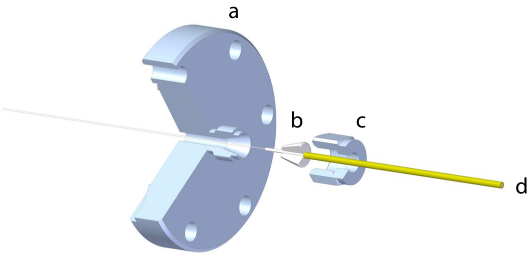

Figure 3.4: The fibre feedthrough with the SwageLock CF40 flange (a), the PTFE plug (b), the SwageLock nut (c) and the optical fibre (d).

The desorption laser is a nanosecond Nd:YAG laser (Innolas, DPPS10) operating at 20 Hz. The power was reduced to less than 1 mJ/pulse, as required for laser desorption, and the laser was coupled into a 400 µm (CeramOptec WF 400/440P) fibre. The fibre is transferred into vacuum with a custom made feedthrough, Figure 3.4 [66]. This consists of a SwageLock nut, a custom made PTFE plug and a CF40 flange containing a corresponding SwageLock connection. This fibre feedthrough allowed us to reach pressures below 5 x 10^{-8} mbar. Laser desorption requires a laser beam loosely focused to a diameter of around 1 mm, nearly matching the width of the sample bar. This was achieved by first collimating the output from the fibre with two lenses (NA = 0.25, f = 36.6 mm, Thorlabs) and afterwards focusing with an aspherical lens (NA = 0.4, f = 31.25 mm, Edmund Optics, 49115). This collimator assembly is shown in Figure 3.5.

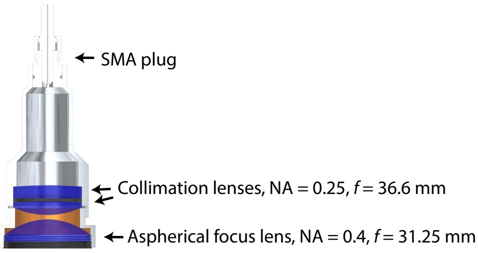
SMA plug
Collimation lenses, NA = 0.25, f = 36.6 mm
Aspherical focus lens, NA = 0.4, f = 31.25 mm

Figure 3.5: A cross-section of the fibre collimator and used optics.

The fibre collimator was fixed on a $Y'Z'$-translational stage, Figure 3.6 c, such that the desorption laser spot can be adjusted to the centre of the noble gas expansion and the sample bar channel. This is important to optimise entrainment of desorbed molecules in the supersonic gas expansion. The desorption laser focus can be manually adjusted by moving the fibre collimator in the x'-direction as shown in Figure 3.6.

The laser fibre collimator assembly was fixed to a plate with curved rails at either side. The angle of the desorption laser shooting on the sample bar can be varied in the $X'Y'$-plane by manual movement along the curved rails. As the laser cone emitted from the collimator is very broad, the angle needs to be adjusted, such that the laser is not hitting the valve. The complete laser fibre coupling unit was fixed to two of the rods holding the valve, Figure 3.3 a, and can be translated along them in the z-direction, providing an approximate adjustment of the desorption laser to the centre of the sample bar.

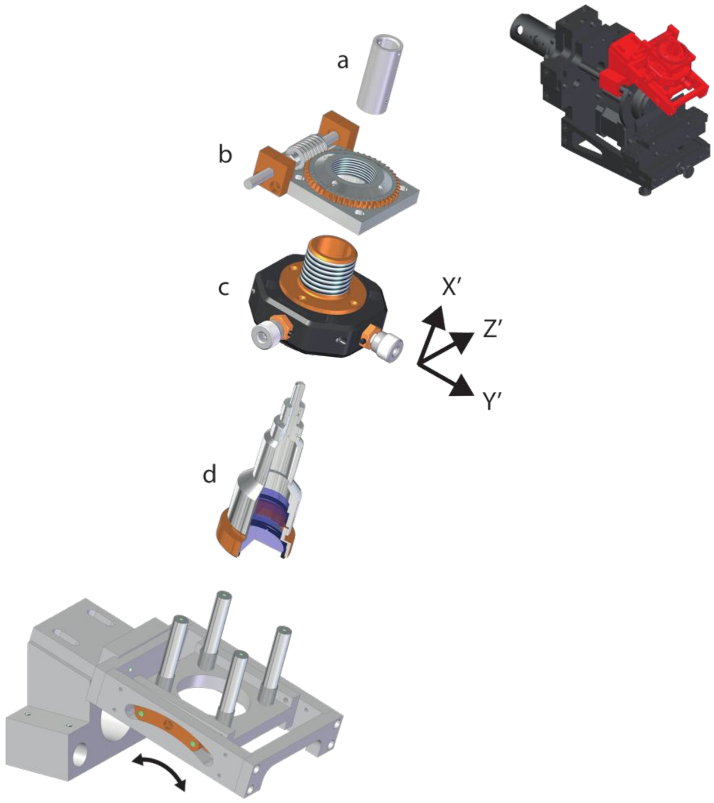

Figure 3.6: Explosion image of the laser fibre coupling unit containing a device to install the fibre (a), a plate with a spiral and gear (b), a *Y'Z'*-translational stage with a thread on top (c), a fibre collimator (d) and a holder for the fibre coupling (e). The coordinate system *X'Y'Z'* is rotated with respect to the coordinate system *XYZ* used before.

3.2.4 Mechanical Hinge

The entire laser desorption source was fixed to a rod, see Figure 3.1, which can be moved in the xyz-direction with a 3-axis linear manipulator. On this rod three plates, Figure 3.7 a - c, were mounted, which allow an angle movement of the source in the XZ and YZ-planes. The complete laser desorption source can thus be adjusted in 5 axis, without changing any alignment of the source itself so that it can be aligned to the x-ray beam in future measurements.

The sample bar assembly was mounted on the third plate using a retainer, Figure 3.7 e. The

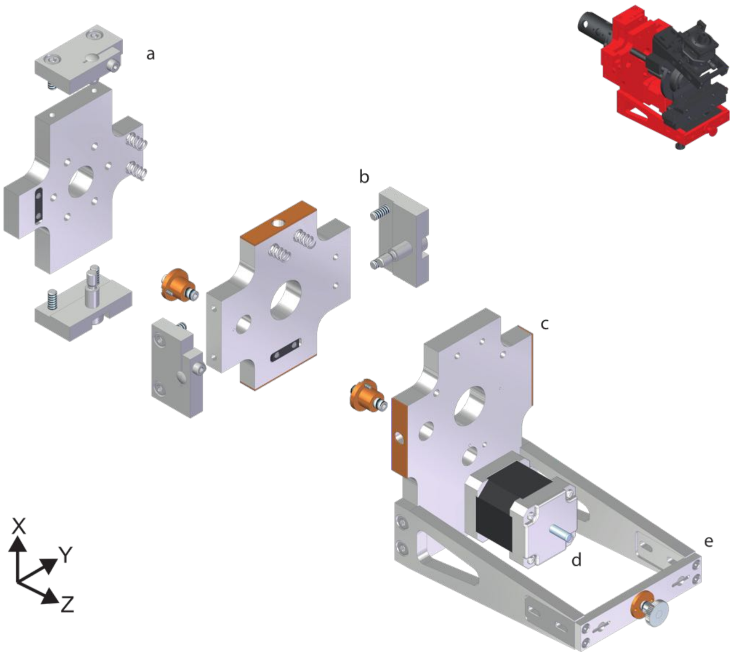

Figure 3.7: The mechanical hinge consists of three plates (a,b,c), which can be moved with respect to each other, an Owis stepper motor (d) and a holding construction for the sample bar assembly (e).

use of elongated holes allows the sample bar assembly some play in the z-direction, giving the possibility to align the sample bar as close as possible to the molecular beam valve. This is important to ensure optimal cooling by entrainment of the desorbed molecules in the densest part of the molecular beam.

3.2.5 Load-lock and Sample Bar Exchange

The load-lock chamber is attached to the source chamber and is separated from it by a mechanical gate valve, as shown in Figure 3.8. This allows a fast sample bar exchange by using a transfer-rod with a bayonet catch which can be engaged to the corresponding part of the sample bar. The sample bar can thus be transferred in the load-lock, which is then isolated from the source chamber, vented, and the sample bar is exchanged. The turn-around time for a sample bar exchange is around 15 min.

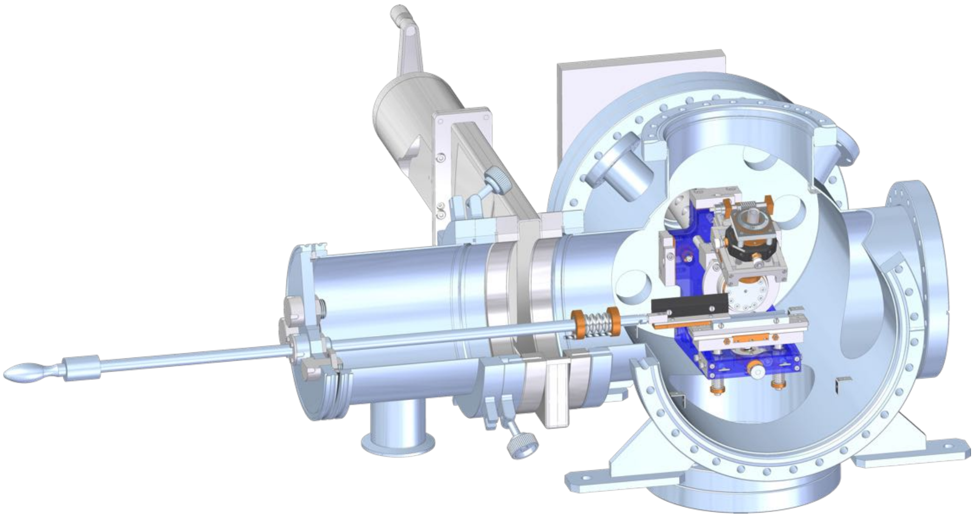

Figure 3.8: Laser desorption source during sample bar exchange, shown from the front. The gate valve is opened and the sample bar unit is shown already connected to the transfer-rod with the bayonet catch and is pulled out of the rail on the SmarAct stage.

3.3 Integration in the Molecular Beam Setup

The overall molecular beam setup consists of three differentially pumped vacuum chambers; a source chamber containing the laser desorption source and a 2 mm skimmer (Beam Dynamics, Model 50.8) mounted 75.1 mm downstream the laser desorption source. Through the skimmer the molecular beam enters the differentially pumped deflection chamber. After a second skimmer of 1 mm diameter (Beam Dynamics, Model 2) the molecular beam enters the 15 cm long deflector [29]. Then the third and last skimmer (Beam Dynamics, 1.5 mm diameter, Model 2) is reached, which separates the differentially pumped deflection and detection chambers. In the detection chamber the molecules are ionised via either strong-field ionisation induced by a 35-fs laser system or via resonance-enhanced multiphoton ionisation using ultraviolet light from a dye laser system. The produced positively charged ions are accelerated to the detector by the electric field of the velocity-map imaging electrodes [67, 68]. The current produced by the impact of the ion on the micro-channel plate is detected as a function of the ion time-of-flight, which yields the mass spectrum of

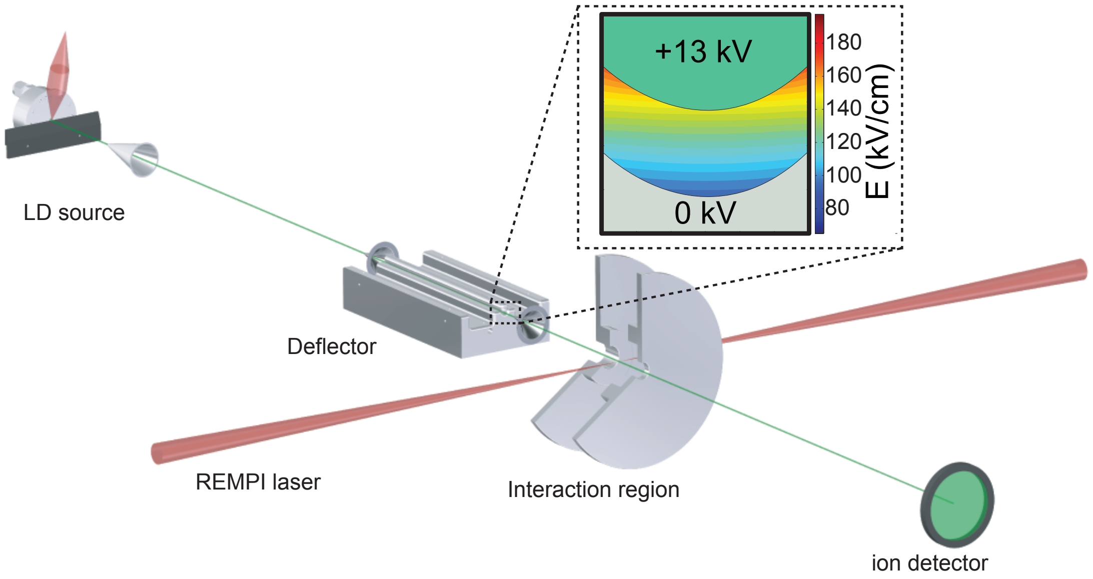

Figure 3.9: Sketch of the complete experimental molecular beam setup. Shown inset is a cross-section of the electrostatic deflector showing typical field strengths inside.

the ionised species.

The electrostatic deflector consists of two electrodes commonly referred to as trough and rod, between them is a 1.4 mm channel for the molecular beam to pass through. A voltage up to 15 kV is applied to the rod while the trough is at ground potential. The resulting strong inhomogeneous static electric field is illustrated in Figure 3.9 [13]. The molecular beam travels through this electric field and the trajectories of molecules are influenced in dependence of their effective dipole moment-to-mass ratio [29].

To record deflection profiles of the molecular beam, the ionisation laser is scanned in x-direction and at each position a time-of-flight mass spectrum is recorded. From these measurements the relative molecular beam density in the x-direction is obtained for all ions in the mass spectrum.

3.4 Sample Preparation

Here, we detail the sample preparation of fresh solid samples onto the sample bar. Therefore, old sample needs to be removed, the surface needs to be roughened and new sample needs to be rubbed on. For the roughening of the surface the tool shown in Figure 3.10 was used, to ensure the sample bar has the same height across its entire length of 80 mm. Additionally, all sample bars prepared with the same settings of the tool have identical height. This means that the height of the sample bar does not need to be realigned upon change.

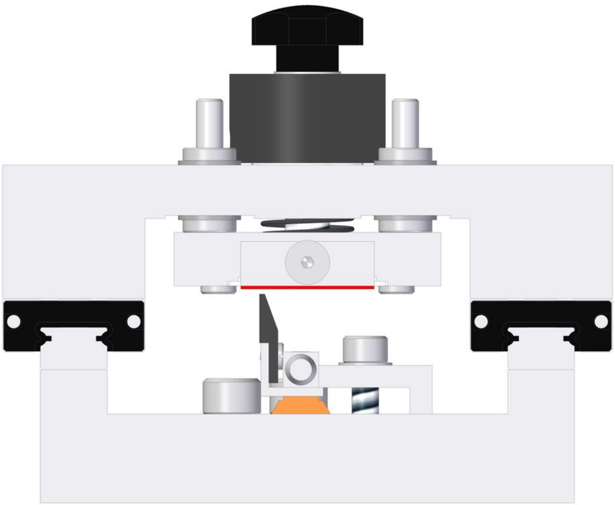

Figure 3.10: Cross-section of the sample bar grinding tool. The sand paper is emphasized in red. Right and left are rails so that the sand paper can easily be moved back and forth along the 80 mm of the sample bar. With the big black adjustment screw on top the height of the sand paper can be adjusted.

Afterwards the molecular sample needs to be prepared and rubbed on the sample bar, as shown in Figure 3.11. The molecular sample was mixed with graphite powder with the concentration of $\sim$ 1:1 graphite : sample by volume, the mixture was ground in a mortar, placed on a weighing paper along a line, and the sample bar was pressed and rubbed with gentle force into the mixture, until a thin layer of sample sticks to the sample bar, as shown in Figure 3.12.

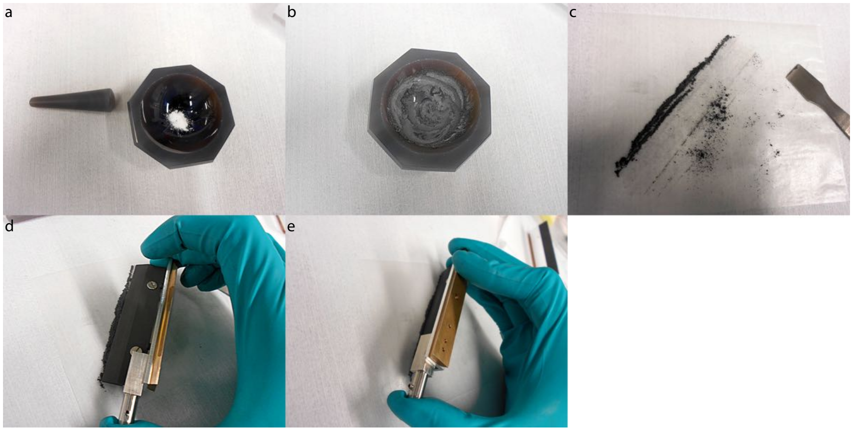

Figure 3.11: Preparation of a sample bar. First, the sample and graphite were taken in the same amount by volume and placed in the mortar (a), afterwards sample was mixed and ground together (b), then the mixture was placed in a line on a weighing paper (c), finally the sample bar was turned up side down and rubbed into the sample (d,e) until the sample stuck in an even and thin layer on the sample bar.

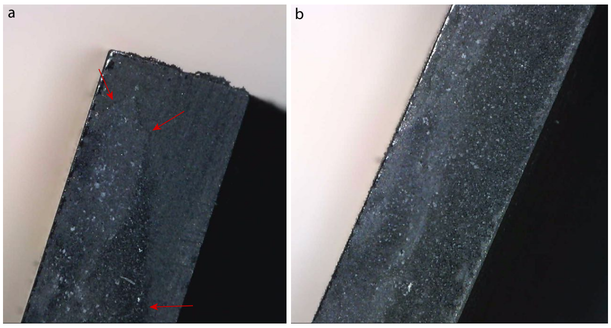

Figure 3.12: A microscope image of the thin sample layer on the sample bar. On picture (a) not the entire sample bar is covered with sample. The edge of the sample is marked with red arrows.

A thin and even sample layer is important for signal stability from the laser desorption source. A thick sample layer tends to stick better to itself than to the sample bar. This leads to large pieces of sample dropping off during laser desorption measurements. Additionally, experience showed that more graphite in the mixture made the sample stick better, as did a finer ground sample.

4 Characterising and Optimising a Laser-Desorption Molecular Beam Source[1]

4.1 Introduction

Laser desorption (LD) is a widely used technique to vaporise non-volatile organic molecules for gas-phase studies. The concept of laser desorption is a rapid heating of the sample to be vaporised, at around 10^{10}–10^{12} K/s, such that a fraction of molecules desorb intact instead of fragmenting [17, 21]. Later studies combined laser desorption with pulsed molecular beams to directly cool the desorbed molecules, enabling the investigation of intact neutral molecules in the gas-phase at low vibrational temperatures [22–25]. The main advantage of laser desorption over other vaporisation techniques, such as thermal vaporisation, is the ability to introduce intact thermally labile organic molecules, including peptides and proteins, into a cold molecular beam. This has been demonstrated, e. g., for a pentapeptide (Ser-Ile-Val-Ser-Phe-NH_2) [27] or the delta sleep inducing nonapeptide [26].

A first detailed characterisation of a laser desorption source coupled to a molecular beam

---

[1] This chapter is based on the publication *Characterizing and optimizing a laser desorption molecular beam source*, N. Teschmit, K. Długołęcki, D. Gusa, I. Rubinsky, D. A. Horke, J. Küpper, *Journal of Chemical Physics* **147**, 144204 (2017)

I was conducting the experiments, the data analysis and wrote the paper under the supervision of D. Horke and J. Küpper.

(MB) valve was conducted nearly 30 years ago. Using anthracene, diphenylamine, and perylene, combined with resonance-enhanced multi-photon ionisation (REMPI) spectroscopy, approximate vibrational temperatures of <15 K and rotational temperatures of 5–10 K were determined [23]. This demonstrated the ability of laser desorbed molecular beams to gently vaporise large, thermally labile molecules and to efficiently cool them. Since then various spectroscopic techniques have been combined with laser desorption molecular beam sources and recent experiments have included resonance-enhanced multi-photon ionisation studies [24], (far) infrared (IR)-ultraviolet (UV) double resonance techniques [28], IR multi-photon dissociation [69], and zero-kinetic-energy-photoelectron (ZEKE) spectroscopy [70].

In recent years, x-ray free-electron lasers (XFELs) have emerged as powerful tools for structure determination of gas-phase systems, with the potential to achieve atomic-resolution structures with femtosecond temporal resolution, recording so-called *molecular movies* [2]. The ultrashort pulse duration available at XFELs enables the recording of a diffraction pattern from a molecule prior to destruction by the high intensity of the x-ray pulses [4]. This *diffraction-before-destruction* paradigm, albeit still discussed [7, 8, 71], has recently also been demonstrated for isolated gas-phase molecules [6, 60, 72]. Similar to the time-resolved nuclear dynamics that can be recorded at XFEL sources, modern laboratory based attosecond light sources allow the measurement of real-time electron dynamics in isolated molecules [73].

These experiments, however, are themselves inherently not species specific, i. e., all molecules within the interaction region will be probed. Therefore, combination of laser desorption with XFEL and attosecond experiments requires a pure molecular sample in the gas-phase. Furthermore, to be compatible with central facility light sources, the laser desorption source needs to be translatable in three axes to adjust the molecular beam to the fixed XFEL beam. Additionally, the continuous measurement time should be as long as possible and the sample quickly exchangeable.

Here, we detail the characterisation, and optimisation of our novel laser desorption molecular beam source design, constructed to be compatible with central facilities, such as XFELs or attoscience centers. Using the dipeptide Ac-Phe-Cys-NH_2 as a prototypical labile biological molecule, which has first been laser desorbed and studied by the Rijs group [62, 74], we characterise the created beam using strong-field ionisation with a femtosecond laser pulse. This allows us to monitor all species present in the interaction region, including the carrier gas of the supersonic expansion. We show the optimisation of experimental parameters to reduce fragmentation, to improve cooling of desorbed molecules and, thereby, to maximise the phase-space density of intact parent molecules in the interaction region. The created molecular beams are well-suited to further manipulation and purification, e. g., using electrostatic deflection techniques [29], an important step towards recording temporally and spatially resolved nuclear and electronic dynamics of isolated biomolecules.

4.2 Experimental Setup

The mechanical design and construction of this laser desorption source is based on compatibility with large-scale-facility-based photon sources. The laser desorption source consists of a single central mechanical unit containing all necessary parts (molecular beam valve, sample bar with motors, and desorption laser optics). It is mounted on a three axis manipulator on a single flange for independent motion in the source chamber, which is pumped with a turbo molecular pump (Pfeiffer Vacuum HiPace 700P) to operating pressures typically around 10^{-5} mbar. It contains a cantilever piezo valve [64] operated at 6 bar backing pressure of argon. The valve has a 300 µm orifice, followed by a conical opening of 4 mm length and 40° opening angle. Conical nozzle shapes are well known to produce molecular beams with more efficient translational cooling and greater directionality, and hence densities, than simple pinhole sources [61]. A graphite (Poco EDM-1) sample bar (80 mm long, sample channel width 1.2 mm) is placed approximately 200 µm in front of the valve, see Figure 5.2. The sample bar height (y axis) can be translated using an in-vacuum two-phase stepper motor (Owis SM.255.V6). To replenish the molecular sample, the sample bar can be moved along the x-direction using an in-vacuum linear piezo-stage (SmarAct SLC-24120-S-HV), typically operated at 0.02 mm/s. This results in measurement times of around 70 min per sample bar. For longer measurement periods the sample bar can be quickly exchanged with a load-lock system, pumped by a Pfeiffer Vacuum HiCube

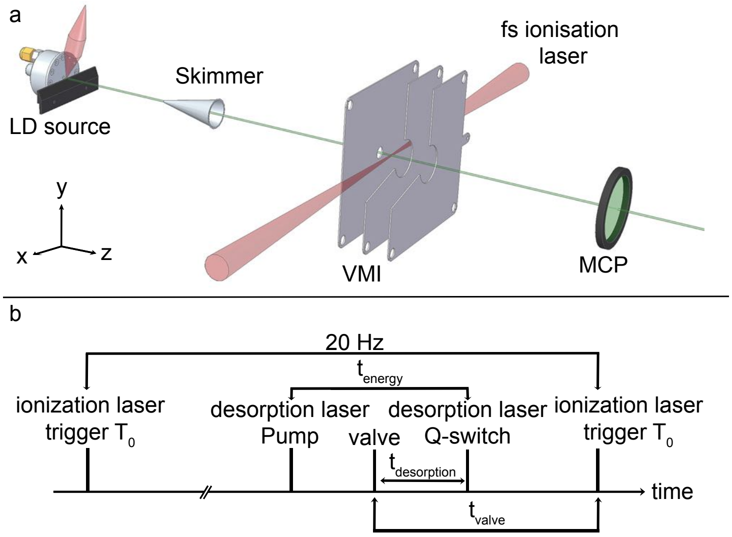
a
fs ionisation laser
Skimmer
LD source
y
x
z
VMI
MCP
b
20 Hz
t_{energy}
ionization laser trigger T_0
desorption laser Pump
valve
desorption laser Q-switch
ionization laser trigger T_0
$t_{desorption}$
time
t_{valve}

Figure 4.1: (a) Experimental setup for characterising a laser desorption source. The source chamber contains the laser desorption source and and is separated from the detection chamber by a 2 mm conical skimmer. The detection chamber houses a velocity-map imaging setup and micro-channel plate detector. (b) Experimental timing diagram. The master trigger is given by the ionisation laser, a kHz-repetition-rate femtosecond-pulse laser system that cannot trivially be externally triggered, and the molecular beam valve is triggered relative to this with delay t_{valve}. The desorption laser trigger is defined relative to the valve with delay $t_{\text{desorption}}$, while the energy of the desorption laser can be changed by modifying the Q-switch timing t_{energy}.

80 Eco pumpstand (typical turn-around time 10 minutes). The entire molecule source (valve, sample-bar holder with motors, and desorption-laser optics) is placed on a three axis manipulator and can furthermore be adjusted for tip and tilt angle, allowing independent five-axes motion of the device within the vacuum chamber, as required for experiments at XFEL facilities. It is generally useful for operation of the source in molecular-beam setups were accurate alignment of the source is crucial, e. g., multi-skimmer setups or electrostatic manipulation devices [29, 75].

Molecules on the sample bar are desorbed by pulses from a fiber-coupled, diode-pumped Nd:YAG laser at 1064 nm (Innolas Spitlight Compact DPSS10), operating at 20 Hz with a pulse duration (full width at half maximum) of 9 ns and pulse energy up to 0.8 mJ. This is coupled into a multimode fiber (CeramOptec WF 400/440P) with core diameter 400 µm and numerical aperture of 0.22. The fiber is coupled into the vacuum chamber with a custom-made Swagelock connection and polytetrafluoroethylene (PTFE) plug [66]. Inside the chamber the fiber is out-coupled with a custom made vacuum compatible fiber collimator and the laser beam is focused to a spot size of approximately 0.6 mm on the sample bar. Custom mounting of the collimator allows variation of the laser spot size on the sample, as well as translation of the laser beam along the x and z axes, and tilting in the yz plane.

Following desorption, molecules are picked up by the supersonic argon jet from the valve and rapidly cooled down. The resulting molecular beam is skimmed with a 2 mm diameter skimmer (Beam Dynamics Inc. Model 50.8), located approximately 5 cm downstream the valve. Following the skimmer the molecular beam enters the differentially pumped (Pfeiffer Vacuum HiPace 2300) detection chamber, maintained at pressures around 3×10^{-7} mbar. The detection chamber contains a velocity-map imaging (VMI) setup with a classic Eppink and Parker 3-plate design [68]. The distance from the molecular beam valve to the interaction point is around 45 cm. For the results presented here, the VMI setup was operated as a time-of-flight mass spectrometer, with typical mass resolution $m/\Delta m \approx 100$.

The molecular beam is probed *via* strong-field ionisation using a femtosecond Ti:Sapphire laser system (Spectra Physics Spitfire Ace) with a central wavelength of 800 nm, a pulse duration of 40 fs and pulse energies up to 300 µJ. It is focused into the vacuum chamber with a $f = 800$ mm lens to a spotsize (FWHM) of 80 µm in the interaction region between the VMI electrodes.

The timing scheme for our experimental setup is shown in Figure 5.2. The femtosecond ionisation laser is used as the master trigger in the experiment. Its native repetition rate of 1 kHz is electronically reduced to provide a trigger signal at 20 Hz. The molecular beam valve trigger is defined, relative to this fs-laser trigger, by the delay t_{valve}. This delay defines which (longitudinal) part of the molecular beam we are probing with the ionisation laser. The desorption laser is now triggered relative to the valve trigger and

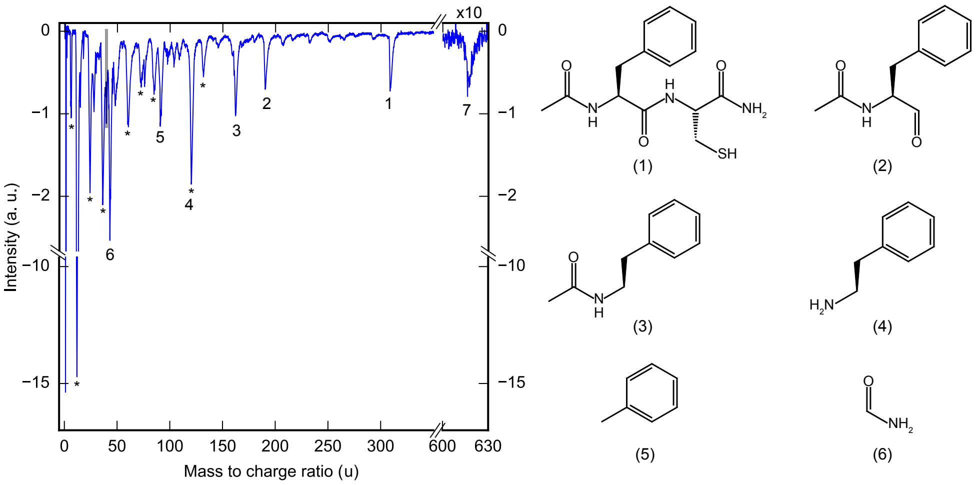

Figure 4.2: Time-of-flight mass spectrum of laser desorbed Ac-Phe-Cys-NH$_2$ following strong-field ionisation. Peaks resulting from carbon or carbon clusters are labeled with $*$. 1 corresponds to the parent ion, and 2–6 to molecular fragments. A small signal from Ac-Phe-Cys-NH$_2$ dimer is also observed, 7. Grey shading marks the peak from argon carrier gas, which appears much smaller than molecular fragments due to the much higher ionisation potential.

defined by the delay $t_{\text{desorption}}$, which controls where within the gas pulse the desorbed molecules are placed. This setup enables us to change t_{valve} without changing $t_{\text{desorption}}$. We note that the timing values given should be seen as relative, not absolute values, as they are susceptible to electronic delays within the valve and laser controls used.

The velocity of the molecular beam is measured by recording the temporal profile of the beam, i. e., scanning t_{valve}, for different longitudinal positions of the valve, i. e., its distance from the first skimmer. We then evaluate the beam velocity from the temporal shift in the peak of the parent ion for different valve positions to be approximately 670 m/s.

The dipeptide Ac-Phe-Cys-NH$_2$ (95% purity, antibodies-online GmbH) is used in this study without further purification. The sample powder is mixed with graphite powder (0.44:1 by weight) and ground with pestle and mortar to a fine powder. The top surface of the graphite sample bar is roughened with sand paper and pushed into the prepared sample mixture. Gentle force is used to ensure the mixture sticks to the sample bar and an even sample layer is formed.

4.3 Results and Discussion

4.3.1 Molecular fragmentation

A measured time-of-flight mass spectrum of laser desorbed and strong-field ionized Ac-Phe-Cys-NH_2 is shown in Figure 4.2. It shows clear signals from parent ions (1 in Figure 4.2), fragment ions (2–6) and parent dimer (7). Furthermore, we observe several peaks from carbon and carbon clusters consisting of up to 11 atoms (highlighted with an asterisk in Figure 4.2). These are present due to their direct desorption from the graphite matrix material within which the sample is embedded, as well as due to the formation of higher-order carbon clusters within the desorption plasma created by the laser pulse [76]. The molecular fragments originating from the Ac-Phe-Cys-NH_2 sample identified in the spectrum are shown in Figure 4.2. Strong-field ionisation is a non-species-selective method and thus allows the identification of all species present within the molecular beam. This approach, therefore, allows us to optimize the yield and fraction of intact parent molecules contained within the molecular beam. For further analysis of the contributing parameters for laser desorption, we identify four characteristic fragments; the Ac-Phe-Cys-NH_2 parent ion ($m/z = 309$, peak labeled 1), the $C_{10}H_{12}NO$ fragment ion ($m/z = 162$, 3), the argon ion peak ($m/z = 40$), and the carbon peak ($m/z = 12$). The particular molecular fragment (3) is chosen as it provides the largest-intensity clean signal, i. e., it does not overlap with a carbon cluster fragment.

In order to evaluate the effect of the femtosecond ionisation laser on the observed molecular fragmentation, we scan the laser pulse energy between 60 µJ and 220 µJ. The observed integrated ion intensities for the 4 characteristic peaks are shown in Figure 4.3 b. The solid lines are a power-law fit of the form $A \times x^n + c$. Additionally, in panel (a) we plot the ratio of observed parent ions to the selected fragment ions for the probed intensity region. This nearly constant ratio indicates that the strong-field ionisation process has little influence on the fragmentation of the parent ion. This is in agreement with previous studies that indicated that the fragmentation of complex molecules in intense laser fields is very sensitive to the laser pulse duration, but not the total energy of the pulse [77].

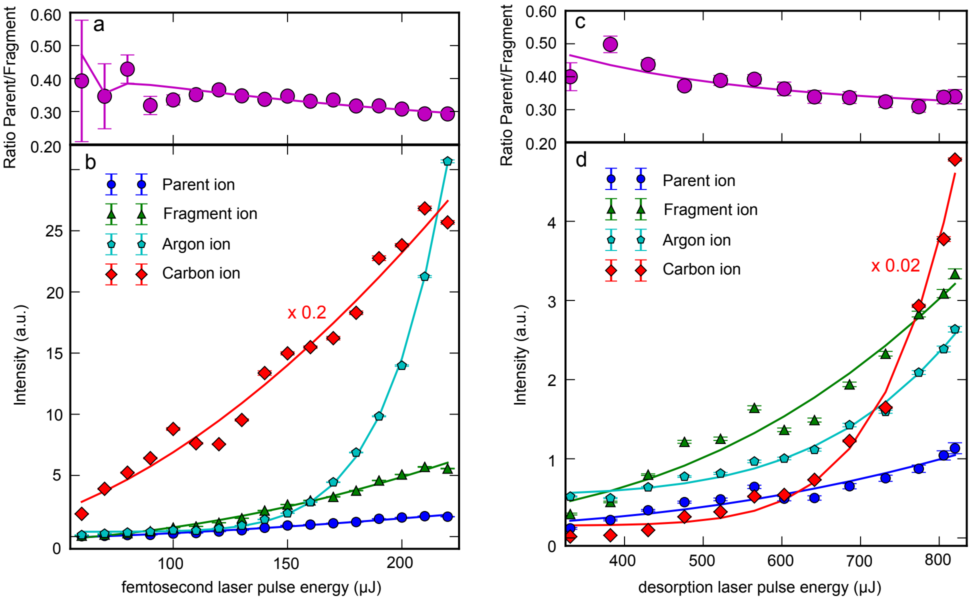

Figure 4.3: Measured ion intensity for parent Ac-Phe-Cys-NH_2, the characteristic fragment at $m/z = 162$, carbon and argon as a function of ionisation laser pulse energy (a,b) and desorption laser pulse energy (c,d). Solid lines are power law fits to the data. The top panels (a,c) show the ratio of parent to fragment ions observed. Throughout the manuscripts, shown error bars correspond to 1 standard error (std. err.).

Therefore, increasing the ionisation laser intensities leads to larger ion signals, but has little effect on the fragmentation patterns observed. Hence using strong-field ionisation with ultrashort laser pulses is a powerful tool for the full characterisation of molecular beams containing complex molecules and fragments thereof.

To elucidate the effect of the high-power desorption laser on the molecular sample on the graphite sample bar, we record mass spectra for various desorption laser energies in the range ∼ 350–800 µJ. In Figure 4.3 d, we plot the recorded integrated ion intensities for the four characteristic masses as a function of desorption laser energy, with solid lines corresponding to a power law fit to the data. As can be seen from these data, all intensities increase with increasing laser energy. This includes, somewhat un-intuitively, the argon seed gas signal observed in the interaction region, which will be discussed later on. The carbon signal shows the steepest dependence on desorption laser pulse energy, which is consistent with the formation of isolated carbon atoms and clusters within a laser-induced plasma [76]. Figure 4.3 c shows the ratio of parent to fragment signal. A decrease in the parent-to-fragment ratio is observed as the desorption energy is increased. Thus the desorption process can cause fragmentation of the sample and the highest fraction of parent ion within the molecular beam is obtained at the lowest desorption energies, albeit at the expense of density within the beam. We furthermore note that the actual fractional yield of parent ions within the molecular beam is significantly smaller than the numerical values shown in Figure 4.3, since these only take into account a single characteristic fragment. Additionally, any charged fragments produced during the desorption process will not arrive in the detection region due to the static fields applied to the time-of-flight electrodes. All studies below were conducted with around 670 µJ desorption laser pulse energy and 140 µJ ionisation laser power.

4.3.2 Molecular beam properties

To probe the longitudinal (or temporal) profile of the produced molecular beam, we scan the timing between the valve trigger and the ionisation laser, t_{valve}, see Figure 5.2, probing different portions of the molecular beam. A typical temporal profile is shown in Figure 4.4 a for the pure argon beam emerging from the valve with (purple) and without (blue) the graphite sample bar in place. Without the sample bar, we observe a single sharp peak with a full width at half maximum of $\sim$ 75 µs (corresponding to a speed ratio of $\sim$10), and a small shoulder at longer times due to the rebounce of the piezo within the valve [64]. When the sample bar is placed in front of the valve, as shown in the picture inset in Figure 4.4, the argon gas flow is significantly disturbed. The overall gas-pulse is significantly broader, the main peak intensity is decreased by a factor of $\sim$3, and more intensity is observed at later times. We attribute these observations to the disturbance of the argon flow by the sample bar and possible turbulences in the flow-field within the dead volume behind the sample bar.

By changing the relative timing of the desorption laser and valve trigger ($t_{\text{desorption}}$ in Figure 5.2), we can now place the plume of desorbed molecules at different positions within

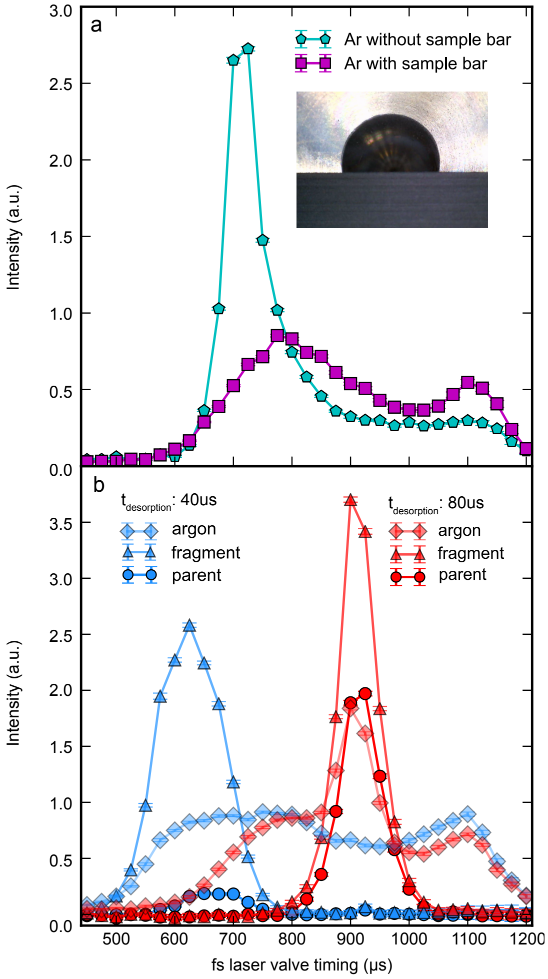

Figure 4.4: Integrated ion intensity as a function of valve delay t_{valve}, i. e., temporal (longitudinal) profiles of the molecular beam. (a) argon profile with (purple squares) and without (torquois pentagons) sample bar in front of the valve. The inset shows a photograph of the sample bar in front of the valve at the optimized position; see text for details. (b) Temporal profile for APCN parent, characteristic fragment and argon for two different desorption laser delays, $t_{\text{desorption}}$.

the argon beam. Changing this relative timing has significant effects on the observed intensities of argon, parent, and fragment ions alike, as shown in Figure 4.4 b. We show temporal molecular beam profiles for argon (diamond markers), fragment 3 (triangles), and parent ions (circles) at two different time delays $t_{\text{desorption}}$. The relative timing of the desorption laser and molecular beam valve significantly affects the intensity of fragment and parent ions, and the ratio between the two. We attribute this effect to changes in the cooling efficiency as the hot desorbed molecules are placed within the argon expansion at different times. An efficient cooling process is required to quench the excess energy of the desorbed molecules and prevent further fragmentation. Comparing the relative integrated intensities of parent and fragment signals at the two timings shown in Figure 4.4 b, we observe that the combined intensity is approximately identical at the two time points, however the ratio between the two differs significantly. This suggests that while approximately the same density of molecules, including fragments, is present within the initially desorbed plume, the less efficient cooling in the less-dense front of the gas pulse at the delay of 40 µs leads to significant fragmentation occurring before or during the argon gas pulse, i. e., the cooling occurs too late and fragmentation has already taken place.

Further to its influence on the molecular signals the timing of the desorption laser clearly has an effect on the observed argon signal. An increase in argon signal is observed at the timing where desorbed molecules (parent or fragments) are present within the beam. We suspect the observed increase in the argon signal is not due to more argon arriving at the detector, but due to signals of molecular fragments or carbon clusters overlapping with the argon mass at 40 u in a very crowded spectrum shown in Figure 4.2.

The dependence of the observed fragmentation on the relative position in the gas pulse is, furthermore, evident when comparing mass spectra recorded at different $t_{\text{desorption}}$, as shown in Figure 4.5. These spectra have been recorded with t_{valve} optimized for parent ion signal and are plotted normalized with respect to the observed parent intensity. This shows that all molecular fragments are significantly more abundant at $t_{\text{desorption}} = 40$ µs, indicating a much higher internal temperature of the desorbed molecules, due to the less efficient cooling, and correspondingly increased fragmentation.

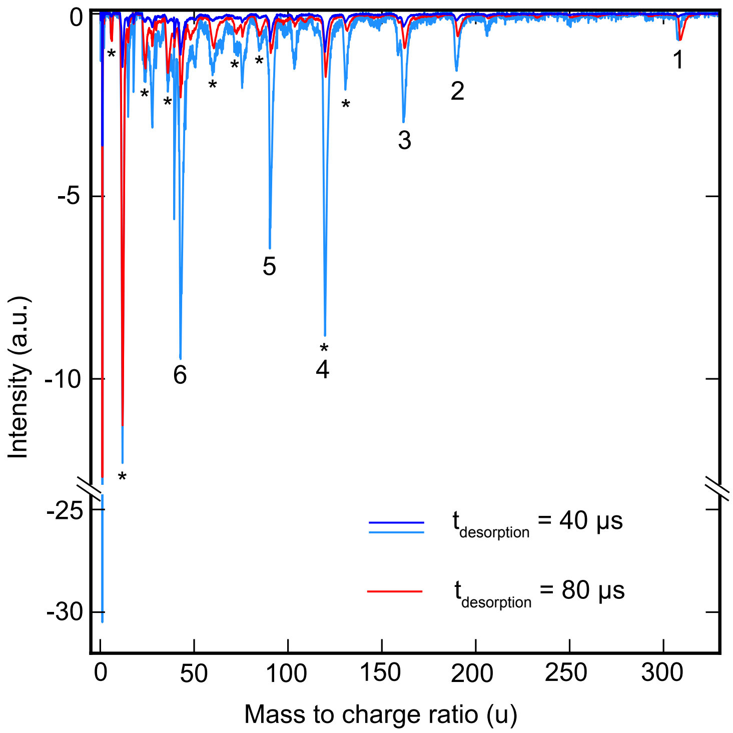

Figure 4.5: Mass spectrum for the two different desorption laser timings shown in Figure 4.4 b, red and dark blue are the absolute intensities measured, the light blue trace has been scaled to the parent ion intensity of the red ($t_{\text{desorption}} = 80$ µs) trace. A significant increase in fragment ion yield is observed for $t_{\text{desorption}} = 40$ µs.

To identify the optimum placement of the desorbed plume within the gas pulse, we have repeated these measurements for several delay points, shown in Figure 4.6, where the curve with higher intensity always corresponds to the fragment and the curve with lower intensity to the parent ion. For better comparison the parent intensity for each $t_{desorption}$, as well as the ratio of parent to the characteristic fragment, is shown in Figure 4.7.

For our setup and under the given experimental conditions, we identify a delay of 80 µs as providing the highest total intensity of parent signal, as well as the best parent-fragment ratio. This ratio is very sensitive to the relative timings, and changes of 10 µs can change this ratio by a factor of ∼2. This is due to the gas pulse directly after the valve being significantly shorter (opening time of the piezo is around 25 µs) than in the detection region located ∼0.5 m downstream where the measurements were taken. This is also

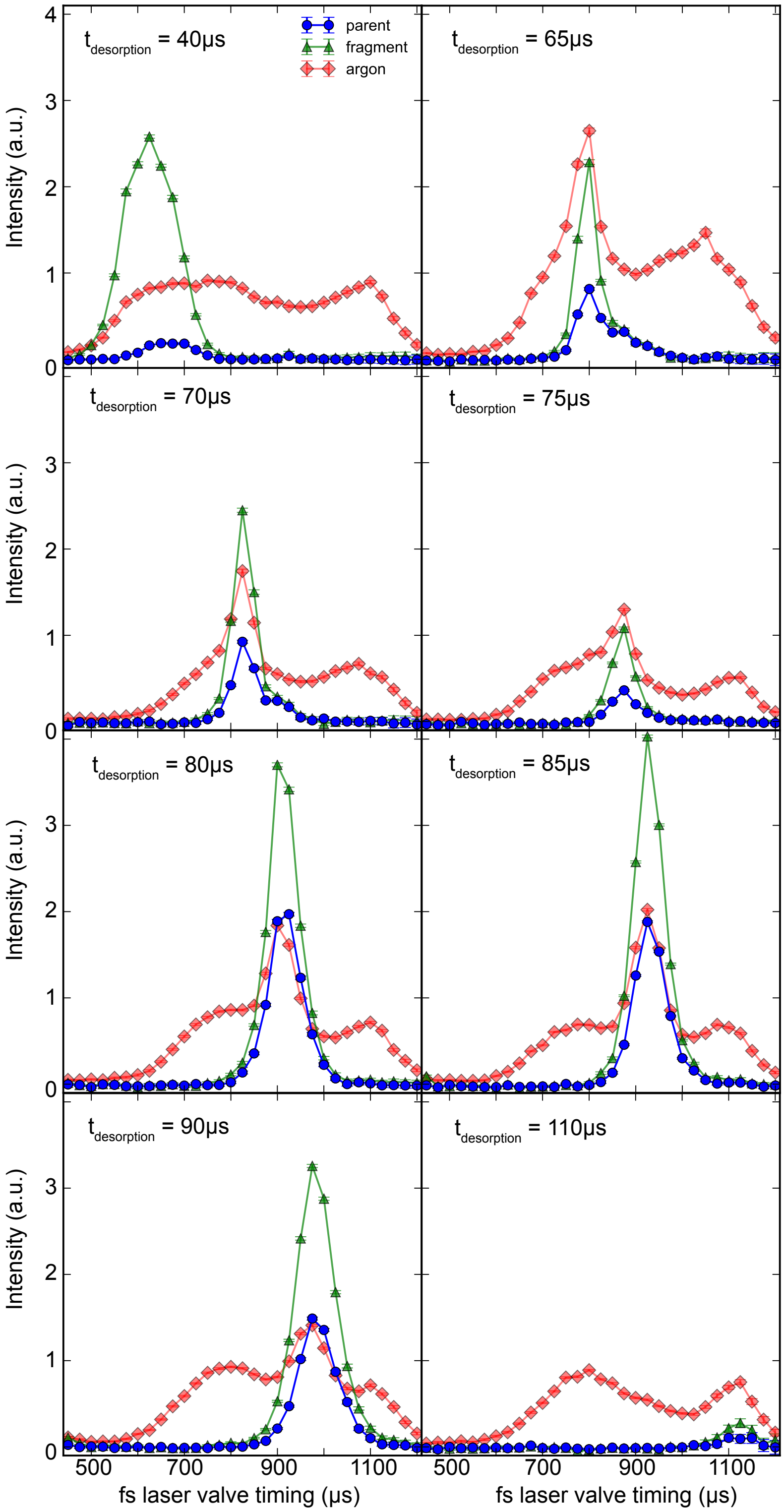

Figure 4.6: Longitudinal (temporal) profiles of the molecular beam for different $t_{\mathrm{desorption}}$ delays. Shown are intensities for the intact parent (blue circles), fragment (green triangles) and argon (red squares) ions.

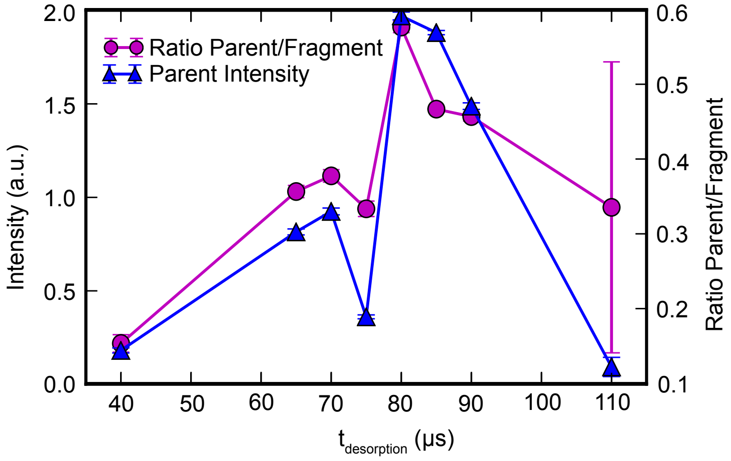

Figure 4.7: Dependence of the parent ion intensity and the parent to fragment ratio on the desorption laser timing $t_{\text{desorption}}$; error bars correspond to 1 standard error. Optimum conditions are observed for $t_{\text{desorption}} = 80$ µs. The data at 75 µs shows a significantly lower intensity than expected, which could be due to irregularities in sample bar preparation; see text for details.

reflected by the steep falloff of signal for later desorption laser timings.

As shown above, the sample bar has a large effect on the supersonic expansion and hence the produced molecular beam. To investigate this further we have taken data for different heights of the sample bar, shown in Figure 4.8. Here, we recorded the intensity of argon, carbon, fragment and parent ions for different heights of the sample bar, as well as the ratio of detected parent to fragment ions. We note that all this data was taken at identical timing of $t_{\text{valve}} = -900$ µs and $t_{\text{desorption}} = 80$ µs and that the height of the sample bar does change the desorption laser focusing conditions (since the focusing lens is fixed relative to the valve).

It is evident from this data that the sample bar height changes not only the peak intensity, but also the parent to fragment ratio, as shown in Figure 4.8 a. The observed intensities are very sensitive to the height of the sample bar, with parent, fragment and carbon ions showing maxima at different positions. This sensitivity was used in all previous measurements to fix the height for each new sample bar measured; it was optimized prior to taking data to obtain maximum signal from the parent ion. However, we note that due

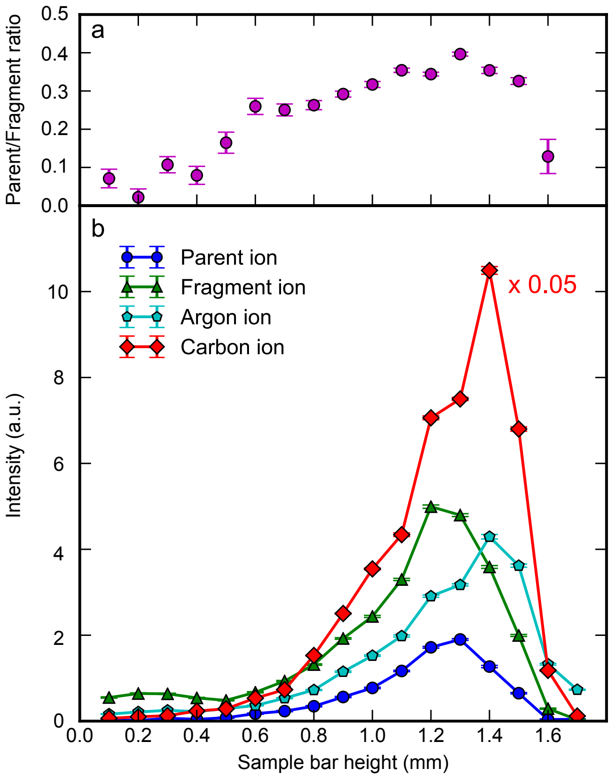

Figure 4.8: Measured ion intensity for parent APCN, the characteristic fragment at $m/z = 162$, carbon and argon as a function of sample bar height. The top panel shows the ratio of parent to fragment ions observed.

to the preparation method, slight differences in height can persists even across a single sample bar[2], and affect the measurement and especially the comparability between data sets. This could be the reason for the large deviation of the data shown for 75 µs in Figure 4.7. This sensitivity can be explained by a number of contributing factors; (i) the efficiency with which desorbed molecules are picked up and carried by the argon beam. Assuming that the slight differences in mass and size between parent and fragments are negligible given the very large number of collisions with the carrier gas, this should be comparable for all species within the beam, i. e., a lower pressure of argon should affect all species to a comparable extent. (ii) The degree to which the argon expansion is disturbed by the presence of the sample bar. In Figure 4.4 a we have shown that the sample bar influences the molecular beam speed and distribution; at the fixed t_{valve} conditions used here this will change the observed intensities. It has furthermore been shown already that the sample bar changes the directionality of the molecular beam [78]. (iii) Changes in the cooling efficiency of desorbed species lead to differences in the parent to fragment ratio in the beam. (iv) The spotsize of the desorption laser on the sample bar changes with different sample bar heights and thus the intensity of the laser and the number of molecules interacting with the laser is influenced. From the collected data we cannot comment on the relative importance of these different mechanisms, however, since (i) and (ii) should influence the parent and fragment molecules nearly identically, the observed changes in the parent to fragment ratio indicate a dependence of the cooling efficiency on the sample-bar height. The cooling efficiency should be best within the densest part of the molecular beam, which is on the axis of the 300 µm nozzle orifice. Therefore, a sample bar height just below this position, i. e., covering slightly less than half the nozzle opening, should lead to the densest plume of desorbed molecules being entrained in the densest part of the molecular beam. This simple consideration is consistent with our observations of the maximum parent signal and parent to fragment ratio occurring at the position labeled 1.3 mm. While we cannot disentangle all the different effects of changing the sample bar height, it is clear that this, and the associated influence on the supersonic expansion and molecular beam properties, is a crucial parameter for laser desorption entrainment of molecules into supersonic expansions. This could be further investigated by either measuring the gas flow from the nozzle directly, for example through direct visualization of gas densities [61, 79] or by measuring spatial argon profiles through strong-field ionisation mass-spectrometry at various distances from the nozzle.

---

[2] The sample preparation tool explained in section 3.4 has been designed after these measurements were taken and clarified the importance of a more careful sample bar preparation method.

Despite the wide use of laser desorption sources, very few studies have looked into the fundamental underlying processes. Furthermore, the vastly different source designs in use, e. g., different desorption laser wavelengths, intensities, pulse durations, different models of supersonic valves, etc., make comparison to previous studies difficult. While we believe this is the first study of laser desorption using strong-field ionisation, previous experiments have utilized electron impact ionisation and have similarly observed a large amount of neutral fragments produced by the desorption processes [17]. Our finding that the molecular packet of desorbed molecules is much shorter than the envelope of the seeding-gas pulse is also consistent with previous measurements [78]. Lastly, we point out that the use of a fiber-coupled desorption laser has been demonstrated before [80], albeit without refocusing inside the vacuum chamber that we have introduced here for greater control.

4.4 Conclusion

We have presented a novel laser desorption setup designed for use in advanced imaging experiments of ultrafast molecular dynamics and we have carefully characterised and optimised the laser desorption and molecular-beam-entrainment conditions. The setup consists of a single central mechanical unit containing all necessary parts (molecular beam valve, sample bar with motors and desorption laser optics) that is mounted on an *XYZ* manipulator on a single flange for independent motion. Furthermore, we have presented a detailed characterisation of our new laser-desorption source as well as molecular beams produced using laser desorption in general. By utilizing strong-field ionisation, we were able to probe all species contained within the beam. Under normal operating conditions we found that the molecular beam contains, in addition to parent molecules, significant amounts of molecular fragments, as well as carbon clusters from the desorption process. We investigated the role of the desorption laser fluence, the relative timing of valve opening and desorption laser, the sample bar height, and which part of the molecular packet is probed. While increased desorption laser fluence leads to more molecules contained within the molecular beam, it was found to induce fragmentation of the sample and leads to enhanced contamination of the beam with carbon and its clusters. The placement of the desorbed plume of molecules within the gas pulse from the supersonic expansion has a profound effect on the cooling efficiency, and thus the fragmentation observed. The best timing was found to be approximately in the center of the gas pulse, and is quite sensitive compared to the gas pulse duration in the detection region. The relative height of the sample bar in front of the valve orifice significantly affects the molecular beam expansion conditions, and hence the intensity of observed signals, as well as the parent to fragment ratio. However, finding the optimum position for the sample bar height is difficult, due to the number of competing effects taking place, and every sample bar being unique. Furthermore, parameters might be dependent on the employed molecular-beam nozzle, and our exact findings are specific to the used conical nozzle shape.

From our detailed investigation we found that the optimal settings for building a laser desorption source very much depend on the planned experimental scheme. While some parameters, such as the relative timing of desorption laser and the molecular beam valve, should always be optimized as shown here, other parameters are not critical. For example the pulse energy of the desorption laser should be chosen according to the application. For techniques that are only sensitive to intact parent molecule signal, like resonance-enhanced multi-photon ionisation, the pulse energy of the desorption laser should be kept high because this increases the number density of parent molecules in the interaction region. But for non-species-specific techniques, such as x-ray diffraction, the pulse energy should be reduced to minimise the contamination with fragments and carbon. However, even at the lowest desorption energy used here, we still observe a significant amount of molecular fragments and carbon clusters in the beam. While the former originate to some extent from the strong-field ionisation probing, the carbon and carbon clusters are certainly in the beam due to the desorption process. In order to produce a pure beam of intact parent molecules in the gas-phase, one can consider coupling a laser desorption source with other species separation techniques for neutral molecules, such as electrostatic deflection or alternating gradient focusing [12, 29].

5 Spatially separated conformers of the dipeptide Ac-Phe-Cys-NH_2[1]

5.1 Introduction

Proteins are the workhorses of biological functionality in living cells and are at the heart of, for instance, the transport of oxygen, the catalysis of biochemical reactions and interactions, or the reproduction of cells and replication of DNA. This wide-ranging functionality is enabled by the unique and specific 3-dimensional (3D) structures of these systems. While every protein is composed of a sequence of the 20 amino acids encoded in RNA, the exact sequence and resulting intra-molecular interactions lead to a specific and unique 3D structure, determining a proteins functionality. Changes in this 3D structure, such as misfolding, can dramatically alter protein function with potentially wide-ranging consequences, such as neurodegenerative diseases [81–83]. Especially the strong hydrogen bonding between amino acids within the sequence has a profound effect on the resulting protein structure [84–87]. In order to study the underlying intra-molecular and hydrogen-bonding interaction in detail, one often turns to studying isolated small peptide fragments in the gas-phase [25, 88–91]. However, even single amino acids and dipeptides often populate several conformational states [62, 87, 92–94], e. g., rotational structural isomers, complicating detailed analysis and the extrapolation from small model data to entire protein complexes. Mapping the structure-function relationship of these biomolecular machines thus requires reproducible samples in the gas-phase in well-defined initial states [95–98]. More generally, species- and conformer-pure samples of peptides in the gas-phase would open the door for novel non-species-specific experimental techniques, such as atomic-resolution diffractive imaging with x-rays [2, 4–6, 99] or electrons [41, 100], attosecond-electron-dynamics experiments [73], or kinetic studies of the chemical reactivity of a single conformer [96]. Such experiments inherently do not distinguish which conformer was probed, making it very difficult or even impossible to interpret data collected with more than one conformer present in the interaction volume.

---

[1] This chapter is based on the manuscript *Spatially separated conformers of a dipeptide*, N. Teschmit, D. A. Horke, J. Küpper, submitted to *Angew. Chem. Int. Ed.*

I was conducting the experiments, the data analysis and wrote the paper under the supervision of D. Horke and J. Küpper.

To investigate biomolecules in the gas-phase requires their vaporisation without fragmentation or ionisation. Laser desorption has been demonstrated as a technique to vaporise such thermally labile molecules [17, 21], and the combination with supersonic expansion allows for rapid cooling of the desorbed molecules [21, 23, 28, 101]. However, even in such cold molecular beams different conformers, which differ by rotations about single bonds, can coexist. In order to produce a pure beam containing only a single conformer, we combine laser desorption with electrostatic deflection [29]. This allows the spatial separation of molecular species based on their distinct interaction with the applied electric field. This so-called Stark effect is dependent on the quantum-state specific effective dipole moment and this technique has been demonstrated to spatially separate conformers of small aromatic molecules [12, 13], and for very small molecules it can even produce single-quantum-state samples [102–104]. Furthermore, due to the rotational-state-dependence of the Stark effect [29, 54, 105], deflection allows the creation of very cold ($T_{\text{rot}} < 100$ mK) molecular ensembles. This can significantly improve the degrees of laser alignment and mixed-field orientation of molecules in space [36] and thus enable ensemble-averaged single-molecule imaging [2, 10].

Here, we present the first combination of laser desorbed biomolecules with electrostatic deflection and demonstrate the spatial separation of the two main conformers of the dipeptide Ac-Phe-Cys-NH_2, shown in Figure 5.1 a. These two conformers differ in their

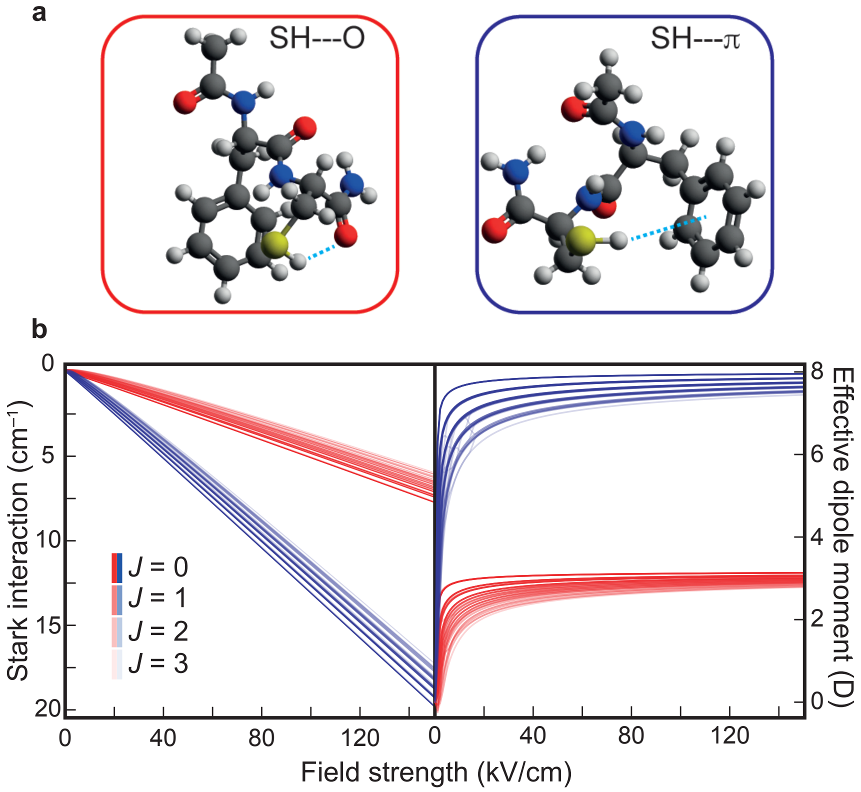

Figure 5.1: a: The two main conformers of the dipeptide Ac-Phe-Cys-NH_2 with their distinct hydrogen-bonding interactions of the cystine sidechain indicated. b: The Stark energy curves (left) and effective dipole moments (right) for the lowest rotational states of the two conformers.

hydrogen-bonding interactions and, hence, 3D structure. One conformer, indicated by red colour throughout this chapter, forms a hydrogen bond from the SH group to the oxygen on the carboxamide group, while the other conformer, blue colour, forms a hydrogen bond from the SH to the delocalised π-system. These two "beautiful molecules" [106] have been previously identified using vibrational and electronic spectroscopy [62]. [2] In a cold molecular beam these two conformers cannot interconvert, however, their significantly different dipole moments of 3.2 D and 8.1 D result in different Stark interactions, see Figure 5.1 b. This allows for their spatial separation with the electrostatic deflector if a sufficiently cold molecular ensemble can be created [29]. This would, furthermore, also separate the sample of interest from unwanted fragments or contaminants present in the beam, such as carbon clusters from the laser desorption process [101]. Compared to the separation of molecular ions in ion mobility measurements [107, 108], our method enables the separation of neutral species, avoiding space-charge density limitations that severely affect diffractive-imaging experiments [6, 41]. Furthermore, the low temperatures of the generated molecular ensembles allow for strongly fixing the molecules in space [36] — two prerequisites for the recording of atomically resolved molecular movies [2, 5].

---

[2] A third conformer was detected by the Mons group [74], but with a population so minor that it is not considered in our study.

5.2 Results and Discussion

Our implementation of the combination of laser desorption with electrostatic deflection is shown schematically in Figure 5.2; details are given in *Methods*. Briefly, the laser desorbed molecular beam enters a 15 cm long deflector sustaining electric field strengths on the order of 150 kV/cm^{-1}. The different conformers experience a different vertical deflection within this field, which originates from the Stark-effect interaction between the molecules' space-fixed dipole moment μ_{eff}, Figure 5.1 b, and the applied electric field ϵ. This leads to a force $\vec{F} = -\mu_{\text{eff}}(\epsilon) \cdot \vec{\nabla}\epsilon$ acting on the molecules [29, 54]. Thus, the observed deflection depends on the effective-dipole moment-to-mass ratio and the two conformers experience different forces, i. e., transverse accelerations, in the electric field, leading to their spatial separation. The molecular beam and the separation of conformers was characterised by recording spatial profiles of the beam. This was achieved by vertically translating the ionisation laser beam through the horizontal molecular beam, and recording the relative density as a function of laser height. The ionisation laser was tuned to specific resonances to selectively detect a single conformer.

Such spatial molecular beam profiles for the individual conformers in the absence of an electric field, i. e., with the deflector at 0 kV, are shown in Figure 5.3 a, to which all beam-profile intensities have been normalised. These show that both conformers are centered around $y = 0$ mm and exhibit the same spatial distribution. The measured width of the molecular beam is predominately defined by the apertures of skimmers and the

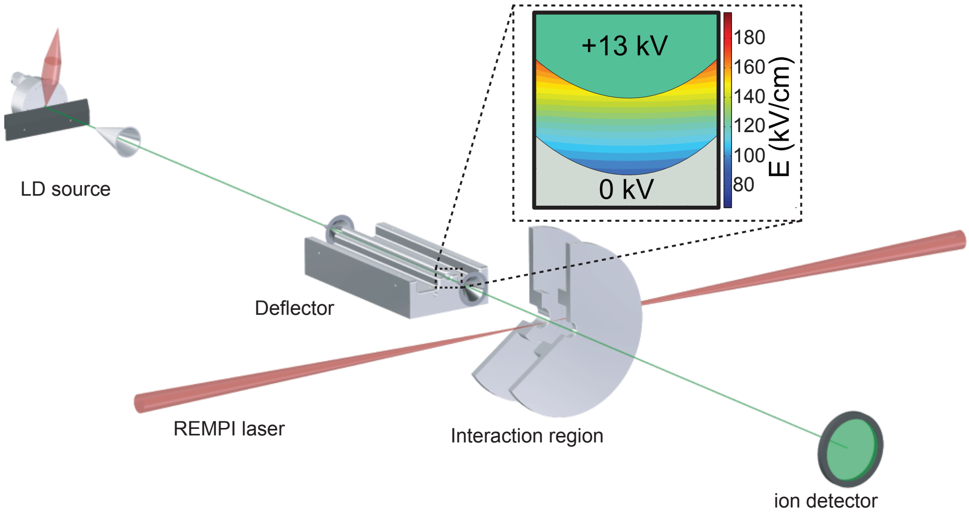

Figure 5.2: Schematic of the experimental setup combining the laser desorption with electrostatic deflection. The inset shows a cross-section of the deflector and the electric-field strength inside.

electrostatic deflector placed in the molecular beam, see *Methods*. The relative population of the two conformers in the beam was assessed by placing the ionisation laser focus at the center of the profile, as indicated by the black arrow in Figure 5.3 a, and scanning the ionisation wavelength across the electronic-origin transitions of the two conformers around 37325 cm^{-1} and 37450 cm^{-1}, respectively. The resulting resonance-enhanced multi-photon ionisation (REMPI) spectrum is shown in Figure 5.3 d and yielded an intensity ratio of $\sim 2:1$ for the SH–O and SH–π bound conformers, respectively. Assuming identical ionisation probabilities for the REMPI process, this ratio can be taken as a measure of the relative conformer populations in the molecular beam.

Charging of the electrostatic deflector lead to deflection of the molecular beam in the positive, upward direction, as shown in Figure 5.3 b,c. Application of 4 kV to the deflector, Figure 5.3 b, lead to a clear shift of both spatial profiles, with the more polar SH–π-bound conformer shifting significantly more. This created an area, between ∼1.7–2.5 mm, were a highly enriched sample of this conformer was obtained, as confirmed by the REMPI spectrum collected at position $y = 1.75$ mm and shown in Figure 5.3 e. To separate and create a pure sample of the SH–O-bound conformer, a voltage of 10 kV was applied,

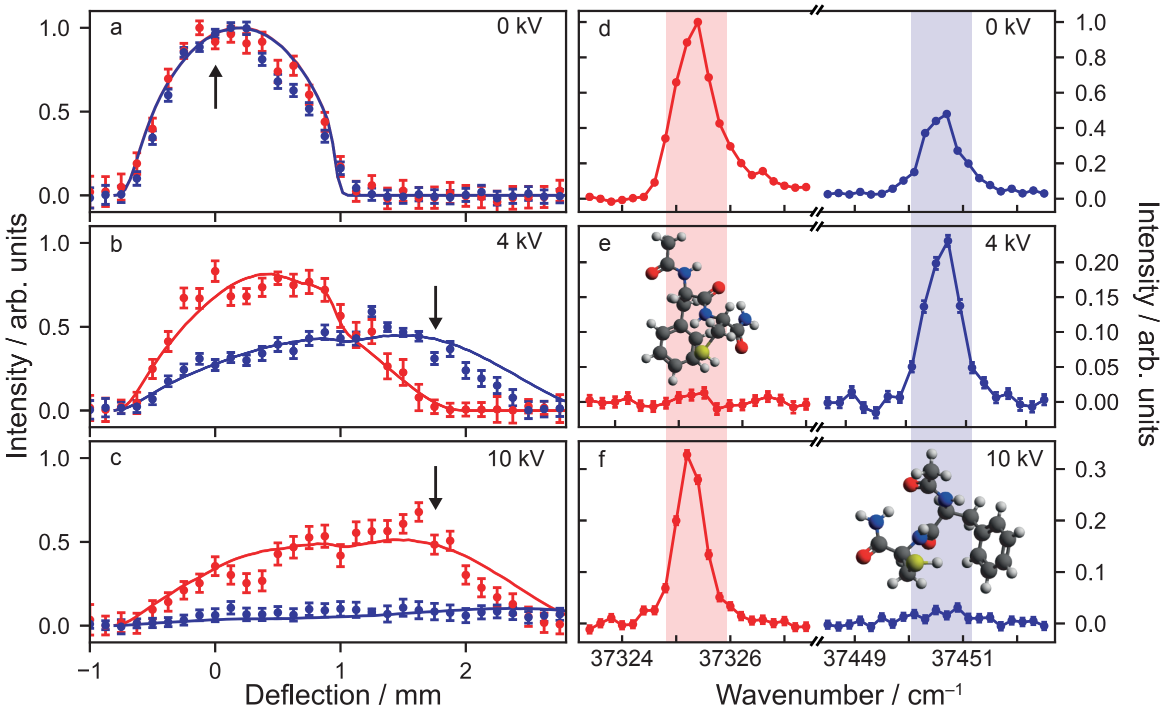

Figure 5.3: Spatial molecular beam profiles (a–c) and corresponding REMPI spectra (d–f) for the two main conformers of Ac-Phe-Cys-NH_2. These are collected at deflector voltages of 0 kV (a,d), 4 kV (b,e) and 10 kV (c,e). Solid lines in the deflection profile plots (a–c) are taken from quantum-state resolved trajectory simulations with a 2.3 K thermal state weighting. REMPI spectra are taken at the spatial position indicated by the black arrow in the spatial profiles.

leading to depletion of the SH–π-bound system from the interaction region, as shown in Figure 5.3 c. This is due to the large deflection experienced by this more polar conformer, such that these molecules collided with the deflector or following apertures and no clear beam was observable anymore. Instead, a position-independent small background signal was present. A REMPI spectrum recorded in the deflected beam is shown in Figure 5.3 f, confirming the highly-enriched sample of the SH—O-bound conformer created under these conditions.

Using a calibrated ion detector, we estimated the number of ions produced per laser shot to be ~1 for REMPI ionisation. By using more efficient strong-field ionisation

(SFI) we extracted a lower limit for the absolute number density of 10^7 cm^{-3}. For the density determination a time-of-flight mass spectrum using strong-field ionisation by femtosecond laser pulses (800 nm central wavelength, 40 fs duration, typical pulse energies of 100 µJ) is recorded [101]. In the time-of-flight mass spectrum all peaks originating from the Ac-Phe-Cys-NH_2 molecule are integrated and the total ion current on the detector determined. This is compared to the known calibrated current for a single ion hit, which leads to approximately 18 ions/shot in the $\omega_0 = 50$ µm focus of the laser. Assuming an ionisation efficiency of 1 for strong-field ionisation and a molecular-beam width of 1 mm, this yields a density of 9 x 10^6 cm^3. Derivation of this density assumes an ionisation efficiency of 1 for SFI and only takes into account the major assigned fragmentation channels for Ac-Phe-Cys-NH_2 [101] and thus strictly represent a lower limit of the density.

	SH—O isomer	SH—π isomer
A (Mhz)	340.181593	345.067516
B (MHz)	203.443113	215.965933
C (MHz)	159.877010	175.850323
μ_A (D)	0.768	6.789
μ_B (D)	2.406	-2.701
μ_C (D)	1.975	3.406

Table 5.1: Rotational constants and dipole moment vectors used for calculating the Stark effect.

Further to the deflection of the molecular beam, we observed a significant broadening of the spatial profiles. This is due to the dispersion of the different rotational states in the electric field, arising from the rotational-state-dependence of the Stark effect [29, 54]. This is shown in Figure 5.1 b for $J = 0 - 3$ states, indicating the larger effective dipole moment of lower-lying rotational states, leading to these states being deflected more, and hence the creation of a rotationally colder sample in the deflected beam [5, 105]. To extract approximate rotational temperatures and quantum-state distributions in the deflected beam, we have simulated particle trajectories through our setup for the different populated rotational states [29]. Spatial molecular-beam profiles were simulated by first calculating the Stark energies for each conformer for all rotational states up to $J = 50$, including all states up to $J = 70$ in the calculation, using the freely available `CMIstark` software package [54]. Rotational constants and dipole moment vectors were taken from the DFT calculations and are summarised in Table 5.1.

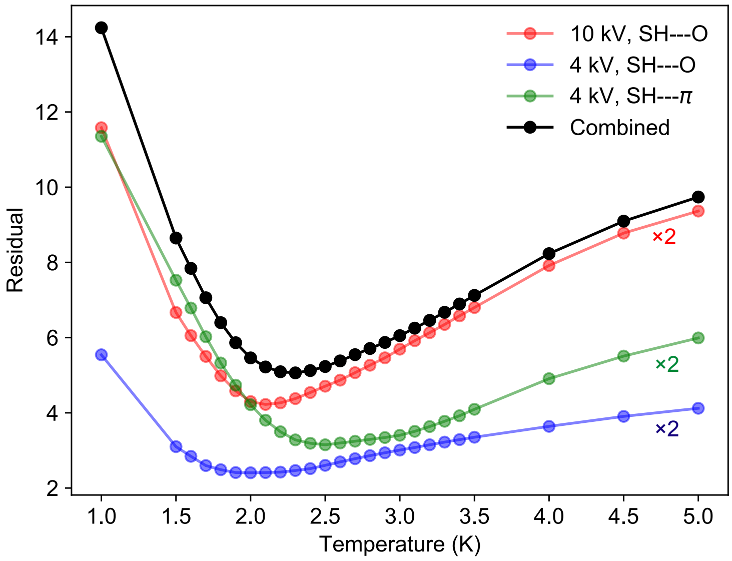

Figure 5.4: Residuals from fitting deflection profiles for different voltages and conformers as a function of temperature. Data for the SH—π conformer at 10 kV are not shown as only a constant background was observed. The sum of these residuals (black line) yielded a rotational temperature of 2.3 K.

Subsequently, for molecules in each quantum state we carried out classical trajectory simulations through the experimental setup, taking into account apertures and applying the appropriate forces when molecules are within the electrostatic deflector [29]. Finally, histograms of the final particle-position densities were determined at the interaction point and the contributions from each quantum state weighted by a Maxwell-Boltzmann distribution for a given initial temperature [105]. Simulated intensities for given conditions

– species and deflector voltage – were scaled with a single amplitude-scaling factor to compare with experimental data to account for additional losses and detection efficiency in the setup. The temperature that best described the experimental observations was determined by comparing the combined residuals, that is the absolute deviation between simulation and data, from all deflected data sets, excluding the SH—π conformer at 10 kV where only a constant low background was observed experimentally, for different rotational temperatures. These are shown in Figure 5.4 and from the combined residuals (black trace) a rotational temperature of 2.3 K for our molecular beam was extracted. Since the minima for individual deflection profiles deviate by $\sim$0.5 K, conservative error bounds for the rotational temperature are $\pm$0.5 K. Resulting simulated deflection profiles are shown as solid lines in Figure 5.3 a–c, which were obtained by applying a thermal-distribution weighting to the individual-state simulations, corresponding to the rotational temperature distribution from our laser desorption molecular beam source. We extract an approximate rotational temperature of 2.3 ± 0.5 K for the laser desorbed molecular beam.

Furthermore, we extract the quantum-state distribution within the deflected beam in Figure 5.3 e,f. These are shown in Figure 5.5 and indicate that the deflector creates a significantly colder ensemble. While this has a non-thermal rotational state distribution, the highest rotational states populated are approximately corresponding to a 1.5 K distribution. Even colder ensembles can be probed by moving the interaction region further into the deflected beam, this is indicated by the magenta and cyan distributions in Figure 5.5, evaluated at position 2.2 mm in the deflected beam, which are comparable to a 1.0 K average.

These results highlight the quantum-state sensitivity of the electrostatic deflection technique, allowing us to control conformer populations and rotational state distributions within the interaction region and creating samples well-suited for further control techniques such as alignment and orientation [5, 36, 44]. Moreover, ultrafast imaging experiments benefit from the significantly, typically several orders of magnitude, reduced density of carrier gas in the interaction region, which does not experience deflection in the electric field.

The presented approach is generally applicable to any polar molecule that can be vaporised by laser desorption and entrained in a molecular beam. The achievable degree of species separation depends crucially on the difference in dipole moment-to-mass-ratio [29, 109], and for small peptide systems we estimate that a difference of ∼20 % is sufficient for creating pure samples of the more polar species, whereas differences above ∼50 % should allow creation of a pure sample of either species, with improved setups enabling the separation for even smaller differences [110, 111]. The main limitation here is the creation of initially rotationally-cold samples in the desorption and entrainment process, such that an appreciable fraction of population is in the lower lying rotational states that exhibit the largest Stark shift. If this can be further improved, for example through the use of specially designed and higher pressure supersonic expansion valves [65], higher state purities or the separation of species with smaller dipole-moment differences will be achievable.

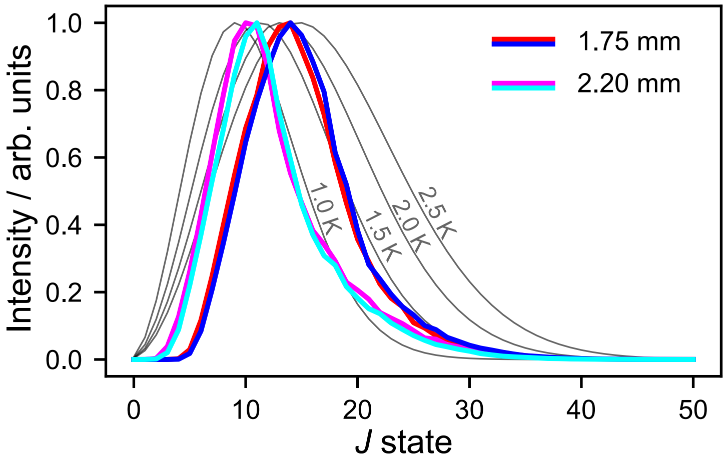

Figure 5.5: Relative population of rotational states in the molecular beam for the conformer-pure samples at two deflected positions, 1.75 mm (as in Figure 5.3) and 2.2 mm. Shown in grey are thermal distributions at various temperatures, as indicated. The red/magenta and blue/cyan lines indicate distributions for the SH–O and SH–π conformer, respectively.

5.3 Conclusion

We demonstrated the combination of laser desorption for the vaporisation of labile biological molecules with the electrostatic deflector for the spatial separation of conformational states and the creation of pure and rotationally-cold samples of individual conformers. Using the prototypical (di)peptide Ac-Phe-Cys-NH_2 as a model system, we showed that its two conformers, in the gas-phase, can be spatially separated and samples of either conformer can be obtained. The measured deflection was quantitatively understood using trajectory calculations, which furthermore allowed us to assign a rotational temperature of 2.3 ± 0.5 K for the beam from our laser desorption source. The generally good agreement between experiment and simulation also confirms the calculated dipole moments and that Stark effect calculations based on the rigid-rotor approximation are sufficient even for these large systems [112].

The created molecular samples will enable novel x-ray diffractive imaging experiments: they are conformer-pure beams that are well-separated from carrier gas and rotationally cold enough for strong laser alignment and orientation. The achieved densities of around 10^7 cm^{-3} are sufficient for high-resolution diffraction experiments at free-electron laser sources such as the European XFEL, which will deliver up to 26,000 pulses per second, allowing fast collection of data. This enables the collection of a diffraction image within 1 h [2], and simulated aligned-molecule diffraction patterns for the two conformers, showing marked differences, are shown in chapter 9. Our laser desorption source, with its low overall repetition rate, but reasonably long gas pulses of 100s of µs [101], is well-suited to the pulse-train structure of superconducting-LINAC-based XFELs [113]. The produced rotationally cold samples are well suited to strong-field alignment, which can be achieved using the available in-house laser systems available at FELs [114].

Our developed technique will more generally enable experiments on conformer-selected biological molecules with inherently non-species-specific experimental techniques, such as (sub-)femtosecond dynamics [73], reactive collision studies [96], or diffractive imaging [6]. This will open new pathways to study the intrinsic structure-function relationship of these basic molecular building blocks of the complex biochemical machinery.

5.4 Methods

A laser desorption source, described in detail in chapter 3, is used to vaporise the dipeptide Ac-Phe-Cys-NH_2 (APCN, 95% purity, antibodies-online GmbH), which is used without further purification. The resulting cold supersonic molecular beam is skimmed twice before entering the strong inhomogeneous field of the electrostatic deflector: once by a 2 mm skimmer (Beam Dynamics Inc. Model 50.8) 75 mm downstream of the expansion, and again by a 1 mm skimmer (Beam Dynamics Inc. Model 2) 409 mm downstream of the expansion. Within the strong inhomogeneous electric field of the deflector, molecules are dispersed according to their effective dipole moment-to-mass-ratio [29]. The molecular beam is skimmed once more with a 1.5 mm skimmer (Beam Dynamics Inc. Model 2) prior to entering the interaction region. This skimmer can be translated in height to ensure no part of the molecular beam is cut off. During measurements, data is collected for two skimmer positions and subsequently combined by keeping the highest intensity measured. The relative density of the conformers is probed via resonance-enhanced multi-photon ionisation (REMPI) [62]. The ultraviolet probe light is produced by frequency doubling the output of a dye laser (Radiant Dyes NarrowScan, using Coumarin 153 dye in methanol), pumped by the third harmonic of a Nd:YAG laser (Innolas, SpitLight 600). Typical laser-pulse energies were around 19 µJ loosely focused to a 100 µm spot in the interaction region.

The structures and dipole moments of Ac-Phe-Cys-NH_2 were calculated using the GAMESS software suite [115] using the B3LYP functional with a 6-311(p) basis set and confirmed against published structures [62].

6 Spatially Separated Conformers of Glycine

6.1 Introduction

Glycine is the smallest amino acid, and forms the back bone of every proteins structure. Its small size allows more accurate calculations for glycine than for other biomolecular building blocks, making it a good benchmark system for investigations toward understanding reactions of peptides. Three different conformers of glycine have been experimentally observed in the gas-phase [116, 117], a fourth conformer was theoretically predicted, but has not been detected in experiments [118, 119]. The molecular structures of the conformers are shown in Figure 6.1. Different conformers of the same structure can have different functions in nature and thus can have, for example, dramatically different charge migration dynamics [120]. Glycine is a good candidate for attosecond charge migration benchmark experiments [73, 121] and calculations for this have been performed already [45]. To realise this experiment, a cold molecular beam of glycine with spatially separated conformers, i. e., a conformer pure beam, is needed. Previous attempts to produce a cold beam of glycine by thermal evaporation in an Even-Lavie valve were unsuccessful and no intact glycine was observed in the beam [122].

Here, the laser desorption of glycine, followed by its deflection and production of a conformer-pure molecular beam is shown and compared to trajectory simulations.

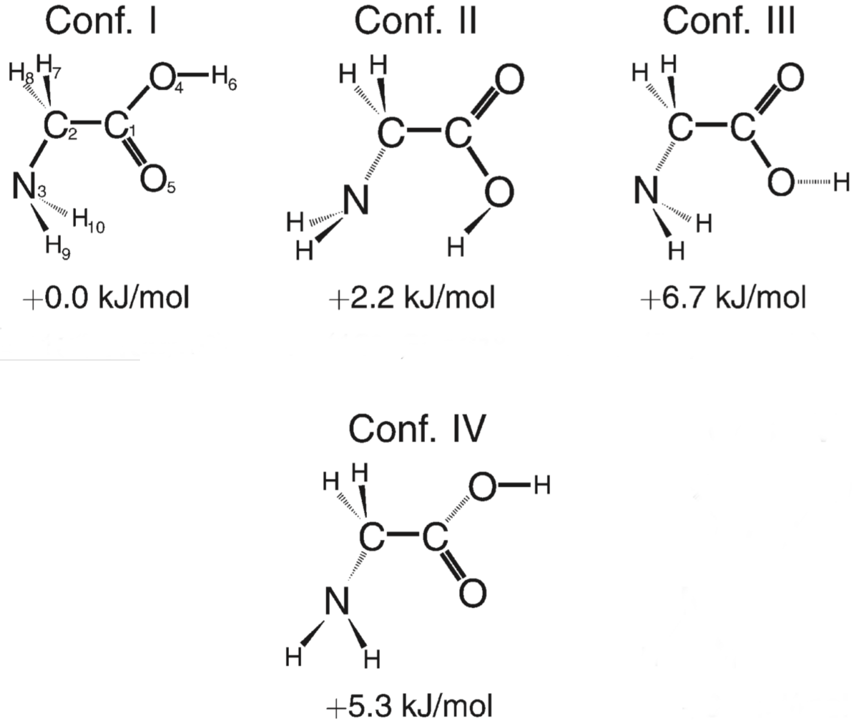
Conf. I
+0.0 kJ/mol
Conf. II
+2.2 kJ/mol
Conf. III
+6.7 kJ/mol
Conf. IV
+5.3 kJ/mol

Figure 6.1: The four different molecular structures of the glycine conformers. Figure adapted from [118]

6.2 Stark Interaction

Table 6.1: The dipole moments [19, 118, 123], experimentally observed populations [117–119] and the colours used in Figure 6.2 for the four conformers of glycine.

Conformer	Dipole moment in D	Experimental population in %	Colour coding
I	1.1	77(8)	red
II	5.5	10(2)	green
III	1.7	13(2)	black
IV	2.1	–	blue

In order to separate the different glycine conformers, we make use of their distinct dipole moments [29], as shown in Table 6.1. This dipole moment can interact with strong inhomogeneous electric fields due to the Stark effect, and leads to the exertion of a force $\vec{F} = -\mu_{\text{eff}}(\epsilon) \cdot \vec{\nabla}\epsilon$, on the molecules. As with the conformers of the dipeptide, the different forces acting on different conformers can be used to spatially separate them, as explained in chapter 2. Calculations for the interaction of the electric field with the four different conformers of glycine were performed using the `CMIstark` program [54].

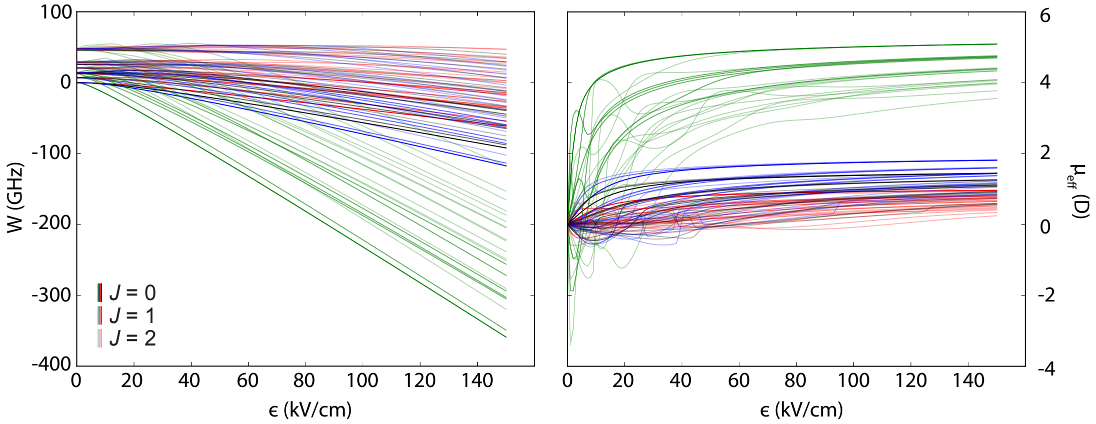

Figure 6.2: The calculated stark interactions, W, and effective dipole moments, μ_{eff}, as a function of the electric field ϵ for the four conformers of glycine. These are shown in red, green, black, and blue for conformer I, II, III, and IV, respectively. Different J states are indicated by different opacities.

The calculated Stark interaction in dependence of the electric field strength is shown in Figure 6.2, additionally the effective dipole moment as a function of the electric field is shown. All rotational states up to the total rotational angular momentum $J = 2$ for the four different conformers are shown. As previously, the different conformers are indicated by different colours (red, green, black and blue), while the total rotational angular momentum J of each state is indicated by different opacities. It is evident that conformer II (green) has a much larger effective dipole moment than the other three conformers. It thus experiences the largest force in an inhomogeneous electric field and can be spatially separated. The conformer I has the lowest dipole moment and thus will be enriched in the least deflected part of the molecular beam.

6.3 Glycin Time-of-Flight Mass Spectrum

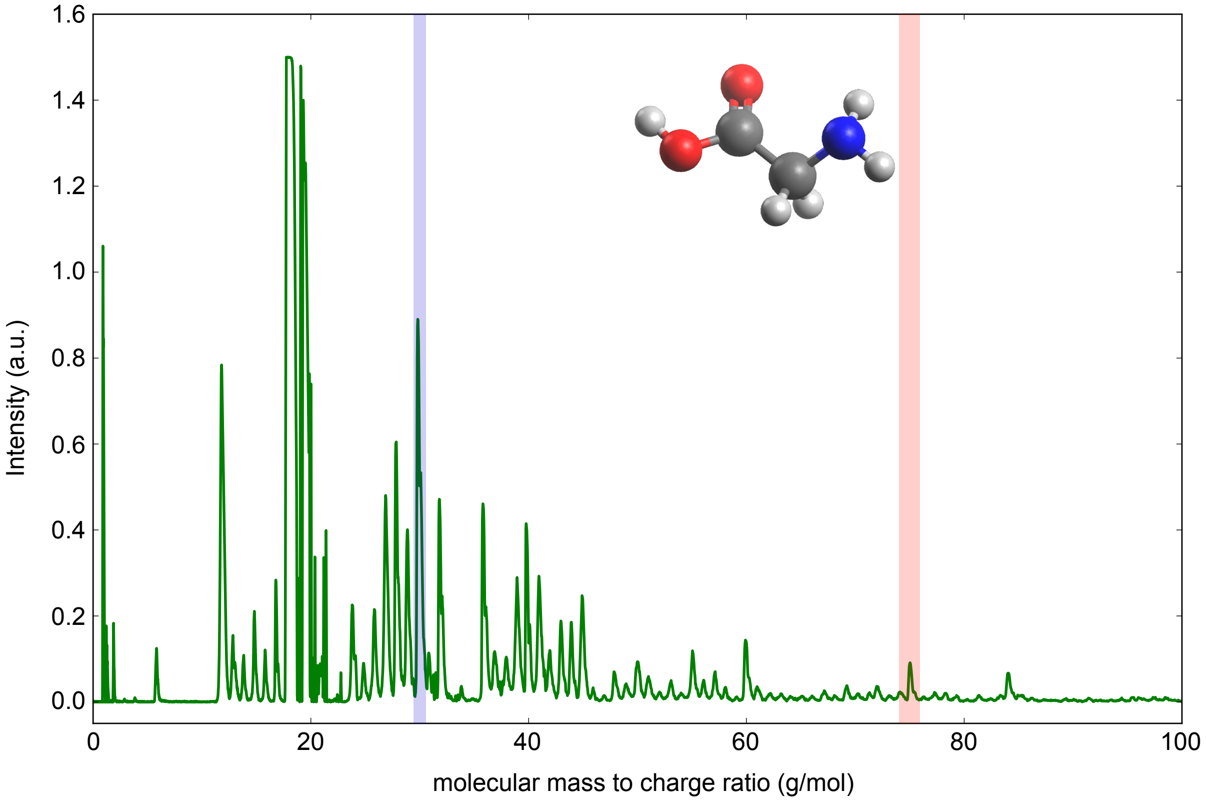

Figure 6.3: Time-of-flight mass spectrum of glycine following laser desorption. The glycine parent ion with mass 75 u is highlighted with red shading. A glycine fragment with mass a of 30 u is highlighted with blue shading. Other peaks correspond to carbon, carbon clusters, argon and protons.

The time-of-flight mass spectrum of glycine is measured following laser desorption in the experimental setup as described in section 3.3. The desorbed glycine is cooled with a helium or argon gas expansion from the pulsed piezo valve. Since there is no accessible resonance-enhanced multi-photon ionisation channel for glycine, all species present in the molecular beam are ionised *via* strong-field ionisation with a titanium-sapphire laser with a central wavelength of 800 nm, a duration of $\sim$ 40 fs and an approximate power density of $\sim$ 1 x 10^{14} W/cm^2.

The observed time-of-flight mass spectrum for glycine entrained in an argon expansion is shown in Figure 6.3. The parent mass of glycine, 75 u, is highlighted with red shading in the spectrum. Additionally, the glycine fragment with mass 30 u is highlighted with blue shading. The other peaks in the spectrum cannot be clearly assigned to any fragments from glycine and seem to correspond to carbon and carbon clusters (as previously observed in chapter 4), water, argon and protons. The time-of-flight mass spectrum clearly shows that it is possible to create a molecular beam containing intact glycine with a laser desorption source. However the number density of the parent ion is low, approximately 10^5 cm^{-3}, based on the number of observed ion per ionisation laser shot and assuming an ionisation efficiency of 1 for strong-field ionisation, see chapter 5 for details. If, however, the fragment with 30 u was created from parent ion fragmentation during the strong-field ionisation, and thus can be included in the density determination, the density of glycine would be approximately 5×10^6 cm^{-3}.

6.4 Electrostatic Deflection of Glycine

Deflection profiles of the glycine molecular beam were measured for deflector voltages of 0 kV, 4 kV and 14 kV. For these measurements the height of the ionisation laser was scanned to record a spatial profile of the molecular beam. The time-of-flight mass spectrum for each laser position was measured in event counting mode, i. e., an intensity threshold was set, here to 1.9 mV which corresponds to approximately a single ion hit, and everything above the threshold was saved as a hit and everything below was disregarded. All measured data for a certain laser position, typically a minimum of 36,000 shots, were combined. The total number of hits within a certain time bin, corresponding either to the parent or fragment mass of glycine, was then evaluated as a function of deflection coordinate, as shown in Figure 6.4 and Figure 6.5 . We, furthermore, show numerical trajectory simulations for deflection of the three conformers together (Figure 6.4, Figure 6.5 a), and of individual glycine conformers (Figure 6.5 b,c) [29]. These are shown in the figures as solid lines, and assume a rotational temperature of the molecular beam emerging from the laser desorption source of 2.5 K. Simulated profiles were obtained by first calculating the Stark effect and afterwards simulating particle trajectories for each conformer in each rotational quantum state up to $J = 20$. For each conformer a thermally-weighted deflection profile was then calculated, by weighting each quantum state with its thermal population at a given temperature, assuming Maxwell-Boltzmann statistics. Afterwards, the three populated conformers were combined into a single overall deflection profile, considering their relative population given in Table 6.1. Simulated deflection profiles for different temperatures were compared to the measured data, the best agreement was observed for a rotational temperature of 2.5 K, in good agreement with the rotational temperature extracted for the laser desorbed dipeptide (chapter 5).

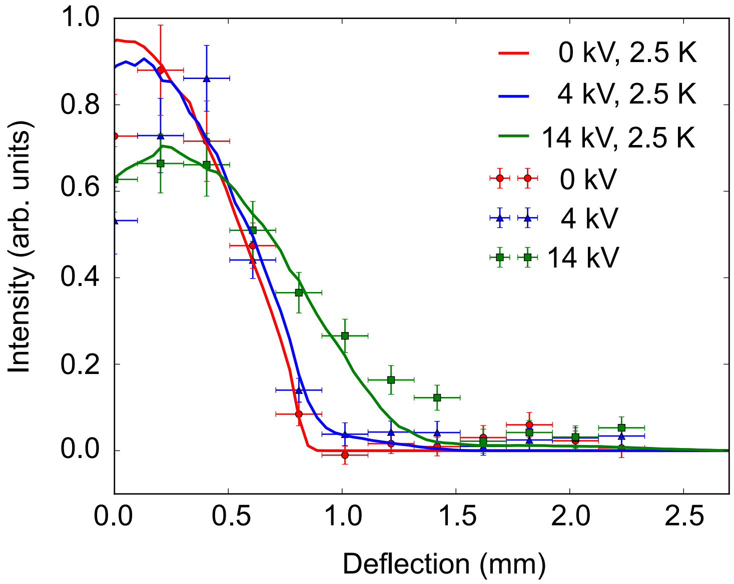

Figure 6.4: Intensity of the parent ion as a function of the deflection coordinate. The measurement was taken for voltages of 0 kV, 4 kV and 14 kV applied to the deflector and molecules were ionised by strong-field ionisation induced by a Ti:Sa femtosecond laser, a non-species-specific technique. The solid lines correspond to trajectory simulations for a rotational temperature of 2.5 K.

In Figure 6.4 the parent ion intensity in dependence of the deflection coordinate is shown for voltages of 0 kV, 4 kV, and 14 kV applied to the deflector. Points correspond to measured data, whereas the lines correspond to simulations at 2.5 K including the three populated conformers of glycine. The recorded deflection profiles show a clear deflection at an applied voltage of 14 kV, whereas at 4 kV only a small part of the beam is visibly deflected.

For the parent ion the observed signal was much lower than for the fragment with mass 30 u, as was the case in the time-of-flight mass spectrum shown in Figure 6.3. If we assume that the fragmentation of glycine that yields this fragment is induced by the strong-field ionisation from the femtosecond laser [124], the deflection profiles for both fragment and parent mass should be identical. The deflection profiles in Figure 6.4 for the parent and in Figure 6.5 a for the fragment show similar behaviour and hence indicate that the observed fragmentation was in large parts due to the strong-field ionisation probe. Due to the larger signal observed for the fragment the spatial profiles were much clearer than those for the parent ion.

In Figure 6.5 a the integrated intensity of the 30 u fragment is shown. Additionally, the simulated deflection for the individual conformers is shown for 4 kV, Figure 6.5 b, and 14 kV, Figure 6.5 c. It is evident that the deflection at 4 kV is from conformer II, which has the largest dipole moment (Table 6.1). Since the population of this conformer is only around 10 % of the total population, only a small part of the total intensity appears as deflected. Therefore, at a position of 1 mm a conformer-pure beam of glycine, containing only conformer II is created.

Furthermore, at higher applied voltages of 14 kV conformer II will be deflected out of the measurable interaction region and hence is significantly depleted from the remaining beam [29, 32]. At this position the molecular beam therefore predominantly contains conformers I and III. While these two conformers could not be fully separated from each other under current experimental conditions, the slight difference in dipole moments, Table 6.1, will lead to the production of population ratios at different spatial positions.

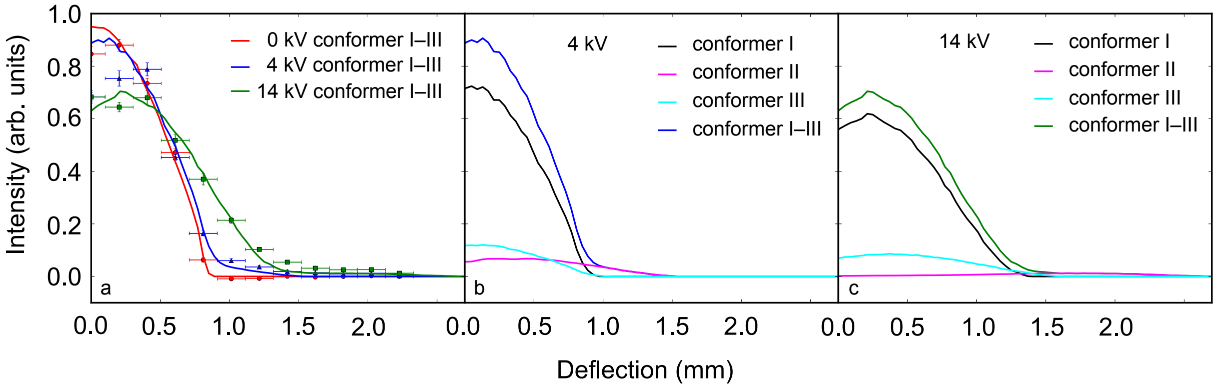

Figure 6.5: Intensity of the fragment ion (a) as a function of the deflection coordinate. The measurement was taken for voltages of 0 kV, 4 kV and 14 kV applied to the deflector and shown as data points. The solid lines correspond to trajectory simulations for a rotational temperature of 2.5 K. In (a) the trajectories are combined for the three conformers, whereas deflection profiles for the individual conformers are shown in (b) for 4 kV and in (c) for 14 kV.

6.5 Conclusion

It has been shown that intact glycine can be vaporised and entrained in a molecular beam of a noble gas with our laser desorption source. Comparison of measured data with numerical trajectory simulations showed that desorbed glycine molecules were cooled down to rotational temperatures of approximately 2.5 K by the supersonic expansion. Additionally, the spatial profile of the fragment showed a similar electrostatic deflection as those of the parent, indicated that that the fragment is mainly produced during the strong-field ionisation and not during the laser desorption process. It was found that conformer II of glycine can be spatially separated from the other populated conformers using electrostatic deflection and a conformer-pure molecular beam was produced at a voltage of 4 kV. Using higher deflection fields, conformer II can be depleted from the molecular beam, such that a molecular beam containing only conformers I and III was produced. The remaining beam consists mainly of conformer I, due to its much larger initial population. Using higher deflection fields or slower molecular beams one could potentially also separate conformer I and III. Already under current conditions the different dipole moments for conformers I and III produce different conformer population ratios at different positions in the deflected beam, such that differential analysis can be used to unravel the behaviour of each conformer [125]. These conformer-separated beams allow novel studies of the structure-function relationship and open the door for, e. g., attosecond charge migration experiments [45, 73].

7 Insulin in the Gas-Phase

In the future, we would like to vaporise and cool intact proteins with the laser desorption source. As a first test, we performed experiments with the prototypical protein bovine insulin. It was not necessary to be expected, that laser desorption works for such a large protein and if the optimised parameters are different for insulin due to different behaviour of the much higher mass. Additionally the supersonic expansion needs to provide much more collisions to cool and entrain insulin in the beam and the strong-field ionisation will probably not produce intact parent ions efficiently, but induce significant fragmentation. To establish that the laser desorption source successfully transfers such large molecules into vacuum, a time-of-flight mass spectrum was measured for insulin using the setup described in section 3.3. Sample bars were prepared as outlined before, section 3.4. Bovine insulin was purchased from Sigma-Aldrich and used without further purification. The sample was mixed with graphite powder in roughly the same ratio by volume as the dipeptide, ground, and rubbed on the sample bar.

Due to the low signal expected from insulin 135,000 single shot time-of-flight mass spectra were recorded to see if there is any insulin present in the molecular beam. During data analysis, the time-of-flight mass spectrum is four-fold binned, i. e., each set of four neighbouring points is averaged. Afterwards signal discrimination and event counting were used to convert data into events per laser shot.

The resulting time-of-flight mass spectrum is shown in Figure 7.1. In the mass region up to 300 u a large amount of carbon and carbon clusters are visible, these carbon contributions are marked with asterisks in the spectrum. Similar carbon clustering was observed previously, as discussed in chapter 4. Due to the low insulin signal levels and the large carbon contribution it is impossible to say if there is any signal from insulin fragments in the mass region below 300 u. The inset in Figure 7.1 shows a zoom in of the same spectrum to highlight the low intensities at higher masses. At these higher masses some small peaks are visible, which we tentatively assign as originating from insulin. The peaks are labelled with numbers from one to four and correspond to the approximate mass to charge ratios of 1040 u, 5800 u, 8300 u and 9620 u, respectively. The given masses are approximate due to the low mass resolution of the spectrometer and the lack of known mass peaks that can be used for accurate calibration at these high masses. The parent mass of insulin is around 5800 u, such that signal 2 might correspond to the singly charged monomer of insulin.

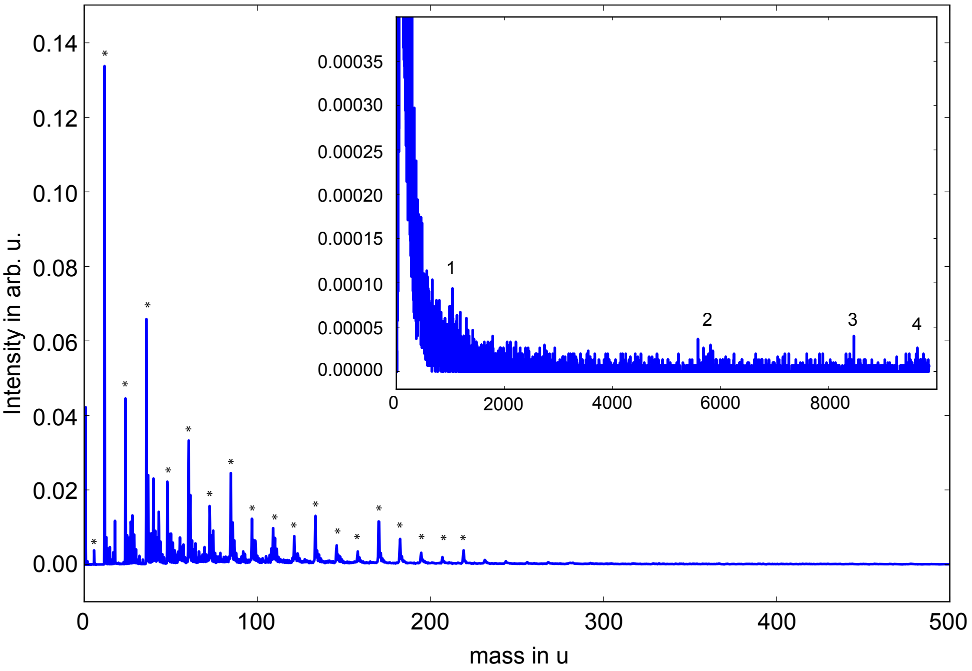

Figure 7.1: Time-of-flight mass spectrum of bovine insulin. Peaks corresponding to carbon and carbon clusters are labelled with asterisks. The labelled peaks 1 to 4 correspond to mass to charge ratios of 1040 u, 5800 u, 8300 u and 9620 u, respectively.

To ensure the observed signal does originate from laser desorbed insulin, a time-of-flight mass spectrum with 110,000 single shots is taken with the desorption laser turned off. The data is treated in the same way and plotted on an identical scale and shown in Figure 7.2. At low masses two signals are visible, which correspond to water and argon. At higher masses we observe significantly less signal compared to the spectrum with desorption laser on. The mass peaks labelled 1 and 2 in Figure 7.2 correspond to approximately 420 u and 6140 u, respectively. The background spectrum looks very different than the insulin spectrum, even at higher masses. This is a clear indication for vaporisation of intact insulin, albeit at very low detected signal levels, corresponding to approximately 3 ions within 100,000 shots.

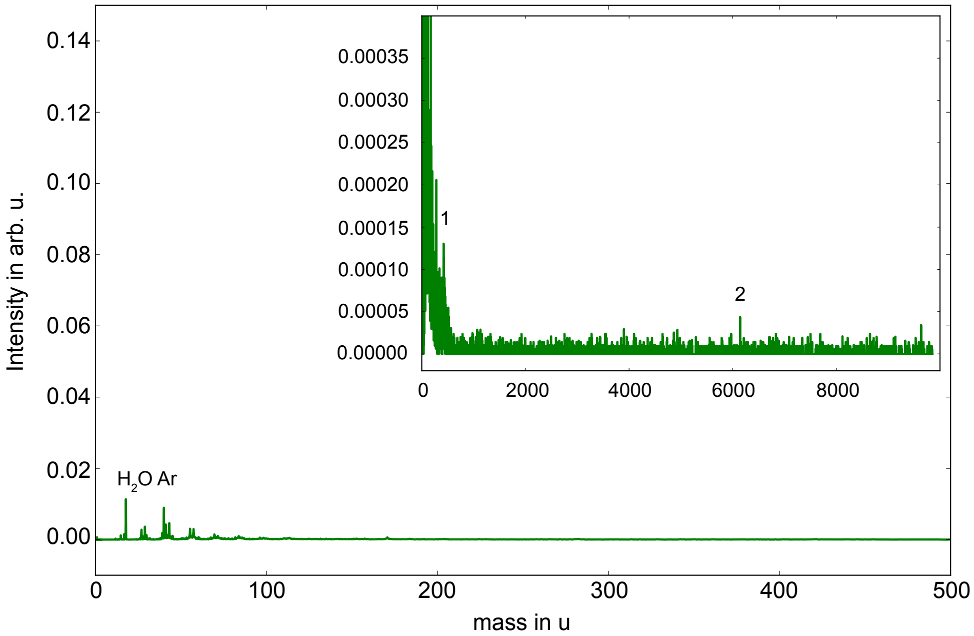

Figure 7.2: Time-of-flight mass spectrum under identical conditions as in Figure 7.1, but with desorption laser off. Peaks due to water, argon and some background at higher masses are visible.

We identify three main reasons for the low signal levels observed. First, in the setup used the distance from the desorption source to the interaction region between the velocity map imaging electrodes was around 74 cm, because in this machine the electrostatic deflector was mounted. This large distance, the three skimmers of sizes 2 mm, 1 mm and

1.5 mm lead partly to the low signal levels. This distance can easily be reduced by a factor of 3 in a different setup, which should yield approximately 9 times higher signal levels. Secondly, the micro-channel plate detector used is operating much less efficient at these high masses, because heavy ions do not accelerate to high enough velocities to generate the impact needed [126]. Hence, to increase the observable signal levels the detector could be exchanged against one more suitable for larger molecules. For example, cryogenic microcalorimeter [127], nanomechanical resonators [128] or a nanomembrane detector [129]. Thirdly, one should consider that the same amount of sample in the sample-graphite-mixture by volume was used. Assuming the same density for insulin and the dipeptide this would yield approximately 20 times fewer molecules on the sample bar for insulin than for the dipeptide. These suggested improvements, especially the use of a mass spectrometer and a detector optimised for higher masses, should allow the operation and optimisation of the laser desorption source for intact proteins.

8 Suggested Improvements of the Laser Desorption Source

The laser desorption source build up as a part of this thesis is a prototype, but the newly developed source is working well and allowed for the first time the characterisation of laser desorption using strong-field ionisation, the production of rotationally very cold beams of, for example, Ac-Phe-Cys-NH_2 and the spatial separation of dipeptide conformers. However, based on the gained experience suggestions for improving the source came up. Since the improvements require technical changes it was not possible to implement them within the time frame of this thesis and they are briefly outlined below. Several of the developments suggested here are currently under construction, because the machine is under preparation for an upcoming beam time at FLASH at the moment.

One of the biggest drawbacks of laser desorption is that the sample bar needs to be exchanged frequently and even with the load-lock system this takes around 15 to 20 minutes. In the laboratory, where the measurement time is not restricted, the sample bar exchange time is no issue, but for beam times at central facilities with restricted time, e. g., at free-electron lasers, it would be useful to shorten this time where not data can be collected. To realise this it would be useful to have a stack, or at least one already prepared sample bar, in the load-lock, so that the sample bar can be changed without venting the load-lock system. If the last prepared sample bar of the stack is in the source chamber and being used, the stack in the load-lock can be refilled with freshly prepared sample bars. With this the sample bar exchange would only take around 2 min. Such a load-lock system is currently under construction in the group and will be implemented shortly.

Another idea to solve the issue of constantly changing the sample bar is to produce the sample bar itself out of the sample of interest, similar to an ablation source [130], or of the sample mixed with graphite, for example, pressed to a disk [80]. In this case the sample bar needs to be driven back and forth constantly instead of exchanged. But also this idea has potential issues, e. g., the desorbed surface might get hot and destroy the sample. Additionally, for a sample bar pressed out of sample a lot of sample is required and depending on the biological molecule of interest it might be difficult to produce or expensive to buy a sufficient amount. Hence this was not possible for Ac-Phe-Cys-NH_2 and was not considered in the measurements for this thesis but the possibility of pressing a disk should be considered depending on the molecule in use.

The deflector used in this work has only a small channel for the molecular beam to pass through. Therefore, the molecular beam was skimmed with a 1 mm skimmer before the deflector and the outer part of the molecular beam was cut off. With the b-type deflector [110] recently developed in our group the distance between the rods of the deflector is larger, such that a larger part of the molecular beam can pass the deflector and reach the interaction region. Additionally, the field strengths that can now be reached with the b-type deflector are larger and furthermore deflected molecules do not collide with the deflector electrodes any more, even at large deflections. Therefore, it would be useful to exchange the deflector against the new b-type deflector to increase the signal levels and the achievable spatial separation. To improve the separation further a moveable knife edge between the deflector and the detection region has been shown to increase the purity of the deflected beam, as it cuts away undeflected sample [111]. Thus it would be useful to implement a knife edge into the setup to improve the purity of the deflected beam. This is beneficial if the conformers have small dipole moment differences, e. g., conformers I and III of glycine. These two developments were just recently demonstrated in the group, and an experimental setup combining laser desorption with the b-type deflector is currently being designed.

The required measurement times are quite long with the current laser desorption source because of the low repetition rate of 20 Hz and the necessary sample bar exchange. If the repetition rate is increased, much more data can be collected in a shorter time. Especially for measurement campaigns at free-electron lasers, where the repetition rate usually is higher and the measurement time is restricted, it would be useful to match the repetition rate with the desorption source. While at the LCLS the repetition rate is 120 Hz, and this could be matched with a new desorption YAG laser operating at this repetition rate, this is not the case for FELs operating in burst mode, such as the European XFEL. However, here the long gas pulses from the laser desorption source can be used to interact with several pulses in the pulse train. One disadvantage of a higher repetition rate is that the sample bar needs to be moved faster and thus needs to be changed more frequently. If the improvements from above are considered, especially the sample bar stack in the load-lock, it might be possible to have a reasonable duty cycle of the source and shorter measurement times with higher repetition rates.

The above mentioned suggestions will improve the achievable molecular density and increase the duty cycle of the laser desorption source. It is certain that these suggestions will improve the source and several of them are currently under development.

The suggestions below are of a more experimental nature and should be considered as potential projects for a upcoming bachelor or masters thesis at the laser desorption source.

Currently the desorption laser spot is circular with a diameter of around 0.6 mm, but this might not be the ideal shape for laser desorption. To get the highest density the desorption laser should be as long as the sample bar channel in the z-direction, which is 1.2 mm, but narrow in the y-direction, which will lead to an elliptic shape. This would ensure that all sample desorbed by the laser is fresh and not hit before by the laser and there is no loss of molecules in the y-direction, because of inefficient picking up by the noble gas expansion. Additionally all molecules on the sample bar are desorbed in the z-direction, which might increase the density but, unfortunately, this might also effect the cooling as not all molecules are desorbed at the same distance from the supersonic expansion.

It might help to increase density in the beam if more sample is desorbed. Therefore, more sample needs to be deposited on the sample bar. The issue with a thick sample layer is that the sample clings strongly to itself, but not to the sample bar. This leads to sample being ‘shot of’ by the desorption laser. A funnel shape at the top of the sample bar would help to stop the desorption laser dropping off the sample and more sample can be deposited on the sample bar.

The piezo valve can be exchanged against an Even-Lavie valve, which promises to produce a denser supersonic expansion. This could lead to more efficient entrainment in the molecular beam and collisional cooling of the biomolecule of interest [65, 131].

For the optimisation and understanding of the source it would be beneficial if the angle movement of the source, enabled by the mechanical hinge described in subsection 3.2.4, is additionally motorised and could be optimised to the highest signal levels during a measurement. The same is valid for the focus size of the desorption laser spot.

In the measurements presented in this thesis the sample of interest is cooled with a pulsed argon or helium expansion. If the biomolecule of interest gets larger the cooling is not so efficient with light gases and heavier noble gases, for example krypton or xenon, could be used to ensure a sufficient cooling.

Molecules after desorption are hot and have significant kinetic energy. The molecules are entrained in the supersonic expansion and their kinetic energy in the XY-directions needs to be quenched by this expansion, otherwise they will not be carried within the molecular beam. It might be the case that a lot of desorbed molecules are lost because they have to much kinetic energy. A new valve design where the desorption is closer to the nozzle of the valve or even inside the valve before the expansion [132, 133] could help, as the density of the noble gas is significantly higher here.

Despite all these suggestions for improvements the laser desorption source is working well in its current status and enabled us to conduct the measurements described in this thesis. But it is the nature of experimental science that even working systems can be improved further and the suggestions given here could be a good starting points for the future.

9 Summary and Outlook

One of the major goals of the *controlling the motion of large and complex particles* (COMOTION) project within the *controlled molecule imaging* (CMI) group is to enable structure and dynamics experiments of large and complex biological systems at x-ray free electron lasers, with high spatial and temporal resolution. The first step to enable these experiments is to transfer biological molecules intact into the gas-phase. The next step is to make sure the sample contains only a single structure, i. e., is conformationally pure. These two important milestones were realised in this thesis by a laser desorption setup combined with electrostatic deflection.

In chapter 2 the basic theoretical background for these experiments is given, while chapter 3 describes the laser desorption source in detail, including the considerations made during the design.

In chapter 4 the characterisation and optimisation of the source towards producing higher densities of intact molecules is described. As a probe strong-field ionisation is used for the first time in combination with laser desorption. This acts as a universal probe and ionises all species present in the interaction volume, which allowed us to identify all species in the molecular beam, including carbon clusters produced during the desorption process. With this ionisation technique it was found that the fragmentation and thus the cooling efficiency is influenced by the placement of the desorbed plume within the supersonic expansion.

After the characterisation the spatial separation of two conformers of the dipeptide Ac-Phe-Cys-NH_2 is shown in chapter 5. This used the combination of a laser desorption source with an electrostatic deflector and the rotational temperature of the molecular beam is found to be 2.3 ± 0.5 K. The efficiency of the Stark calculations and the functionality of the rigid-rotor model even for large molecules is confirmed by the good agreement of the simulation with the experimental data. Ac-Phe-Cys-NH_2 is the largest molecule which has been conformer separated by the electrostatic deflector so far. Containing nearly 3 times as many atoms as the previous largest molecule hydroquinone [33]. This separation and the achieved density of around 10^7 cm^{-3} are crucial steps towards investigations of structure and dynamics experiments at free-electron lasers. Additionally, the conformer separation was also achieved for glycine, as discussed in chapter 6.

As final demonstration bovine insulin is used as a large prototypical protein with the laser desorption source in chapter 7. There are clear indications that a molecular beam containing intact insulin was successfully produced.

The laser desorption source in combination with electrostatic deflection opens the door for novel experiments, such as conformer depended studies with non-species-specific techniques, e. g., x-ray diffraction [6] or fragmentation studies [134, 135]. Although these measurements have not been performed during this work, the important steps that enable these experiments were demonstrated; the characterisation and optimisation of a laser desorption source, the production of rotationally very cold molecular beams using laser desorption, enabling alignment and orientation, and the creation of a conformer-pure molecular beam of a large biological molecule. In future this thesis will enable several novel experiments, some of which are briefly outlined below.

Conformer-Resolved Fragmentation

The conformer separated molecular beams produced here contain neutral molecules, therefore the density is not limited by the space-charge limit and the structure is not influenced by excess charge. This enables the study of intra-molecular interactions separately for different conformers, which can, for example, give information about the different folding of proteins. This can be achieved by analysing the photon-induced fragmentation patterns following soft x-ray ionisation [134]. To conduct this experiment we have applied and received beam time at the free-electron laser FLASH in Hamburg to study the conformational fragmentation of spatially separated conformers of Ac-Phe-Cys-NH_2, shown in Figure 9.1.

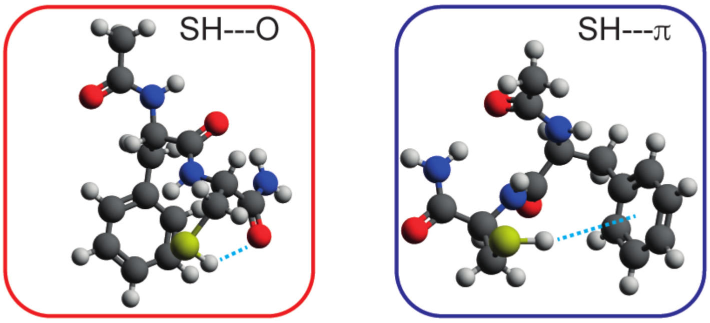

Figure 9.1: The two conformers of Ac-Phe-Cys-NH_2 with the different hydrogen bonding highlighted.

The tunable soft x-ray radiation at FLASH enables site-specific ionisation by setting the photon wavelength to specific atomic resonances. In particular we will ionise at the sulphur ($2p$ edge) in the Cysteine residue. Since the two conformers exhibit different hydrogen bonding at this site, as shown in Figure 9.1, we expect different fragmentation pathways following core-ionisation at the sulphur. We can, therefore, study the influence of the intramolecular interactions on fragmentation in detail in a bottom-up approach.

Conformational Switching Dynamics

A conformer separated beam will allow the investigation of conformational switching dynamics [136, 137]. For these experiments one pure conformer is pumped into the other conformation and the ensemble is probed *via* a species-specific technique, such as resonance-enhanced multi-photon ionisation as used in chapter 5 or *via* diffractive imaging. By varying the pump-probe temporal delay the time-scale and dynamics of the switching can be investigated directly.

Microsolvation of Biomolecules

Biomolecules in nature, e. g., in the cell, are not isolated but surrounded by water. To investigate water-biomolecule interactions, molecular clusters containing a single biomolecule surrounded by water could be used. These can be produced by enriching the noble gas expansion with water before the expansion. Most probably the produced water-biomolecule complexes have distinct dipole moments and thus can be separated with the electrostatic deflector, as has been demonstrated for smaller systems, such as indole-water clusters [112] and hydroquinone-water clusters [33]. This allows them to be investigated individually, for example, the hydrogen bond from the water to the biomolecule can be studied by looking at the fragmentation following side-specific ionisation [122, 138].

Diffractive Imaging

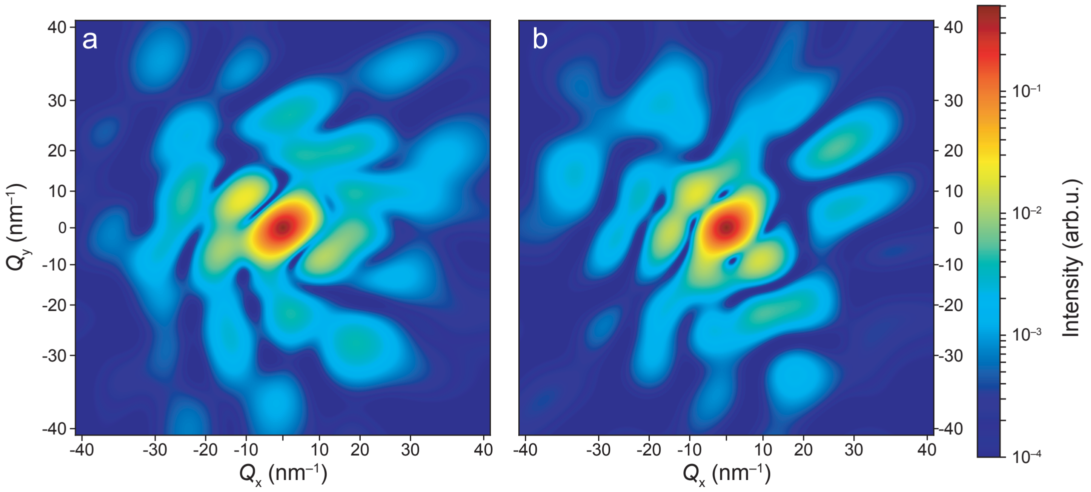

Figure 9.2: Simulated diffraction of the two conformers of Ac-Phe-Cys-NH_2, (a) shows the SH–O bonded conformer and (b) the SH–π bonded conformer . Molecules are assumed perfectly oriented in the most polarisable axis system, incoherent diffraction and noble gas background are not considered. The x-ray polarisation is horizontal in the shown images.

The production of cold and conformer separated molecular beams is the crucial first step towards diffractive imaging of individual biomolecules. The next step is the alignment and orientation of molecules in space. Once this is achieved, the individual diffraction pattern could be recorded at a XFEL [2], as it has been demonstrated in a recent proof of principal experiment with diiodobenzonitrile [6, 60]. The collection of the data for one diffraction image will take around 1 h at the European XFEL, which will deliver up to 26,000 pulses per second [2]. The differences in the diffraction pattern for the two conformers of the dipeptide Ac-Phe-Cys-NH_2 that could be separated, see chapter 5, are clearly observable, as shown in Figure 9.2. This shows simulated diffraction patterns obtained with the CMIdiffract software [122]. Simulations assumed perfect orientation, no incoherent scattering, nor noble gas background, a photon energy of 9.5 keV and typical beamline parameters and detectors currently available (AMO beamline at LCLS). These measurements, enabled by the new laser desorption source combined with the electrostatic deflector, will enable the direct measurement of structural dynamics with high spatial and temporal resolution and thus recording of true ‘molecular movies’.

Bibliography

[1] J. L. Hansen, J. H. Nielsen, C. B. Madsen, A. T. Lindhardt, M. P. Johansson, T. Skrydstrup, L. B. Madsen, and H. Stapelfeldt, Journal of Chemical Physics **136**, 204310 (2012).

[2] A. Barty, J. Küpper, and H. N. Chapman, Annu. Rev. Phys. Chem. **64**, 415 (2013).

[3] K. Pande, C. D. M. Hutchison, G. Groenhof, A. Aquila, J. S. Robinson, J. Tenboer, S. Basu, S. Boutet, D. P. DePonte, M. Liang, T. A. White, N. A. Zatsepin, O. Yefanov, D. Morozov, D. Oberthuer, C. Gati, G. Subramanian, D. James, Y. Zhao, J. Koralek, J. Brayshaw, C. Kupitz, C. Conrad, S. Roy-Chowdhury, J. D. Coe, M. Metz, P. L. Xavier, T. D. Grant, J. E. Koglin, G. Ketawala, R. Fromme, V. Šrajer, R. Henning, J. C. H. Spence, A. Ourmazd, P. Schwander, U. Weierstall, M. Frank, P. Fromme, A. Barty, H. N. Chapman, K. Moffat, J. J. van Thor, and M. Schmidt, Science **352**, 725 (2016).

[4] R. Neutze, R. Wouts, D. van der Spoel, E. Weckert, and J. Hajdu, Nature **406**, 752 (2000).

[5] F. Filsinger, G. Meijer, H. Stapelfeldt, H. Chapman, and J. Küpper, Phys. Chem. Chem. Phys. **13**, 2076 (2011), arXiv:1009.0871 [physics] .

[6] J. Küpper, S. Stern, L. Holmegaard, F. Filsinger, A. Rouzée, A. Rudenko, P. Johnsson, A. V. Martin, M. Adolph, A. Aquila, S. Bajt, A. Barty, C. Bostedt, J. Bozek, C. Caleman, R. Coffee, N. Coppola, T. Delmas, S. Epp, B. Erk, L. Foucar, T. Gorkhover, L. Gumprecht, A. Hartmann, R. Hartmann, G. Hauser, P. Holl, A. Hömke, N. Kimmel, F. Krasniqi, K.-U. Kühnel, J. Maurer, M. Messerschmidt, R. Moshammer, C. Reich, B. Rudek, R. Santra, I. Schlichting, C. Schmidt, S. Schorb, J. Schulz, H. Soltau, J. C. H. Spence, D. Starodub, L. Strüder, J. Thøgersen, M. J. J. Vrakking, G. Weidenspointner, T. A. White, C. Wunderer, G. Meijer, J. Ullrich, H. Stapelfeldt, D. Rolles, and H. N. Chapman, Phys. Rev. Lett. **112**, 083002 (2014), arXiv:1307.4577 [physics] .

[7] U. Lorenz, N. M. Kabachnik, E. Weckert, and I. A. Vartanyants, Phys. Rev. E **86**, 051911 (2012), arXiv:1206.6960 [physics] .

[8] B. Ziaja, H. N. Chapman, R. Fäustlin, S. Hau-Riege, Z. Jurek, A. V. Martin, S. Toleikis, F. Wang, E. Weckert, and R. Santra, New J. Phys. **14**, 115015 (2012).

[9] K. J. Gaffney and H. N. Chapman, Science **316**, 1444 (2007).

[10] J. C. H. Spence and R. B. Doak, Phys. Rev. Lett. **92**, 198102 (2004).

[11] H. Stapelfeldt and T. Seideman, Rev. Mod. Phys. **75**, 543 (2003).

[12] F. Filsinger, U. Erlekam, G. von Helden, J. Küpper, and G. Meijer, Phys. Rev. Lett. **100**, 133003 (2008), arXiv:0802.2795 [physics] .

[13] F. Filsinger, J. Küpper, G. Meijer, J. L. Hansen, J. Maurer, J. H. Nielsen, L. Holmegaard, and H. Stapelfeldt, Angew. Chem. Int. Ed. **48**, 6900 (2009).

[14] M. Karas, D. Bachmann, and F. Hillenkamp, Anal. Chem. **57**, 2935 (1985).

[15] K. Dreisewerd, Chem. Rev. **103**, 395 (2003).

[16] V. V. Golovlev, S. L. Allman, W. R. Garrett, N. I. Taranenko, and C. H. Chen, Int. J. Mass Spectrom. Ion Processes **169–170**, 69 (1997).

[17] F. J. Vastola and A. J. Pirone, Adv. Mass Spectrom. **4**, 107 (1968).

[18] J. R. Cable, M. J. Tubergen, and D. H. Levy, J. Am. Chem. Soc. **109**, 6198 (1987).

[19] F. J. Lovas, Y. Kawashima, J. U. Grabow, R. D. Suenram, G. T. Fraser, and E. Hirota, Astrophys. J. **455**, L201 (1995).

[20] E. R. Russo, Appl. Spectrosc. **49**, 14A (1995).

[21] A. M. Rijs and J. Oomens, eds., "IR spectroscopic techniques to study isolated biomolecules," in *Gas-Phase IR Spectroscopy and Structure of Biological Molecules* (Springer Verlag, 2015) Chap. 1, pp. 1–42.

[22] R. Tembreull and D. M. Lubman, Anal. Chem. **59**, 1003 (1987).

[23] G. Meijer, M. S. de Vries, H. E. Hunziker, and H. R. Wendt, Appl. Phys. B **51**, 395 (1990).

[24] E. Nir, K. Kleinermanns, and M. S. de Vries, Nature **408**, 949 (2000).

[25] M. S. de Vries and P. Hobza, Annu. Rev. Phys. Chem. **58**, 585 (2007).

[26] J. M. Bakker, C. Plützer, I. Hünig, T. Häber, I. Compagnon, G. von Helden, G. Meijer, and K. Kleinermanns, Chem. Phys. Chem. **6**, 120 (2005).

[27] S.-i. Ishiuchi, K. Yamada, H. Oba, H. Wako, and M. Fujii, Phys. Chem. Chem. Phys. **18**, 23277 (2016).

[28] J. M. Bakker, L. M. Aleese, G. Meijer, and G. von Helden, Phys. Rev. Lett. **91**, 203003 (2003).

[29] Y.-P. Chang, D. A. Horke, S. Trippel, and J. Küpper, Int. Rev. Phys. Chem. **34**, 557 (2015), arXiv:1505.05632 [physics] .

[30] E. Wrede, Z. Phys. **44**, 261 (1927).

[31] O. Stern, Z. Phys. **39**, 751 (1926).

[32] T. Kierspel, D. A. Horke, Y.-P. Chang, and J. Küpper, Chem. Phys. Lett. **591**, 130 (2014), arXiv:1312.4417 [physics] .

[33] H. S. You, J. Kim, S. Han, D.-S. Ahn, J. S. Lim, and S. K. Kim, J. Phys. Chem. A **122**, 1194 (2018).

[34] H. J. Loesch and A. Remscheid, J. Chem. Phys. **93**, 4779 (1990).

[35] B. Friedrich and D. R. Herschbach, Z. Phys. D **18**, 153 (1991).

[36] L. Holmegaard, J. H. Nielsen, I. Nevo, H. Stapelfeldt, F. Filsinger, J. Küpper, and G. Meijer, Phys. Rev. Lett. **102**, 023001 (2009), arXiv:0810.2307 [physics] .

[37] O. Ghafur, A. Rouzée, A. Gijsbertsen, W. K. Siu, S. Stolte, and M. J. J. Vrakking, Nat. Phys. **5**, 289 (2009).

[38] S. De, I. Znakovskaya, D. Ray, F. Anis, N. G. Johnson, I. A. Bocharova, M. Magrakvelidze, B. D. Esry, C. L. Cocke, I. V. Litvinyuk, and M. F. Kling, Phys. Rev. Lett. **103**, 153002 (2009), arXiv:0907.3250 [physics] .

[39] P. M. Kraus, D. Baykusheva, and H. J. Wörner, Phys. Rev. Lett. **113**, 023001 (2014), arXiv:1311.3923 [physics] .

[40] J. J. Larsen, H. Sakai, C. P. Safvan, I. Wendt-Larsen, and H. Stapelfeldt, J. Chem. Phys. **111**, 7774 (1999).

[41] C. J. Hensley, J. Yang, and M. Centurion, Phys. Rev. Lett. **109**, 133202 (2012).

[42] L. Holmegaard, J. L. Hansen, L. Kalhøj, S. L. Kragh, H. Stapelfeldt, F. Filsinger, J. Küpper, G. Meijer, D. Dimitrovski, M. Abu-samha, C. P. J. Martiny, and L. B. Madsen, Nat. Phys. **6**, 428 (2010), arXiv:1003.4634 [physics] .

[43] C. Z. Bisgaard, O. J. Clarkin, G. Wu, A. M. D. Lee, O. Geßner, C. C. Hayden, and A. Stolow, Science **323**, 1464 (2009).

[44] V. Kumarappan, C. Z. Bisgaard, S. S. Viftrup, L. Holmegaard, and H. Stapelfeldt, J. Chem. Phys. **125**, 194309 (2006).

[45] D. Ayuso, A. Palacios, P. Decleva, and F. Martin, Phys. Chem. Chem. Phys. **19**, 19767 (2017).

[46] W. Gordy and R. L. Cook, *Microwave Molecular Spectra*, 3rd ed. (John Wiley & Sons, New York, NY, USA, 1984).

[47] G. Scoles, ed., *Atomic and molecular beam methods*, Vol. 1 & 2 (Oxford University Press, New York, NY, USA, 1988 & 1992).

[48] J. M. Hollas, *Moderne Methoden in der Spektroskopie* (Vieweg, Braunschweig, 1995).

[49] W. Demtröder, *Molekülphysik* (Oldenbourg Wissenschaftsverlag, München, 2003).

[50] P. Atkins and J. de Paula, *Physical Chemistry*, 8th ed. (Oxford University Press, 2006).

[51] S. Y. T. van de Meerakker, H. L. Bethlem, N. Vanhaecke, and G. Meijer, Chem. Rev. **112**, 4828 (2012).

[52] P. Atkins, J. de Paula, and R. Friedman, *Physical Chemistry, Quanta, Matter, and Change*, 2nd ed. (Oxford University Press, 2014).

[53] F. J. Lovas, J. S. Coursey, S. A. Kotochigova, J. Chang, K. Olsen, and R. A. Dragoset, eds., *NIST Triatomic Spectral Database* (2018).

[54] Y.-P. Chang, F. Filsinger, B. Sartakov, and J. Küpper, Comp. Phys. Comm. **185**, 339 (2014), arXiv:1308.4076 [physics] .

[55] G. M. Barrow, *Introduction to Molecular Spectroscopy*, 1st ed. (McGraw-Hill, 1962).

[56] S. Y. T. van de Meerakker, H. L. Bethlem, and G. Meijer, Nat. Phys. **4**, 595 (2008).

[57] D. H. Levy, Science **214**, 263 (1981).

[58] M. Schnell and G. Meijer, Angew. Chem. Int. Ed. **48**, 6010 (2009).

[59] M. Hillenkamp, S. Keinan, and U. Even, J. Chem. Phys. **118**, 8699 (2003).

[60] S. Stern, L. Holmegaard, F. Filsinger, A. Rouzée, A. Rudenko, P. Johnsson, A. V. Martin, A. Barty, C. Bostedt, J. D. Bozek, R. N. Coffee, S. Epp, B. Erk, L. Foucar, R. Hartmann, N. Kimmel, K.-U. Kühnel, J. Maurer, M. Messerschmidt, B. Rudek, D. G. Starodub, J. Thøgersen, G. Weidenspointner, T. A. White, H. Stapelfeldt, D. Rolles, H. N. Chapman, and J. Küpper, Faraday Disc. **171**, 393 (2014), arXiv:1403.2553 [physics] .

[61] K. Luria, W. Christen, and U. Even, J. Phys. Chem. A **115**, 7362 (2011).

[62] B. Yan, S. Jaeqx, W. J. van der Zande, and A. M. Rijs, Phys. Chem. Chem. Phys. **16**, 10770 (2014).

[63] A. Rijs, "*private communication*," (2014).

[64] D. Irimia, D. Dobrikov, R. Kortekaas, H. Voet, D. A. van den Ende, W. A. Groen, and M. H. M. Janssen, Rev. Sci. Instrum. **80**, 113303 (2009).

[65] U. Even, J. Jortner, D. Noy, N. Lavie, and N. Cossart-Magos, J. Chem. Phys. **112**, 8068 (2000).

[66] E. R. Abraham and E. A. Cornell, Appl. Opt. **37**, 1762 (1998).

[67] J. S. Kienitz, S. Trippel, T. Mullins, K. Długołęcki, R. González-Férez, and J. Küpper, Chem. Phys. Chem. **17**, 3740 (2016), arXiv:1607.05615 [physics] .

[68] A. T. J. B. Eppink and D. H. Parker, Rev. Sci. Instrum. **68**, 3477 (1997).

[69] M. R. Ligare, A. M. Rijs, G. Berden, M. Kabeláč, D. Nachtigallova, J. Oomens, and M. S. de Vries, J. Phys. Chem. B **119**, 7894 (2015).

[70] J. Zhang, L. Pei, and W. Kong, J. Chem. Phys. **128**, 104301 (2008).

[71] K. Nass, L. Foucar, T. R. M. Barends, E. Hartmann, S. Botha, R. L. Shoeman, R. B. Doak, R. Alonso-Mori, A. Aquila, S. Bajt, A. Barty, R. Bean, K. R. Beyerlein, M. Bublitz, N. Drachmann, J. Gregersen, H. O. Jönsson, W. Kabsch, S. Kassemeyer, J. E. Koglin, M. Krumrey, D. Mattle, M. Messerschmidt, P. Nissen, L. Reinhard, O. Sitsel, D. Sokaras, G. J. Williams, S. Hau-Riege, N. Timneanu, C. Caleman, H. N. Chapman, S. Boutet, and I. Schlichting, J. Synchrotron Rad. **22**, 225 (2015).

[72] J. M. Glownia, A. Natan, J. P. Cryan, R. Hartsock, M. Kozina, M. P. Minitti, S. Nelson, J. Robinson, T. Sato, T. van Driel, G. Welch, C. Weninger, D. Zhi, and P. H. Bucksbaum, Phys. Rev. Lett. **117**, 153003 (2016), arXiv:1608.03039 [physics] .

[73] F. Calegari, D. Ayuso, A. Trabattoni, L. Belshaw, S. De Camillis, S. Anumula, F. Frassetto, L. Poletto, A. Palacios, P. Decleva, J. B. Greenwood, F. Martín, and M. Nisoli, Science **346**, 336 (2014).

[74] M. Alauddin, H. S. Biswal, E. Gloaguen, and M. Mons, Phys. Chem. Chem. Phys. **17**, 2169 (2015).

[75] H. L. Bethlem, M. R. Tarbutt, J. Küpper, D. Carty, K. Wohlfart, E. A. Hinds, and G. Meijer, J. Phys. B **39**, R263 (2006), arXiv:0604020 [physics] .

[76] E. A. Rohlfing, D. M. Cox, and A. Kaldor, J. Chem. Phys. **81**, 3322 (1984).

[77] C. R. Calvert, L. Belshaw, M. J. Duffy, O. Kelly, R. B. King, A. G. Smyth, T. J. Kelly, J. T. Costello, D. J. Timson, W. A. Bryan, T. Kierspel, P. Rice, I. C. E. Turcu, C. M. Cacho, E. Springate, I. D. Williams, and J. B. Greenwood, Phys. Chem. Chem. Phys. **14**, 6289 (2012).

[78] P. Arrowsmith, M. S. de Vries, H. E. Hunziker, and H. R. Wendt, Appl. Phys. B **46**, 165

(1988).

[79] D. A. Horke, N. Roth, L. Worbs, and J. Küpper, J. Appl. Phys. **121**, 123106 (2017), arXiv:1609.09020 [physics] .

[80] F. Piuzzi, I. Dimicoli, M. Mons, B. Tardivel, and Q. C. Zhao, Chem. Phys. Lett. **320**, 282 (2000).

[81] C. Soto, Nat. Rev. Neurosci. **4**, 49 (2003).

[82] K. Hsiao, H. F. Baker, T. J. Crow, M. Poulter, F. Owen, J. D. Terwilliger, D. Westaway, J. Ott, and S. B. Prusiner, Nature **338**, 342 (1989).

[83] M. Bucciantini, E. Giannoni, F. Chiti, F. Baroni, L. Formigli, J. Zurdo, N. Taddei, G. Ramponi, C. M. Dobson, and M. Stefani, Nature **416**, 507 (2002).

[84] A. R. Fersht, J.-P. Shi, J. Knill-Jones, D. M. Lowe, A. J. Wilkinson, D. M. Blow, P. Brick, P. Carter, M. M. Y. Waye, and G. Winter, Nature **314**, 235 (1985).

[85] E. S. Feldblum and I. T. Arkin, PNAS **111**, 4085 (2014).

[86] N. S. Nagornova, T. R. Rizzo, and O. V. Boyarkin, Science **336**, 320 (2012).

[87] B. C. Dian, A. Longarte, and T. S. Zwier, Science **296**, 2369 (2002).

[88] E. G. Robertson and J. P. Simons, Phys. Chem. Chem. Phys. **3**, 1 (2001).

[89] A. M. Rijs, G. Ohanessian, J. Oomens, G. Meijer, G. von Helden, and I. Compagnon, Angew. Chem. Int. Ed. **49**, 2332 (2010).

[90] R. Weinkauf, J. Schermann, M. S. de Vries, and K. Kleinermanns, Eur. Phys. J. D **20**, 309 (2002).

[91] K. Schwing and M. Gerhards, Int. Rev. Phys. Chem. **35**, 569 (2016).

[92] R. D. Suenram and F. J. Lovas, J. Am. Chem. Soc. **102**, 7180 (1980).

[93] M. Y. Choi and R. E. Miller, J. Am. Chem. Soc. **128**, 7320 (2006).

[94] S. Blanco, M. E. Sanz, J. C. Lopez, and J. L. Alonso, PNAS **104**, 20183 (2007).

[95] C. A. Taatjes, O. Welz, A. J. Eskola, J. D. Savee, A. M. Scheer, D. E. Shallcross, B. Rotavera, E. P. F. Lee, J. M. Dyke, D. K. W. Mok, D. L. Osborn, and C. J. Percival, Science **340**, 177 (2013).

[96] Y.-P. Chang, K. Długołęcki, J. Küpper, D. Rösch, D. Wild, and S. Willitsch, Science **342**, 98 (2013), arXiv:1308.6538 [physics] .

[97] L. Khriachtchev, A. Domanskaya, K. Marushkevich, M. Räsänen, B. Grigorenko, A. Ermilov, N. Andrijchenko, and A. Nemukhin, J. Phys. Chem. A **113**, 8143 (2009).

[98] H.-Y. Lin, Y.-H. Huang, X. Wang, J. M. Bowman, Y. Nishimura, H. A. Witek, and Y.-P. Lee, Nat. Commun. **6**, 7012 (2015).

[99] M. M. Seibert, T. Ekeberg, F. R. N. C. Maia, M. Svenda, J. Andreasson, O. Jönsson, D. Odić, B. Iwan, A. Rocker, D. Westphal, M. Hantke, D. P. Deponte, A. Barty, J. Schulz, L. Gumprecht, N. Coppola, A. Aquila, M. Liang, T. A. White, A. Martin, C. Caleman, S. Stern, C. Abergel, V. Seltzer, J.-M. Claverie, C. Bostedt, J. D. Bozek, S. Boutet, A. A. Miahnahri, M. Messerschmidt, J. Krzywinski, G. Williams, K. O. Hodgson, M. J. Bogan, C. Y. Hampton, R. G. Sierra, D. Starodub, I. Andersson, S. Bajt, M. Barthelmess, J. C. H. Spence, P. Fromme, U. Weierstall, R. Kirian, M. Hunter, R. B. Doak, S. Marchesini, S. P. Hau-Riege, M. Frank, R. L. Shoeman, L. Lomb, S. W. Epp, R. Hartmann, D. Rolles, A. Rudenko, C. Schmidt, L. Foucar, N. Kimmel, P. Holl, B. Rudek, B. Erk, A. Hömke, C. Reich, D. Pietschner, G. Weidenspointner, L. Strüder, G. Hauser, H. Gorke, J. Ullrich, I. Schlichting, S. Herrmann, G. Schaller, F. Schopper, H. Soltau, K.-U. Kühnel, R. Andritschke, C.-D. Schröter, F. Krasniqi, M. Bott, S. Schorb, D. Rupp, M. Adolph, T. Gorkhover, H. Hirsemann, G. Potdevin, H. Graafsma, B. Nilsson, H. N. Chapman, and J. Hajdu, Nature **470**, 78 (2011).

[100] J. Yang, M. Guehr, X. Shen, R. Li, T. Vecchione, R. Coffee, J. Corbett, A. Fry, N. Hartmann, C. Hast, K. Hegazy, K. Jobe, I. Makasyuk, J. Robinson, M. S. Robinson, S. Vetter, S. Weathersby, C. Yoneda, X. Wang, and M. Centurion, Phys. Rev. Lett. **117**, 153002 (2016).

[101] N. Teschmit, K. Długołęcki, D. Gusa, I. Rubinsky, D. A. Horke, and J. Küpper, J. Chem. Phys. **147**, 144204 (2017), arXiv:1706.04083 [physics] .

[102] J. H. Nielsen, P. Simesen, C. Z. Bisgaard, H. Stapelfeldt, F. Filsinger, B. Friedrich, G. Meijer, and J. Küpper, Phys. Chem. Chem. Phys. **13**, 18971 (2011), arXiv:1105.2413 [physics] .

[103] D. A. Horke, Y.-P. Chang, K. Długołęcki, and J. Küpper, Angew. Chem. Int. Ed. **53**, 11965 (2014), arXiv:1407.2056 [physics] .

[104] S. Trippel, T. Mullins, N. L. M. Müller, J. S. Kienitz, R. González-Férez, and J. Küpper, Phys. Rev. Lett. **114**, 103003 (2015), arXiv:1409.2836 [physics] .

[105] F. Filsinger, J. Küpper, G. Meijer, L. Holmegaard, J. H. Nielsen, I. Nevo, J. L. Hansen, and H. Stapelfeldt, J. Chem. Phys. **131**, 064309 (2009), arXiv:0903.5413 [physics] .

[106] M. Francl, Nat Chem **4**, 142 (2012).

[107] G. von Helden, T. Wyttenbach, and M. T. Bowers, Science **267**, 1483 (1995).

[108] F. Lanucara, S. W. Holman, C. J. Gray, and C. E. Eyers, Nat. Chem. **6**, 281 (2014).

[109] F. Filsinger, S. Putzke, H. Haak, G. Meijer, and J. Küpper, Phys. Rev. A **82**, 052513 (2010).

[110] J. S. Kienitz, K. Długołęcki, S. Trippel, and J. Küpper, J. Chem. Phys. **147**, 024304 (2017), https://doi.org/10.1063/1.4991479 .

[111] S. Trippel, M. Johny, T. Kierspel, J. Onvlee, H. Bieker, H. Ye, T. Mullins, L. Gumprecht, K. Długołęcki, and J. Küpper, (2018), submitted, arXiv:1802.04053 [physics] .

[112] S. Trippel, Y.-P. Chang, S. Stern, T. Mullins, L. Holmegaard, and J. Küpper, Phys. Rev. A **86**, 033202 (2012), arXiv:1208.4935 [physics] .

[113] W. Ackermann, G. Asova, V. Ayvazyan, A. Azima, N. Baboi, J. Bähr, V. Balandin, B. Beutner, A. Brandt, A. Bolzmann, R. Brinkmann, O. I. Brovko, M. Castellano, P. Castro, L. Catani, E. Chiadroni, S. Choroba, A. Cianchi, J. T. Costello, D. Cubaynes, J. Dardis, W. Decking, H. Delsim-Hashemi, A. Delserieys, G. Di Pirro, M. Dohlus, S. Düsterer, A. Eckhardt, H. T. Edwards, B. Faatz, J. Feldhaus, K. Flöttmann, J. Frisch, L. Fröhlich, T. Garvey, U. Gensch, C. Gerth, M. Görler, N. Golubeva, H. J. Grabosch, M. Grecki, O. Grimm, K. Hacker, U. Hahn, J. H. Han, K. Honkavaara, T. Hott, M. Hüning, Y. Ivanisenko, E. Jaeschke, W. Jalmuzna, T. Jezynski, R. Kammering, V. Katalev, K. Kavanagh, E. T. Kennedy, S. Khodyachykh, K. Klose, V. Kocharyan, M. Körfer, M. Kollewe, W. Koprek, S. Korepanov, D. Kostin, M. Krassilnikov, G. Kube, M. Kuhlmann, C. L. S. Lewis, L. Lilje, T. Limberg, D. Lipka, F. Löhl, H. Luna, M. Luong, M. Martins, M. Meyer, P. Michelato, V. Miltchev, W. D. Möller, L. Monaco, W. F. O. Müller, O. Napieralski, O. Napoly, P. Nicolosi, D. Nölle, T. Nuñez, A. Oppelt, C. Pagani, R. Paparella, N. Pchalek, J. Pedregosa-Gutierrez, B. Petersen, B. Petrosyan, G. Petrosyan, L. Petrosyan, J. Pflüger, E. Plönjes, L. Poletto, K. Pozniak, E. Prat, D. Proch, P. Pucyk, P. Radcliffe, H. Redlin, K. Rehlich, M. Richter, M. Roehrs, J. Roensch, R. Romaniuk, M. Ross, J. Rossbach, V. Rybnikov, M. Sachwitz, E. L. Saldin, W. Sandner, H. Schlarb, B. Schmidt, M. Schmitz, P. Schmüser, J. R. Schneider, E. A. Schneidmiller, S. Schnepp, S. Schreiber, M. Seidel, D. Sertore, A. V. Shabunov, C. Simon, S. Simrock, E. Sombrowski, A. A. Sorokin, P. Spanknebel, R. Spesyvtsev, L. Staykov, B. Steffen, F. Stephan, F. Stulle, H. Thom, K. Tiedtke, M. Tischer, S. Toleikis, R. Treusch, D. Trines, I. Tsakov, E. Vogel, T. Weiland,

H. Weise, M. Wellhöfer, M. Wendt, I. Will, A. Winter, K. Wittenburg, W. Wurth, P. Yeates, M. V. Yurkov, I. Zagorodnov, and K. Zapfe, Nat. Photon. **1**, 336 (2007).

[114] T. Kierspel, J. Wiese, T. Mullins, J. Robinson, A. Aquila, A. Barty, R. Bean, R. Boll, S. Boutet, P. Bucksbaum, H. N. Chapman, L. Christensen, A. Fry, M. Hunter, J. E. Koglin, M. Liang, V. Mariani, A. Morgan, A. Natan, V. Petrovic, D. Rolles, A. Rudenko, K. Schnorr, H. Stapelfeldt, S. Stern, J. Thøgersen, C. H. Yoon, F. Wang, S. Trippel, and J. Küpper, J. Phys. B **48**, 204002 (2015), arXiv:1506.03650 [physics] .

[115] M. S. Gordon and M. W. Schmidt, in *Theory and Applications of Computational Chemistry: the first forty years*, edited by C. E. Dykstra, G. Frenking, K. S. Kim, and G. E. Scuseria (Elsevier, Amsterdam, 2005).

[116] K. Iijima, K. Tanaka, and S. Onuma, J. Mol. Struct. **246**, 257 (1991).

[117] A. Y. Ivanov, G. Sheina, and Y. P. Blagoi, Spectrochim. Acta A **55**, 219 (1998).

[118] T. F. Miller and D. C. Clary, Phys. Chem. Chem. Phys. **6**, 2563 (2004).

[119] T. F. Miller III, D. C. Clary, and A. J. H. M. Meijer, J. Chem. Phys. **122**, 244323 (2005).

[120] A. I. Kuleff and L. S. Cederbaum, Chem. Phys. **338**, 320 (2007).

[121] J. P. Marangos, J. Phys. B **49**, 132001 (2016).

[122] T. Kierspel, *Imaging structure and dynamics using controlled molecules*, Dissertation, Universität Hamburg, Hamburg, Germany (2016).

[123] A. J. H. M. Meijer, "*private communication*," (2013).

[124] M. J. Duffy, O. Kelly, C. R. Calvert, R. B. King, L. Belshaw, T. J. Kelly, J. T. Costello, D. J. Timson, W. A. Bryan, T. Kierspel, I. C. E. Turcu, C. M. Cacho, E. Springate, I. D. Williams, and J. B. Greenwood, J. Am. Soc. Mass. Spectrom. **24**, 1366 (2013).

[125] A. Kilaj, H. Gao, D. Rösch, U. Rivero, J. Küpper, and S. Willitsch, Nat. Commun. (2018), in print.

[126] R. Liu, Q. Li, and L. M. Smith, J. Am. Soc. Mass. Spectrom. **25**, 1374 (2014).

[127] G. C. Hilton, J. M. Martinis, D. A. Wollman, K. D. Irwin, L. L. Dulcie, D. Gerber, G. P. M., and T. D., Nature **391**, 672 (1998).

[128] K. L. Ekinci, X. M. H. Huang, and M. L. Roukes, Appl. Phys. Lett. **84**, 4469 (2004).

[129] H. Kim, J. Park, Z. Aksamija, M. Arbulu, and R. Blick, Phys. Rev. Appl. **6**, 064031 (2016).

[130] R. E. Russo, X. Mao, H. Liu, J. Gonzalez, and S. S. Mao, Talanta **57**, 425 (2002).

[131] U. Even, Adv. Chem. **2014**, 636042 (2014).

[132] M. Smits, C. A. de Lange, S. Ullrich, T. Schultz, M. Schmitt, J. G. Underwood, J. P. Shaffer, D. M. Rayner, and A. Stolow, Rev. Sci. Instrum. **74**, 4812 (2003).

[133] B. S. Zhao, M. Castillejo, D. S. Chung, B. Friedrich, and D. Herschbach, Rev. Sci. Instrum. **75**, 146 (2004).

[134] T. Schlathölter, G. Reitsma, D. Egorov, O. Gonzalez-Magaña, S. Bari, L. Boschman, E. Bodewits, K. Schnorr, G. Schmid, C. D. Schröter, R. Moshammer, and R. Hoekstra, Angew. Chem. Int. Ed. **55**, 10741 (2016).

[135] T. Kierspel, C. Bomme, M. Di Fraia, J. Wiese, D. Anielski, S. Bari, R. Boll, B. Erk, J. S. Kienitz, N. L. M. Müller, D. Rolles, J. Viefhaus, S. Trippel, and J. Küpper, (2018), arXiv:1802.02964 [physics.atm-clus] .

[136] D. Polli, P. Altoè, O. Weingart, K. M. Spillane, C. Manzoni, D. Brida, G. Tomasello, Gaia andOrlandi, P. Kukura, R. A. Mathies, M. Garavelli, and G. Cerullo, Nature **467**, 440 (2010).

[137] B. C. Dian, G. M. Florio, J. R. Clarkson, A. Longarte, and T. S. Zwier, J. Chem. Phys. **120**, 9033 (2004).

[138] T. Kierspel, S. Trippel, J. Küpper, *et al.*, In preparation (2017).

Curriculum Vitae – Nicole Teschmit

Education

01.2014 - today	Dissertation (Dr. rer. nat.) *Universität Hamburg* Thesis title: Cold beams of Large Molecules for Structural Dynamics Studies
05.2012 - 10.2013	Master in Chemistry *Technische Universität Braunschweig* Thesis title: Optically and collisionally induced electric transitions in iodine molecules in excited states
10.2009 - 05.2012	Bachelor in Chemistry *Technische Universität Braunschweig* Thesis title: Strukturuntersuchungen an Thioharnstoffderivaten

Fellowships

11.2014 - 07.2016	Kekulé-Fellowship *Fonds der chemischen Industrie (FCI)*
04.2013	Fellowship of the German-Russian Interdisciplinary Science Center *Deutscher Akademischer Austauschdienst (DAAD)*

Time Abroad

04.2013 - 08.2013	The experiments for the master thesis were conducted in Saint Petersburg in cooperation with the *Saint Petersburg State University*

Publications

1. N. Teschmit, T. Kierspel, L. He, D. A. Horke, S. Trippel, J. Küpper, A conformer-pure beam of glycine, in preparation (2018)
2. N. Teschmit, D. A. Horke, J. Küpper, Spatially separating the conformers of a dipeptide, *Angew. Chem. Int. Ed.*, submitted (2018)
3. N. Teschmit, K. Długołęcki, D. Gusa, I. Rubinsky, D. A. Horke, J. Küpper, *J. Chem. Phys.* **147**, 144204 (2017)
4. M. E. Akopyan, V. V. Baturo, S. S. Lukashov, S. A. Poretsky, A. M. Pravilov, N. Teschmit, *J. Phys. B: At. Mol. Opt. Phys.* **47**, 055101 (2014)
5. P. J. Jones, C. Taouss, N. Teschmit, L. Thomas, *Acta Cryst. B* **69**, 405 (2013)
6. C. Näther, I. Jess, P. G. Jones, C. Taouss, N. Teschmit, *Cryst. Growth Des.* **13**, 1676 (2013)

H- und P-Sätze

Substanz	Symbol	H-Sätze	P-Sätze
Aceton	🔥 ❗ Gefahr	H225, H319, H336	P210, P280, P304+P340+P312, P305+P351+P338, P337+P313, P403+P235
Ac-Phe-Cys-NH_2	unbekannt	unbekannt	unbekannt
Coumarin 153	kein Gefahrstoff	—	—
Ethanol	🔥 ❗ Gefahr	H225, H319	P210, P280, P305+P351+P338, P337+P313, P403+P235
Fluorescein	☠ Achtung	H319	P305+P351+P338
Glycin	kein Gefahrstoff	—	—
Graphit	kein Gefahrstoff	—	—
Insulin (vom Rind)	kein Gefahrstoff	—	—

Isopropanol	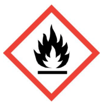 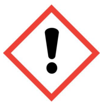 Gefahr	H225, H319, H336	P210, P305+P351+P338, P370+P378, P403+P235
Methanol	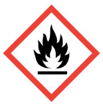 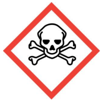 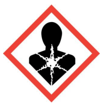 Gefahr	H225, H301+H311+H331, H370	P210, P280, P302+P352+P312, P304+P340+P311, P370+P378, P403+P235
Phenylalanin	kein Gefahrstoff	—	—
Rhodamin 6G	kein Gefahrstoff	—	—
Rhodamin B	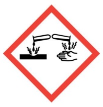 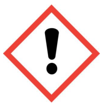 Gefahr	H302, H318, H412	P273, P280, P305+P351+P338

übernommen aus den Sicherheitsdatenblättern auf SigmaAldrich.com

Acknowledgment

At first I would like to thank my parents, grandparents and my brother. You took such good care of me for now nearly thirty years. Thank you that you encouraged and believed in me. I love you very much. Thank you, Daniel Horke, for all your patient explanations, for the long times you spend with me in the lab, for listening and helping when I was stressed, for making me laugh, for pizza and many many coffees.

I would like to thank my supervisor Jochen Küpper for the help, discussions, and financial support. Nele Müller thank you for all your advise, scientifically and private. It has been of great help for me and you turned out to be a friend I do not want to miss. I would like to thank Thomas Kierspel. It was really helpful and nice to work my first year or two next to you in the lab. You gave me much useful advise and encouraged me so much to represent my own opinions. Thanks for beeing such a happy person from Cologne. Thanks also to Jens Kienitz, for your sprints to the lab when LabView was broken and for the much advise you gave me regarding electronics and things to do. Thank you Karol for designing the machine. The assembling of it together with you was great fun. I would also like to thank you for your fast help when something was broken and your kindness. Here I also would like to thank Tim Ossenbrüggen for your help fixing the always leaking SwageLock connection, it was driving me nuts. Daniel Gusa thank you for the help with the fibre collimation and the advice regarding the polishing.

Amit Samanta, thanks for your help in the lab and for always beeing so happy and making fun. Melby Johny thank you for beeing my chat and chai partner always and for your introduction in indian cooking. I thank also Lanhai He for taking good care of the laser desorption machine now. Thank you Markus Metz, Sophie Walter, Cedric Bomme, Andrea Trabattoni and Daniel Horke for going bouldering and spending time with me, I really enjoyed it. Thanks also to Melanie Borchmann for the many evenings you spend with me listening interested to all the scientific stuff I was talking and sometimes complaining about. Last but not least I thank the whole CMI-group and the previous members I met. You all helped me in some way and made this thesis possible.

Thank you!